POLITECNICO DI MILANO

Scuola di Ingegneria dei Sistemi

Corso di Laurea Magistrale in Ingegneria Matematica

Hierarchical Multiscale Modeling and Simulation of Bio-Electronic Interfaces

Relatore:
Prof. Riccardo Sacco
Correlatore:
Dott. Matteo Porro

Tesi di laurea di:
Emanuela Abbate
Matr. 770560

Anno Accademico 2012/13

Abstract

Bio-electronic interfaces are a fundamental subject in the wider areas of electrochemistry and neuroscience. The aim of this Master Thesis is to derive and numerically solve a hierarchy of novel mathematical models, which can serve as a supporting tool for design and investigation of innovative bio-hybrid structures.

The basis of the present work is a three dimensional model describing the ionic concentration dynamics and the electrical displacement in the extracellular fluid as the result of an external stimulation of the cell. The focus is on the thin sheet of electrolyte bath between the cell and the electronic device, where most of the physical phenomena occur. Ion channels and capacitive couplings at the cellular membrane and at the oxide layer covering the device are modeled through specific transmission conditions. Numerical computations are performed in axisymmetric configurations, introducing a suitable exponentially fitted finite element discretization for these particular geometries. Simulations are able to characterize not only the behavior of a single cell on a single electrode, but also the mutual interactions between multiple cells and multiple devices, providing results that are in good agreement with physical expectation and experiments.

A detailed derivation of geometrically reduced models is also presented and validated on numerical simulations of biological relevance, conducted in the middle plane of the considered electrolyte cleft.

Abstract

L'accoppiamento di dispositivi elettronici con materiali bologici è un aspetto fondamentale nel campo delle neuroscienze e dell'elettrochimica. L'obiettivo di questa Tesi è la derivazione e la risoluzione numerica di una gerarchia di nuovi modelli matematici che possano essere uno strumento utile nell'ambito di queste discipline.

Il punto di partenza del lavoro è un modello tridimensionale per descrivere il flusso di ioni e il campo elettrico che si creano nel fluido extracellulare quando una cellula viene stimolata dall'esterno. L'attenzione viene posta sul sottile strato di elettrolita tra la cellula e il dispositivo elettronico, dove avvengono i fenomeni fisici di maggior interesse. La descrizione dei canali ionici e degli accoppiamenti capacitivi con la membrana cellulare e con l'ossido che ricopre il substrato è affidata a specifiche condizioni di trasmissione. Per quanto riguarda il trattamento numerico del modello, è stata introdotta una discretizzazione ad elementi finiti di tipo "exponential fitting" adattata a trattare le particolari configurazioni assialsimmetriche studiate. Le simulazioni condotte riproducono non soltanto il comportamento di una singola cellula su un singolo elettrodo, ma anche le interazioni tra più cellule e più dispositivi, con risultati in buon accordo con le aspettative fisiche e i dati sperimentali.

Viene infine presentata la derivazione matematica di una riduzione geometrica del modello di partenza nel piano medio del dominio tridimensionale. I modelli ridotti proposti sono validati su numerose simulazioni numeriche relative a casi test di interesse biologico.

Contents

List of Figures

Symbols and notation

Notation	Definition
∇	Gradient operator
∇_{xy}	Gradient operator in two spatial dimensions
div	Divergence operator
div_{xy}	Divergence operator in two spatial dimensions
$\triangle$	Laplacian
$\mathbf{E}$	Electric field ($\text{V}\,\text{m}^{-1}$)
$\mathbf{D}$	Electric displacement ($\text{C}\,\text{m}^{-2}$)
$\mathbf{j}$	Current density ($\text{A}\,\text{m}^{-2}$)
$\mathbf{f}$	Particle flux ($\text{m}^{-2}\,\text{s}^{-1}$)
ρ	Charge density ($\text{C}\,\text{m}^{-3}$)
c_i	Concentration of the i-th ion (m^{-3})
z_i	Valence of the i-th ion
D_i	Diffusion coefficient of the i-th ion ($\text{m}^2\,\text{s}^{-1}$)
μ_i	Electrical mobility of the i-th ion ($\text{m}^2\,\text{V}^{-1}\,\text{s}^{-1}$)
q	Elementary charge ($1.6022 \times 10^{-19}\,\text{C}$)
ϵ_0	Electric permittivity in free space ($8.8542 \times 10^{-12}\,\text{F}\,\text{m}^{-1}$)
N_A	Avogadro constant ($6.0221 \times 10^{23}\,\text{mol}^{-1}$)
k_B	Boltzmann constant ($1.3806 \times 10^{-23}\,\text{J}\,\text{K}^{-1}$)

Introduction

The research activity of the present Master Thesis can be cast within the context of Bio-Electronics, which is a discipline belonging to the wider areas of Nanotechnologies and Neurosciences. The focus is on the coupling between biological matter and solid state devices: an example of a simple structure can consist of a living cell attached to an electronic substrate and surrounded by an electrolyte bath. This interfacing gives rise to the study of different types of signal trasmissions. One of the main ways of operation consists in the actual stimulation of the cell, with a depolarizing pulse or other specific techniques, transducing the chemical signals produced by the biological component into electronic signals measured by the device. Another way of operation, on the contrary, is the activation of the biomaterials from the electronic component.

The interface contact is realized by a thin conductive electrolyte cleft between the cell and the substrate, whose amplitude is smaller than the cell radius of about three orders of magnitude. Therefore, the cell-chip junction forms a planar electrical core-coat conductor and the main physical phenomena take place in this thin region.

In this work a novel contribution in the area of modeling and simulation of the bio-electronic interfaces is given by introducing a hierarchy of mathematical models able to describe the ion flow and the electric potential variation in the extracellular fluid. The attention is on the layer of extracellular fluid in the cleft, which represents the computational domain chosen to perform the analysis and the simulations. Special interest is devoted to the modeling of the transmembrane currents and of the strong coupling mechanisms with both cell and device, dealt through specific boundary and interface conditions on the considered three dimensional domain. Several modeling hypotheses are also introduced and discussed to mathematically derive different reduced models in the middle horizontal plane of the cleft, whose aim is to reduce the number of the degrees of freedom in the numerical computations.

Extensively conducted simulations reveal that the ion flow and the electric dis-

placement variation mainly occur in the considered cleft. The three dimensional model is solved in axisymmetric configurations and produces sensible results also when considering the mutual interactions among more than only one cell on an electronic substrate. The stimulation of one cell results in turn in a stimulation of the electrodes and of the other cells collocated in the neighbourhood around and this physical behaviour is investigated and effectively reproduced. Finally, computational experiments demonstrate that the proposed model reduction is valid in terms of physical accuracy and useful in terms of decrease of the computational effort.

The thesis structure consists in a first chapter where we present an overview of the main components and features of bio-electronic interfaces. Great importance is given to the cell membrane, which is actually the major leader in the considered phenomena, to the stimulation techniques and to the coupling between the biological and the electronic environments.

The hierarchical mathematical modeling is discussed in Chapter 2, using the Poisson Nernst Planck system as a basis and starting point in the description of the motion of the charged particles in the electrolyte. The adopted approach consists in solving the equations in the cleft junction, accounting for the cell and for the device with appropriately chosen coupling conditions based on several symplifying modeling assumptions. With an averaging procedure and proper hypotheses on the distributions of the potential and of the concentrations, based on the physical nature of the problem, a geometrical reduction is then performed from a three dimensional picture leading to a suitable two dimensional formulation in the middle section of the electrolyte cleft.

In Chapter 3 we illustrate the general scheme used to numerically solve the mathematical models. Time dependence is dealt with a Backward Euler scheme and at each time level the resulting nonlinear system is solved with a staggered algorithm, namely the Gummel Map iterative procedure. After the application of this solution map, the equations are decoupled and at each iteration one needs to solve a diffusion advection reaction problem with strongly advection dominating terms. A spatial discretization with an exponentially fitted finite element method is introduced and described for the particular case of axisymmetric geometries.

In Chapter 4 an extensive validation of all the mathematical models of the present work is performed. We study and analyze in detail some test cases for the discretization in axial symmetry and then we apply this numerical procedure to solve many

different biological cases. Not only a simple cell-chip junction is considered, but the analysis focuses also on the simulation of the interaction between multiple cells and multiple devices, obtaining physically sound behaviors and results. Then we also reproduce the same results with the models of reduced order, to validate the mathematical procedure and the assumptions introduced in Chapter 2.

Finally, in Chapter 5 we present a summary of the main mathematical and computational aspects investigated in this thesis and we indicate several possible future research developements in the area of modeling and simulation of bio-electronic interfaces.

Chapter 1

Introduction to Bio-Hybrid Devices

In this chapter we give a short introduction to the subject of bio-electronics, a scientific discipline whose principal aim is to couple a biological component (a cell or a system of cells) and a solid-state device (a silicon transistor or an array of transistors).

1.1 Basic principles of bio-electronics

Bio-Electronics is a scientific and technological discipline that deals with the study of the coupling of biomolecules with electronic devices. The interfacing of biomaterials and electronic devices can be used to transduce chemical signals generated by biological components into electronically readable signals or, conversely, to activate the biomaterials by applying electronic signals, thus resulting in a switchable performance of the biological components. The scientific and practical importance of bio-electronics reflects in a variety of different fields, as basic science, practical use in medicine, high-tech industry and many other applications [54]. Miniaturization is a requisite for future implantable bio-electronic devices, and these types of applications will certainly introduce the need for biocompatibility of the systems. Miniaturization will also require the patterned, dense organization of biomolecules on electronic supports.

As explained in [53], cell-silicon junctions are the basis for an integration of neuronal dynamics and digital electronics. One way of operation is the so called “cell to chip” mode: an input biological signal is transduced into an electrical signal, which can be measured at the output terminals of the electronic substrate (as in non- invasive techniques to record cellular response to drugs and/or toxins [23]). The second way is called “chip to cell” mode: an electrical signal applied to the chip can induce

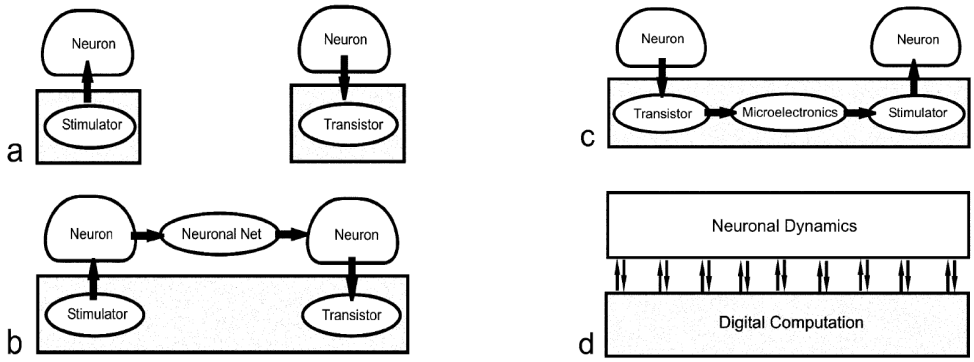

Figure 1.1.1 – Neuroelectronic hybrids and cell transistor schemes (from [53]).

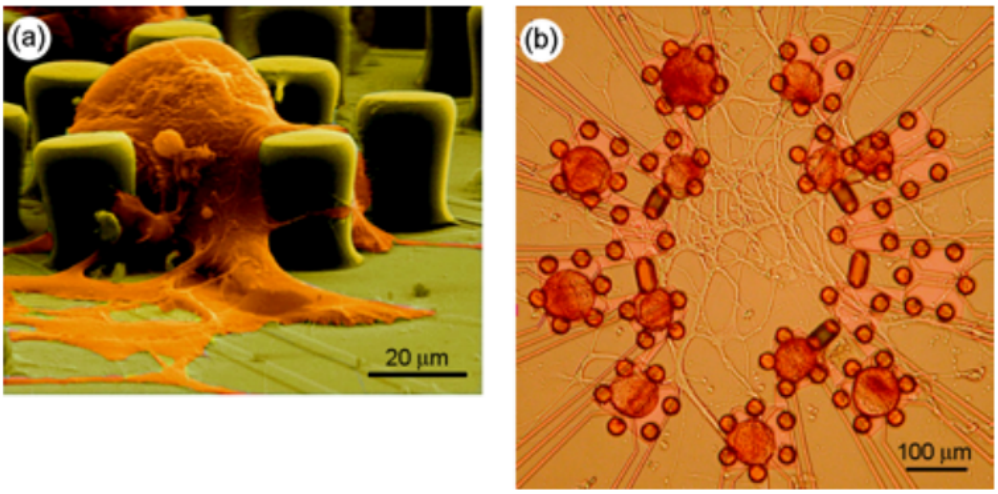

Figure 1.1.2 – Network of neurons on a silicon chip (from [53]).

a stimulation of the cell.

To illustrate some basic ideas we now describe the structure of a communication system between cells and chips. The simplest configuration is the interface of individual nerve cells and silicon microstructures and is shown in Fig. 1.1.1-(a). Neuronal activity is elicited by capacitive stimulation from the chip and is then recorded by a transistor. On a next level, pairs of nerve cells are coupled to a chip. Fig. 1.1.1-(b) schematically depicts the operation of a neuronal network: the network receives a signal from a stimulator, then it elaborates the signal, and finally transmits the information to an electronic device for further use. In Fig. 1.1.1-(c) the role of the biological and electrical components is reversed compared to Fig. 1.1.1-(b): as a matter of fact, the electronic device elaborates the signal received from the cell, and then the

resulting output signal is used as a driving force for the stimulator towards a second cell. Configurations (b) and (c) are therefore mutually complementary. In a further step, neuronal networks are created on the chip in such a way that an intimate communication of network dynamics and computation is built (Fig. 1.1.1-(d)).

The neuronal network shown in Fig. 1.1.2 conceptually corresponds to the configuration of Fig. 1.1.1-(b) and is grown onto a silicon substrate, where transistors were implemented before the implantation of the cells and neuronal cell bodies are inserted into the cages. In this configuration, neurons are electrically stimulated and the electric signal propagates to the end point of the network, where it is transferred, for further elaboration, to a transistor located underneath.

Before going further in analyzing bio-electronic interfaces we need to take a closer look at the cell structure, which is the main biological component of the system and at the techniques used to stimulate it. This is mandatory for the study we want to conduct.

1.2 The cell and the cell membrane

In the present work, the mathematical modeling of the cell and of its membrane is a major object, therefore we take a look at the entire structure of a cell to make sure that the proposed mathematical models account for the main phenomena.

The cell is the basic living unit of the human body. Each type of cell is adapted to perform one or a few specific functions, and identifying and characterizing cells is a big task which pertains the field of medical physiology [18]. Although cells often differ considerably from one another, all of them have certain basic characteristics that are alike. For instance, every different kind of cell uses the same reaction of oxygen with carbohydrate, fat, or protein to release the energy required for its function. The basic structure of a cell is also shared among each type of cell, and is depicted in Fig. 1.2.1.

Its two major parts are the nucleus and the cytoplasm. The nucleus is separated from the cytoplasm by a nuclear membrane, and the cytoplasm is separated from the surrounding fluid by the cell membrane. The different substances that make up the cell are collectively called protoplasm. Protoplasm is composed mainly of five basic substances: water, electrolytes, proteins, lipids, and carbohydrates. Water is by far the principal fluid medium of the cell in a concentration of 70 to 85 per cent for most cells. Many cellular chemicals are suspended or dissolved in water: ions such as

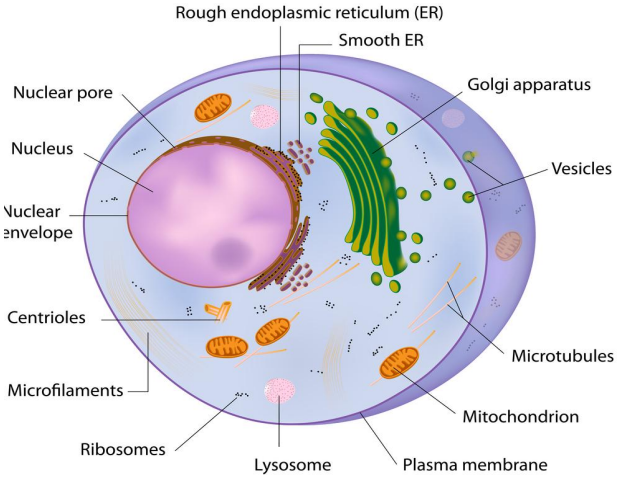

Figure 1.2.1 – Basic structure of a cell.

potassium, magnesium, sodium, chloride, and calcium are present, and play a major role in the electrochemical activity of the cell and in the regulation of the transport of substances across the cell membrane.

The exterior of the cell, or "extracellular fluid", is the medium where cells live, and accounts for almost one third of the body fluids. There are obviously many differences between the quality and quantity of the substances present in the extra- and intracellular fluid: specifically, there is a great difference in the amount of the dissolved ions, a difference due to special transport mechanism occurring at the cell membrane.

Fig. 1.2.2 shows a detail of a two-dimensional cross-section of a cell membrane: it consists almost entirely of a lipid bilayer, with a thickness of the order of 10 nm, but it also contains large numbers of protein molecules in the lipid, many of which penetrate all the way through the membrane. The lipid bilayer is not miscible with water, therefore it constitutes a barrier against the movement of water and water-soluble substances (such as ions) between the extracellular and intracellular compartments. The protein molecules in the membrane have entirely different properties for transporting substances: their molecular structure interrupts the continuity of the lipid bilayer, constituting an alternative pathway through the cell membrane. Most of these penetrating proteins work as transport proteins and are usually highly selective to the types of substances that are allowed to cross the membrane. Protein molecules that permit the flow of ions are called ionic channels [19].

Transport mechanism and selectivity of ionic channels depend on the type of channel that is being considered. Transport can be passive, namely due the simple

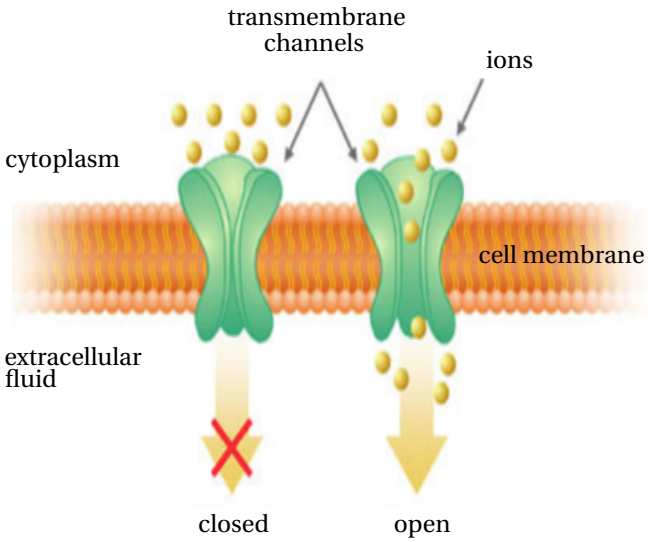

Figure 1.2.2 – Transmembrane channels and ion flow across the membrane.

electrodiffusion of substances, or active, that is the flow of substances is activated with the use of cellular energy (mostly ATP, adenosine triphosphate) in the process. Also, the permeability of the ion channels is often modulated by either the concentration of substances (chemical gating) or the potential difference across the membrane (voltage gating), as is the case for potassium and sodium ion channels. The role of the membrane in the communication between the interior and exterior of the cell is very important, because it supervises the dynamic regulation of the concentration of ionic species dissolved in the cytoplasm. A variation of concentration implies an accumulation or depletion of charged ions, causing in turn a variation of the electric potential V_m across the membrane.

1.3 Cell stimulation: voltage clamp technique

The voltage clamp technique is widely used in electrophysiology to study a single or multiple ion channels in cells and to measure the ion currents through the membrane, while holding the membrane voltage at a prescribed value. It can be applied to a variety of cells, especially to excitable cells such as neurons, cardiomyocytes, muscle fibers and pancreatic cells.

The membranes of excitable cells contain many different kinds of ion channels, some of which are voltage-gated. With the application of the voltage clamp, the membrane voltage V_m can be manipulated independently from the ionic currents, allowing to study the current-voltage relationships of membrane channels. The concept

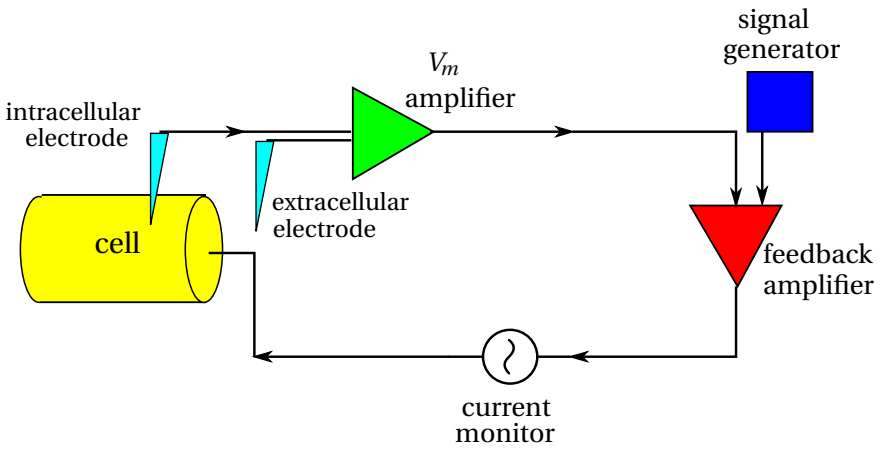

Figure 1.3.1 – Schematics for the voltage-clamp technique.

of the voltage clamp is attributed to Kenneth Cole and George Marmont in the 1940s, then Hodgkin and Huxley discovered in 1952 how ionic currents give rise to the action potential [24].

The voltage clamp consists in a current generator with two electrodes, one inside the cell and the other one in the surrounding bath, as schematically depicted in Fig. 1.3.1. The transmembrane voltage V_m is the difference of potential between the intracellular and the extracellular electrodes. The experimenter sets a "holding voltage", or "command potential" and the voltage clamp maintains the cell at this value. The electrodes are connected to an amplifier, actually measuring and recording membrane potential, and then feeding the signal into a feedback amplifier. Whenever the cell deviates from the holding voltage, this amplifier generates an error signal (the difference between the holding voltage and the actual voltage of the cell). The feedback circuit passes current into the cell to reduce the error signal to zero, therefore the clamp circuit produces a current equal and opposite to the ionic current, giving an accurate reproduction of the currents flowing across the membrane.

In the present work we study and try to reproduce experimental results where voltage clamp and current clamp techniques are applied to stimulate the cells [3, 5, 14, 38, 48, 49]. In most of these experimental setups the configuration consists in one or multiple cells attached on an electronic device (as described in Section 1.4) and the goal is to study the behavior of these cells after an external stimulation, resulting in the opening of the transmembrane channels and in the flow of ions through the surrounding electrolyte. This stimulation is made possible with the use of voltage clamp or patch clamp, which is a refinement of the voltage clamp tecnique developed by Neher and Sakmann in the late 1970s [36].

1.4 Contact between a cell and an electronic device

Great importance has the compatibility of electronics and biological material, because living cell or neurons must be cultured or attached to a substrate that does not threaten their survival. Interfacing biological and electronic systems requires to establish a contact between these two worlds. This contact must be intimate because the distance between cells and electronic devices influences the amount of coupling, as we will see in our numerical simulations.

In order to maintain a spatio-temporal coherence in the measurement and stimulation, the immobilization of biocomponents on the interface is also needed. The methods involved in the culture of neurons on silicon are the basis for the considered application, but we are not describing them in the present work because it would require a huge amount of bio-chemistry (for a detailed explanation see [13]). We can see an example of a simple stucture in Fig. 1.1.2-(a), where the neuron is caged in "micro fences" post-fabricated on the electronic substrate [5, 35].

1.4.1 Ion-electronic interfacing

Fig. 1.4.1 shows an example of what we refer to when describing ion-electronic interfacing. We see the micrograph of a nerve cell from rat brain on a silicon chip, along with source and drains contacts of a linear array of Field Effect Transistors (FET), while the gate contacts are visible as bright squares.

The contact between neurons and substrate is a perfectly polarized electrolyte/oxide electrode without electronic or ionic current. As long as the insulating lipid layer of the membrane is in intimate contact with the substrate insulator, an electrical field across the membrane due to neuronal activity can polarize the silicon dioxide to affect the underlying transistor (cell to chip stimulation). The same effect can also be reversed by applying an electrical field from the substrate in order to polarize the membrane and affect field-sensitive membrane ion channels (chip to cell stimulation).

When a nerve cell grows on a chip, the lipid layer of the cell and the oxide layer of the chip do not form a compact dielectric [13]. Actually, a thin layer of electrolyte is created between cell and substrate, caused by steric repulsion of fibronectin and of proteins in the glycocalix of the cell. The amplitude of the distance between the

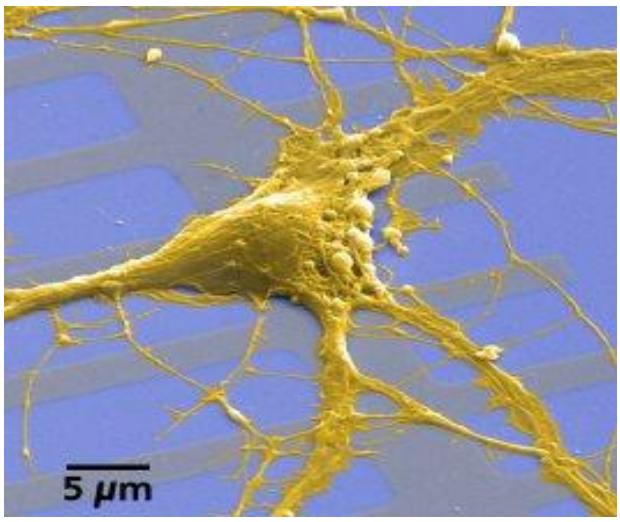

Figure 1.4.1 – Example of ion-electronic interfacing: rat neuron on a linear array of transistors (the ionic current in the cell interacts with the electronic current in the silicon substrate) [57].

cell and the substrate can be measured by fluorescence interference contrast (FLIC) and is usually around 100 nm [5]. This conductive electrolyte cleft shields the electric field, preventing a direct mutual polarization of membrane and dielectric insulator. The cell-silicon junction forms a planar electrical core-coat conductor: the coats of silicon dioxide and membrane insulate the core of the conductive cleft from the conducting environments of silicon and cytoplasm. The neuro-electronic interface is then mediated by the cleft, where the ionic currents from the cell are forced to flow.

Sensing the activity of a neuron can then be divided into two different mechanisms:

- stimulating a neuron leads to electric displacement and ionic currents through the membrane, and a concomitant current along the cleft gives rise to an extracellular potential between cell and chip;
- the potential variation induced by the neuron in the cleft produces an electrical field across the substrate insulator that is then probed by a FET.

1.4.2 An example of bio-hybrid device: the EOSFET

In this section we briefly introduce the simplest example of a bio-chip, namely, the EOSFET (Electrolyte-Oxide Field Effect Transistor). In Fig. 1.4.2 the representation of the working principle of a generic ion-electronic interface is schematically depicted: a neuron surrounded by an electrolyte bath is attached to an electronic device. This

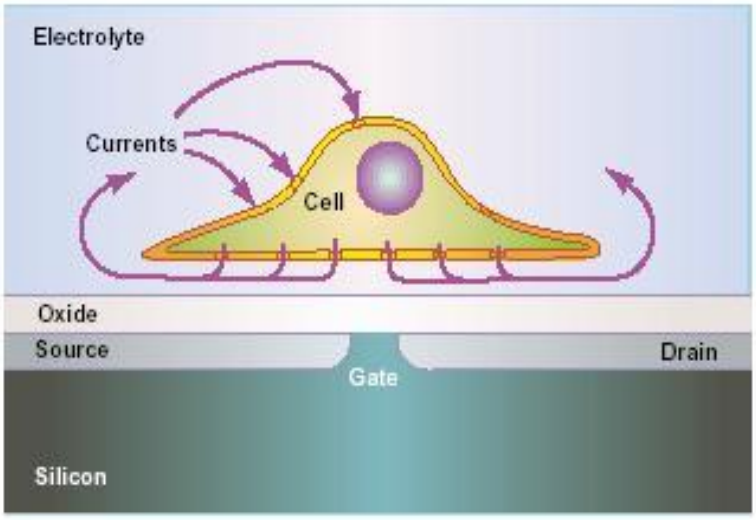

Figure 1.4.2 – Schematics of a neuro-chip [35].

is the so called EOSFET structure, namely a transistor device where the gate contact is made by an electrolyte solution instead of a metal interconnection, as in standard semiconductor technology. The structural difference between the EOSFET and the conventional MOSFET (Metal-Oxide Field Effect Transistor) device implies a radical change in the nature of the charges controlling the transistor. In the case of a MOSFET, the conducting channel is gated by the electric field generated by electrons in the gate contact, while in the case of a EOSFET the gating process is operated by ionic charges coming from the cell towards the semiconductor.

Integration of cell and chip is made possible by proper control of the flow of ionic charges exchanged between the cell and the semiconductor component, in such a way that the hybrid device can work under two different modes of operation. In the first mode, the cell gates the transistor and regulates the electronic current flowing into the transistor conducting channel. In the second mode, which is the reverse case, the cell acts as the receiver of a signal coming from a microelectronical network. The EOSFET also presents a ionic sensitivity due to interactions between its chemically sensitive insulator surface and the ions in the electrolyte solution [52].

Chapter 2

Mathematical Models

In this chapter we extensively illustrate the modeling hypotheses and the mathematical equations used in the present work to describe and to simulate bio-electronic interfaces. The Poisson-Nernst-Planck system is the starting point for the self consistent treatment of ion electrodiffusion and potential variations in the thin layer of electrolyte between the cell and the electronic device.

2.1 Mathematical modeling of bio-electronic interfaces

In order to characterize the bio-electronic interfaces described in Chapter 1, we need to elaborate a suitable physical model, whose aim can be thought either as an opportunity to confirm the understanding and analysis of experimental data or as a tool to be used in the design of actual devices. The present work is not a "real-world" simulation/design tool, but can be considered a first step in the direction of the construction of a mathematical simplified model, which is able to reproduce experimental results and to be applied in complex configurations.

To fully describe bio-electronic interfaces, a broad range of mathematical models should be considered. As a matter of fact, the phenomena involved are of very different nature, since they originate from two separate domains (the biological world and the electronic device) with different physical behaviors and scales, both temporal and spatial.

More in detail, one has to consider three levels of modeling:

- bio-physical models to describe the behavior of the cell. The cell membrane

is crucial for this application, because it controls the ionic flow through the cell. As pointed out in [26, 29], the transfer of substances to and from the cell is strongly affected by pressure, by changing the cell volume and also by varying the distance between the cell and silicon device;

- advection-diffusion models to describe the flow of substances in the intra- and extra-cellular spaces. The transport processes of charged particles are mainly due to diffusion and electric field drift. Fluid-mechanical forces also act on the substances present in the liquid medium, as well as chemical reactions taking place at the silicon-electrolyte interface and in the whole aqueous solution, as pointed out in [5];

- an appropriate drift-diffusion model to represent the electric current flow into the semiconductor device [50, 30] and the interaction of the electric field with the overlying biological domain;

Such a detailed level of description would lead to a multiphysics mathematical model, in a heterogeneous three dimensional representation, through a strongly coupled nonlinear system of partial differential equations. Obviously, this very general approach would require a very large amount of computational burden to be solved and this is the motivation to introduce suitable simplifying approximations.

In the mathematical treatise carried out in this chapter, we reduce the computational domain to a thin layer of electrolyte and then introduce a suitable three dimensional model, in order to study in detail the physical phenomena taking place in the extracellular bath. After that, we discuss a possible model reduction in a two dimensional domain, to decrease the computational complexity. Thanks to an averaging procedure and some physical assumptions on the distributions along the z-direction, we derive different hierarchical models describing the quatities of interest only in a x-y plane.

2.2 Three dimensional model

In this section we derive a three dimensional model of the interface between cell and electronic substrate. The mathematical description should account for variations in time and space of the potential and of the ion species flowing in the bath, keeping in mind that everything is due to the influence of the cell and the substrate, which can be both stimulated and/or controlled from the outside: this eventually results in the

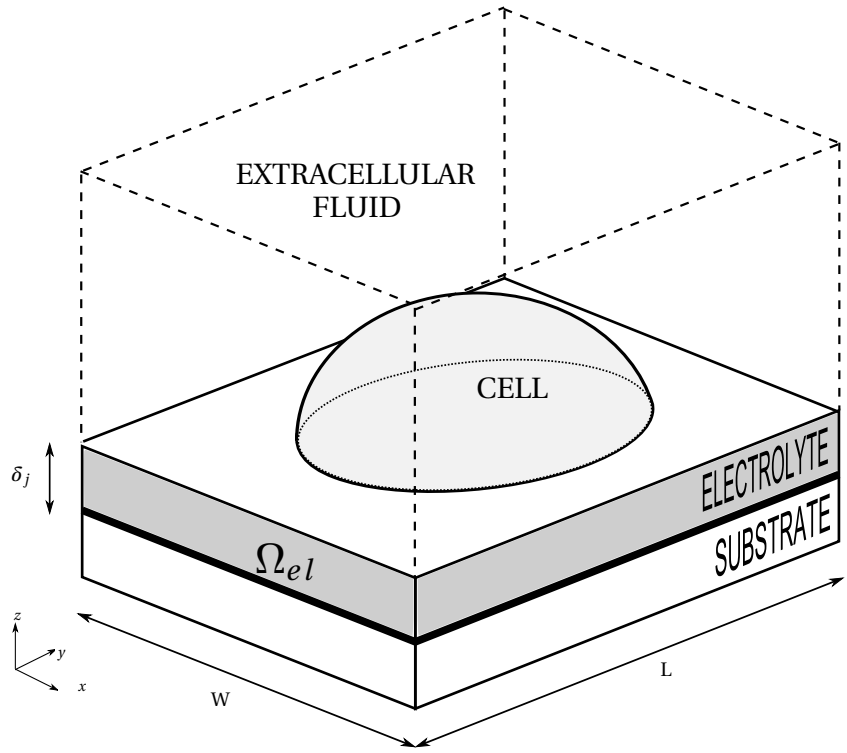

Figure 2.2.1 – Geometrical model: a cell surrounded by an electrolyte bath is attached on an electronic device. The thin layer of electrolyte between the cell and the substrate is the considered mathematical domain Ω_{el}.

opening and closing of the membrane channels, which are the major responsibles of the physical phenomena.

2.2.1 Geometrical model

Fig. 2.2.1 illustrates the three dimensional physical domain considered in this section: the cell shape has been simplified to a smooth rotational solid and the representation of the electronic substrate internal structure is neglected, as it will be in all the models we are going to consider in the present work (see also [31, 32, 3, 38, 4]). The extracellular fluid is surrounding all the cell, but the computational domain we are going to refer to from now on is the layer Ω_{el}, a thin sheet of electrolyte bath, which includes the cleft between the attached area of the cell and the device, but also the part of electrolyte in the neighborhood of the cell. We are dealing with a layer thickness δ_j of the order of $50 \div 100$ nm, while the cell radius is assumed to be around $10\,\mu$m in the applications we are investigating [3, 5, 38].

2.2.2 The Poisson-Nernst-Planck system

The Poisson-Nernst-Planck (PNP) system serves as basic electrodiffusion model for the motion of chemical species in a fluid medium, for example the ion flow through membrane channels and the transport of holes and electrons in semiconductors, and is also applicable to the ion flow in the electrolyte bath surrounding the cell. Therefore, as in [3, 14, 33, 38], we apply the PNP model to study ion flow in the region Ω_{el} in order to determine the potential φ (V) and the concentration c_i (m^{-3}) of each ion in the electrolyte. The basic assumption of the PNP system is that the substances in the aqueous electrolyte medium are subject to two main forces: thermodynamical or diffusion forces and electrical or drift forces.

Considering M ion species in the three dimensional domain Ω_{el}, one can write the following equations [44]:

$$
\begin{aligned}
qz_i\frac{\partial c_i}{\partial t}+\mathrm{div}\,\mathbf{j}_i\left(c_i,\varphi\right) &= 0 && i=1,...,M && \text{(2.1a)}\\
\mathbf{j}_i\left(c_i,\varphi\right) &= q|z_i|\mu_i c_i\mathbf{E}-qz_iD_i\nabla c_i && i=1,...,M && \text{(2.1b)}\\
\mathrm{div}\,\mathbf{E} &= \frac{q}{\epsilon}\sum_i z_i c_i && && \text{(2.1c)}\\
\mathbf{E} &= -\nabla\varphi && && \text{(2.1d)}\\
D_i &= \frac{\mu_i V_{th}}{|z_i|} && i=1,...,M. && \text{(2.1e)}
\end{aligned}
$$

The first one (2.1a) is the continuity equation (one for each ion), describing the conservation of electric charge. Mathematically, it states that the divergence of the current density $\mathbf{j}_i$ ($\mathrm{A\,m}^{-2}$) is equal to the negative time rate of change of the charge density $\rho_i = qz_ic_i$ ($\mathrm{C\,m}^{-3}$). A current is a movement of charge and this description states that if charge is moving out of a differential volume, then the amount of it within that volume is going to decrease. Here q is the elementary charge and z_i is the valence of the ion species.

Each ion current density is defined in (2.1b), the Nernst-Planck relation. This is a simplified momentum conservation equation, where the flow of ions is driven by the superposition of their concentration gradients ∇c_i and by the electric field $\mathbf{E}$ ($\mathrm{V\,m}^{-1}$) defined in (2.1d). It is then possible to recognize in (2.1b) both the chemical and the electric contributions influencing the flux, so that the model extends Fick's law of diffusion to the case where the diffusing particles are also moved by electrostatic forces with respect to the fluid. μ_i and D_i are respectively the mobility ($\mathrm{m^2\,V^{-1}\,s^{-1}}$) and the diffusivity ($\mathrm{m^2\,s^{-1}}$) of the chemical species. These two last physical quantities

are related by the fundamental Einstein relation (2.1e), which describes the diffusion of a particle in an electric field, where $V_{th} = k_B T/q$ is the thermal potential (k_B is the Boltzmann constant and T is the absolute temperature).

The electric field is governed by the ion concentrations through the Poisson equation for electrostatics (2.1c). Substituting the electric field (the electrolyte dielectric constant is $\epsilon = \epsilon_0 \epsilon_r$) one obtains the usual form

$$-\epsilon \triangle \varphi = \rho,$$

where the total charge density ρ is defined as

$$\rho = \sum_i \rho_i = \sum_i q z_i c_i.$$

The PNP system (2.1) has the same format and structure as the Drift-Diffusion (DD) equations for semiconductors [25], but it is applied to a different medium (water instead of a semiconductor crystal lattice) and, in most of the cases, one needs to consider more charge carriers than just holes and electrons, as in the case of semiconductor device theory.

Adding together the M continuity equations (2.1a), we obtain

$$\sum_i q z_i \frac{\partial c_i}{\partial t} + \sum_i \mathrm{div}\, \mathbf{j}_i = 0,$$

and then using the Poisson equation (2.1c) we get

$$\epsilon \frac{\partial}{\partial t} \mathrm{div}\, \mathbf{E} + \mathrm{div} \sum_i \mathbf{j}_i = 0. \tag{2.2}$$

Relation (2.2) suggests the introduction of a total current density, as the following definition shows

$$\mathbf{j}_{tot} = \mathbf{j}^{disp} + \mathbf{j}^{cond}_{tot} = \epsilon \frac{\partial \mathbf{E}}{\partial t} + \sum_i \mathbf{j}_i,$$

where we recognize a displacement current term, given by the time derivative of the electric field **E**, and a total conductivity current term, given by each ion Nernst-Planck current. Therefore, exchanging the space and the time derivatives, (2.2) becomes now

$$\mathrm{div}\, \mathbf{j}_{tot} = 0,$$

which shows that the total current density (conduction current plus displacement

current) is solenoidal.

For numerical purposes, the PNP model can be reformulated introducing the mass flux $\mathbf{f}_i$ ($\mathrm{m}^{-2}\,\mathrm{s}^{-1}$) for each ion species, defined as

$$\mathbf{f}_i := \frac{\mathbf{j}_i}{q z_i} \qquad i = 1, ..., M. \tag{2.3}$$

By doing so, the PNP system reads as follows [14]:

$$\begin{aligned}
\frac{\partial c_i}{\partial t} + \mathrm{div}\,\mathbf{f}_i\left(c_i, \varphi\right) &= 0 && i = 1, ..., M && \text{(2.4a)}\\
\mathbf{f}_i\left(c_i, \varphi\right) &= z_i \mu_i c_i \mathbf{E} - D_i \nabla c_i && i = 1, ..., M && \text{(2.4b)}\\
\mathrm{div}\,\mathbf{E} &= \frac{q}{\epsilon} \sum_i z_i c_i && && \text{(2.4c)}\\
\mathbf{E} &= -\nabla \varphi && && \text{(2.4d)}\\
D_i &= \frac{\mu_i V_{th}}{|z_i|} && i = 1, ..., M. && \text{(2.4e)}
\end{aligned}$$

This is the model we will refer to from now on. Of course, to recover the current density $\mathbf{j}_i$ for each ion, we can use (2.3) as a post-processing formula.

2.2.3 Boundary and initial conditions

The concentrations $c_i = c_i(t, \mathbf{x})$ and the potential $\varphi = \varphi(t, \mathbf{x})$ are unknown functions of both time t and space $\mathbf{x}$ (the spatial coordinate with respect to a fixed frame of reference). Thus, we need to impose an initial condition at time $t = 0$ and boundary conditions on $\partial\Omega_{el}$ to complete the three dimensional model (2.4).

The initial conditions $c_i^0(\mathbf{x}) = c_i(0, \mathbf{x})$ and $\varphi^0(\mathbf{x}) = \varphi(0, \mathbf{x})$ are determined by solving the static version of the PNP system (2.4) in the domain Ω_{el}, which corresponds to setting $\frac{\partial c_i}{\partial t} = 0$ in (2.4a) for each ion $i = 1, ...M$.

The boundary conditions need a more thorough discussion: they are required to complete the mathematical model describing the whole considered physical system. The domain Ω_{el} is reduced to a thin layer of electrolyte (the parallelepiped shown in Fig. 2.2.2), but it is essential to remember the presence of a cell over it and of an electronic device under it and that they have a major role in the overall behavior of the coupled bio-electronic system. All around the cell there is also an electrolytic bath identical to the one in the cleft area, therefore we need to take into account that there can be exchange of ions between the portion of electrolyte considered and all the environment surrounding the cell and the substrate (of Fig. 2.2.1). We assume

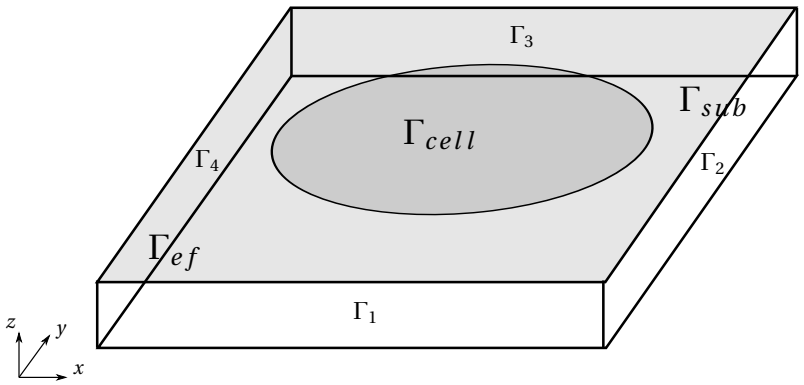

Figure 2.2.2 – Three dimensional domain Ω_{el}. Seven different boundary regions are distinguished: the upper surface is divided in Γ_{cell} (the cell attachment area) and Γ_{ef} (surface dividing electrolyte from electrolyte).

that far away from the cell the electrolyte is a neutral solution, in such a way that the following electroneutrality condition holds

$$\rho_{bath} = q \sum_{i=1}^{M} z_i c_i^{bath} = 0. \tag{2.5}$$

The corresponding potential V_{bath} is then computed using the concentrations c_i^{bath} in (2.4c)-(2.4d): this value can be interpreted as the reference value of an electrode located in the electrolyte nearby the cell.

Then, in defining boundary conditions, as shown in Fig. 2.2.2, we distinguish among seven different regions (the domain is a parallelepiped, but the upper face can be divided into two areas: the attached area Γ_{cell} and the free one Γ_{ef}, covered by the surrounding part of extracellular fluid). Accordingly, the following conditions are enforced on the electric field and the particle fluxes:

$$\begin{aligned}
\varphi &= V_{bath} && \text{on } \Gamma_1 \cup \Gamma_2 \cup \Gamma_3 \cup \Gamma_4 && \text{(2.6a)}\\
[\![\mathbf{D}\cdot\mathbf{n}]\!]_{\Gamma_{ef}} &= 0 && \text{on } \Gamma_{ef} && \text{(2.6b)}\\
[\![\mathbf{D}\cdot\mathbf{n}]\!]_{\Gamma_{cell}} &= 0 && \text{on } \Gamma_{cell} && \text{(2.6c)}\\
[\![\mathbf{D}\cdot\mathbf{n}]\!]_{\Gamma_{sub}} &= 0 && \text{on } \Gamma_{sub} && \text{(2.6d)}
\end{aligned}$$

$$\begin{aligned}
c_i &= c_i^{bath} && \text{on } \Gamma_1 \cup \Gamma_2 \cup \Gamma_3 \cup \Gamma_4 && \text{(2.6e)}\\
[\![\mathbf{f}_i\cdot\mathbf{n}]\!]_{\Gamma_{ef}} &= 0 && \text{on } \Gamma_{ef} && \text{(2.6f)}\\
[\![\mathbf{f}_i\cdot\mathbf{n}]\!]_{\Gamma_{cell}} &= 0 && \text{on } \Gamma_{cell} && \text{(2.6g)}
\end{aligned}$$

$$\mathbf{f}_i \cdot \mathbf{n} = 0 \qquad \text{on } \Gamma_{sub}. \tag{2.6h}$$

The symbol $[\![\cdot]\!]_\zeta$ denotes the jump operator restricted to the interface ζ.

Conditions (2.6a) and (2.6e) are Dirichlet boundary conditions: the concentrations are fixed at the same value as the electrolyte concentrations and the potential is fixed at the reference value V_{bath}. These can be interpreted as "far field conditions" for the considered variables, consistently with the fact that the side faces of Ω_{el} (Γ_1, Γ_2, Γ_3 and Γ_4) are sufficiently far away from the surface where the cell is attached to the substrate.

A little more accurate discussion is required for Γ_{cell} and Γ_{sub}, which are the surfaces attached to the cell membrane and to the electronic device, respectively. In order to describe this complex bio-hybrid system one has to introduce suitable coupling conditions representing the presence of the cell and the substrate. On Γ_{cell} there is conservation of the normal electric field and of the normal component of the ionic fluxes, namely both the jumps of the displacement vector and of the current densities are set equal to zero (conditions (2.6c) and (2.6g)). This tells us that there is continuity between the variation of the potential and the particle fluxes inside the cell and in the electrolyte in the cleft. For the description of the electronic substrate we need to impose on Γ_{sub} again a null jump of the electric displacement field, but also that there is no ion current injected from the cleft to the device or the other way around, as stated in (2.6h).

The surface Γ_{ef} is the free part of the upper face but we cannot neglect that the ions can flow not only in the thin sheet of electrolyte we are considering, but also in the upper part of the bath surrounding the whole cell, and this is why again both the jumps are set equal to zero in (2.6b) and (2.6f).

2.2.4 Coupling conditions

In this section, we discuss coupling conditions describing the behavior of the electric displacement vector and of the ionic current densities at the interface surfaces separating the various parts of our system.

Cleft-cell coupling

As described in Section 1.2, a cell is an enormously complex structure. Accounting for all its bio-chemical reactions is evidently impossible, hence a drastic modeling reduction must be undertaken. In this work both the interior and exterior of the cell

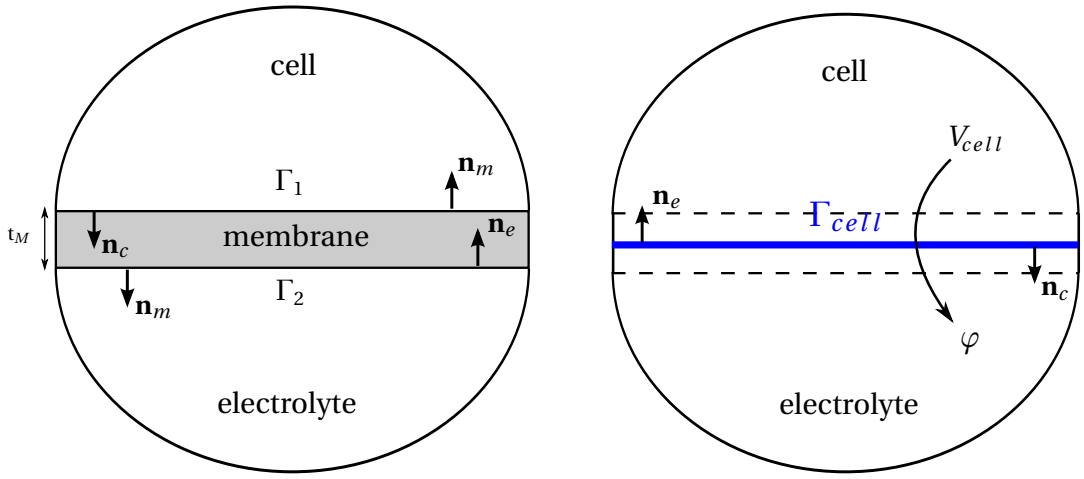

(a) Membrane (b) Lumping in Γ_{cell}

Figure 2.2.3 – On the left: cell and electrolyte separated by the membrane with its physical thickness t_M. On the right: cell and electrolyte separated by an interface Γ_{cell} with zero thickness, result of the lumping of the original boundaries Γ_1 and Γ_2 of the membrane region.

will be described as simple electrolyte solutions. This choice is both due to the need of a computationally feasible model and to the observation that ions and potential are the main physical quantities acting on the bio-electronic interface.

In the present work, most of the physiological phenomena relevant to the considered applications depend upon the cell membrane, which is the communication medium between interior and exterior of the cell. The physical model of the membrane is the sum of two contributions: one from the sole lipid membrane and one from the ionic channels. The lipid membrane is largely impermeable to the ions and can be modeled as a constant specific capacitance C_M ($\mathrm{F\,m^{-2}}$). The main feature of the membrane subdomain (shown in Fig. 2.2.3-(a)) is that the thickness t_M, according to biophysical evidence (it is in the order of $5 \div 10$nm), is much smaller than the characteristic size of the domain (the cell radius). The principal difficulty in the numerical solution of a microscale model accounting for the cell membrane is the geometrical discretization of this small region, which may give rise to a huge number of degrees of freedom of the numerical method. To reduce computational complexity, we have decided to study and apply the membrane model proposed and investigated in [34, 33, 4] in the three dimensional study of cellular electrical activity. This approach consists of a geometrical level and a modeling level.

Geometrically, as shown in Fig. 2.2.3, we need to introduce a two dimensional manifold Γ_{cell} corresponding to the middle cross-section of the membrane volume and to partition the membrane into the union of two disjoint subregions Ω_{m1} and

Ω_{m2} (the two open portions of the membrane respectively in contact with the cell and the cleft) and of Γ_{cell}. At this point we can define "extended" subdomains: the cell, consisting in the union of the cell and of Ω_{m1}, and the electrolyte insiede the cleft, consisting in the union of the cleft and of Ω_{m2}. The new geometrical partition of the cell structure is shown in Fig. 2.2.3-(b).

Going into details for the modeling level, condition (2.6c) can be rewritten as

$$\mathbf{D}_e \cdot \mathbf{n}_e + \mathbf{D}_c \cdot \mathbf{n}_c = 0 \qquad \text{on } \Gamma_{cell}, \tag{2.7}$$

where two outward unit normal vectors $\mathbf{n}_e$ and $\mathbf{n}_c$ are considered: this is actually a transmission condition across the two dimensional manifold Γ_{cell}. The principal assumption in this modeling reduction is that the electric potential varies linearly inside the membrane along the z-direction, so that $\frac{\partial \varphi}{\partial z} \simeq \frac{\varphi(z_1)-\varphi(z_2)}{z_1-z_2}$. This assumption agrees with the fact that t_M is much smaller than the cell radius and, replaced into the transmission condition (2.7), yields

$$\mathbf{D}_c \cdot \mathbf{n}_c = -\mathbf{D}_e \cdot \mathbf{n}_e = -\epsilon_M \frac{\varphi_{m2} - \varphi_{m1}}{\mathrm{t}_M} \simeq -C_M \left(\varphi_{m2} - V_{cell}\right), \tag{2.8}$$

where φ_{m1} and φ_{m2} are the traces of φ at both sides of Γ_{cell}. Moreover, in our simplified model, we consider the intra-cellular potential V_{cell} only as a function of time and not varying in space, because we are not interested in describing the intra-cellular phenomena, as in [5]. We also get a capacitive coupling between the cell and the electrolyte, having defined $C_M = \epsilon_M/\mathrm{t}_M$ as the intrinsic membrane specific capacitance.

To account for the ionic channels, a detailed description of their behavior requires a compromise between accurate physical modeling and computational effort. The types of channels to consider are at most K^+, Ca^{2+}, Na^+ and Cl^- channels, as those four are responsible for the majority of the ionic current in a cellular action potential. In the present work we focus on cells where K^+ channels are the principal inflow/outflow current sources. The ionic current carried by this ionic species needs to be described as a function of a set of controlling variables, namely potential across the channel, ion concentrations and gating variables.

The most general formulation for ion flow through membrane channels is the generalized Hodgkin Huxeley model [20, 21, 33]

$$j_i^{tm} = j_i^{tm}\left(t, \mathbf{x}, \mathbf{s}, V_{cell}, \varphi, \mathbf{c}^{in}, \mathbf{c}^{ext}\right) \tag{2.9}$$

accounting for voltage-gating mechanism of the channels, which in turn permits the

simulation of the propagation of an action potential. The symbol **s** denotes the so called gating variables, while $\mathbf{c}^{in}$ and $\mathbf{c}^{ext}$ are arrays of size M containing all the ions concentrations inside and outside the cell. Evidently, transmembrane injection depends on both potential difference and ionic concentration differences between inside and outside the cell.

The first model we consider is the so called linear resistor model [26]. This is the simplest current-voltage relationship of the form (2.9) and the ionic current density of the i-th ion is expressed as

$$j_i^{tm} = g_{JM}^i \left(\left(V_{cell} - \varphi \right) + \frac{V_{th}}{z_i} \ln \left(\frac{c_i^{cell}}{c_i} \right) \right), \tag{2.10}$$

where g_{JM}^i is the specific transmembrane conductance of the i-th ion ($\mathrm{S\,m^{-2}}$). It multiplies two terms: the first one is the potential difference between inside and outside and the second one is the Nernst potential[1] between the cell and the electrolyte, calculated using internal concentrations c_i^{cell} and unknown concentrations in the electrolyte $c_i = c_i(t,\mathbf{x})$ evaluated at $\mathbf{x} \in \Gamma_{cell}$. This model, although very simple, is quite accurate and successfully used in [3, 5].

The second model adopted in the present work is the Goldman-Hodgkin-Katz (GHK) current equation for ionic channels [19]. The electrodiffusion process across the channel can be expressed as

$$j_i^{tm} = p_i z_i q \left[Be\left(-\frac{z_i \left(V_{cell} - \varphi \right)}{V_{th}} \right) c_i^{cell} - Be\left(\frac{z_i \left(V_{cell} - \varphi \right)}{V_{th}} \right) c_i \right], \tag{2.11}$$

where p_i is the permeability constant of the specific ion ($\mathrm{m\,s^{-1}}$), z_i the valence and $Be(\cdot)$ is the inverse of the Bernoulli function, defined as

$$Be(x) = \frac{x}{e^x - 1}. \tag{2.12}$$

The GHK model describes the flow of ions across the membrane as the result of electrodiffusion processes, where the equivalent diffusion constant in the membrane is accounted for with the permeability constant and the potential is assumed to vary linearly across the membrane. The permeability value is a sensitive parameter to compute for the membrane channels, because there is a stochastic part to account

[1] In electrochemistry the equilibrium potential of each ion species can be calculated using the Nernst equation, which gives $V_i = -\frac{V_{th}}{z_i} \ln\left(\frac{c_i^{int}}{c_i^{ext}}\right)$.

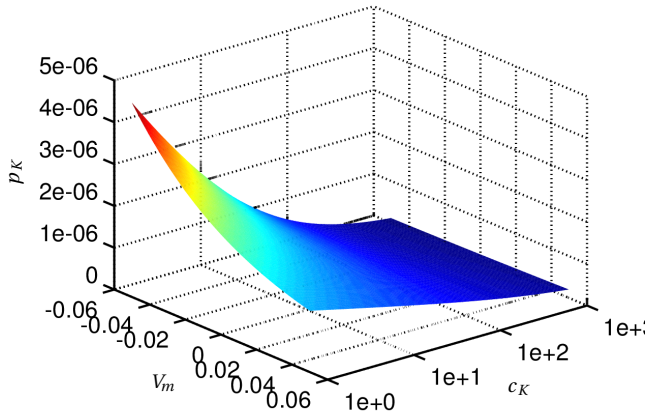

Figure 2.2.4 – Values of potassium membrane permeability p_K (in $\mathrm{m\,s^{-1}}$) as a function of V_m (in V) and c_K (logarithmic axis for the millimolar concentration).

for the opening and closing of these. Its mathematical definition is

$$p_i = \frac{D_i^{eff}}{\mathrm{t}_M}, \tag{2.13}$$

where D_i^{eff} is the effective diffusion coefficient of ion i throughout the membrane. A precise characterization of this latter parameter would require the use of more advanced models than the ones considered in the present work, for example molecular dynamics simulations. In order to provide an immediate and mathematically consistent characterization of p_i, we propose the following approach: we conduct a parametric analysis to find the correct values of p_i by equating expressions (2.10) and (2.11) and studying the permeability as a function of c_i and of the membrane potential $V_m := V_{cell} - \varphi$, resulting in

$$p_i = \frac{g_{JM}^i}{q z_i} \frac{\left(V_m + \frac{V_{th}}{z_i} \ln \frac{c_i^{cell}}{c_i}\right)}{Be\left(-\frac{z_i V_m}{V_{th}}\right) c_i^{cell} - Be\left(\frac{z_i V_m}{V_{th}}\right) c_i}. \tag{2.14}$$

The obtained result for potassium permeability is illustrated in Fig. 2.2.4, where one can observe that a sensible value for the considered problem can be estimated as $2 \div 3 \times 10^{-6}\,\mathrm{m\,s^{-1}}$. This provides a useful indication for the potassium diffusion through the membrane proteins, which can be computed with definition (2.13): the result obtained is of the order of $1 \times 10^{-11}\,\mathrm{m^2\,s^{-1}}$ and this value is significantly smaller than potassium diffusivity in water ($1.96 \times 10^{-9}\,\mathrm{m^2\,s^{-1}}$).

Introducing in the model a transmembrane current density j_i^{tm} for each ion spe-

cies (the current perpendicularly injected into the electrolyte when the transmembrane channels open after a stimulation), condition (2.6g) becomes

$$\mathbf{f}_e^i \cdot \mathbf{n}_e = -\mathbf{f}_c^i \cdot \mathbf{n}_c = -\frac{j_i^{tm}}{q z_i}. \tag{2.15}$$

The negative sign of the last term in (2.15) agrees with the direction of these currents, going from the cell to the domain Ω_{el} in a direction which is perpendicular to Γ_{cell}.

Cleft-substrate coupling

A complete charge transport model (e.g. a Drift-Diffusion model, see [31, 30]) should be used, in principle, to fully describe the electronic substrate and the electrolyte-oxide interface in all of its electro-chemical aspects. This approach, however, would add a huge amount of computational burden to the overall model, not balanced by the benefits obtained in terms of physical accuracy.

Therefore, in the present work, we choose to adopt a lumped equivalent model to treat the semiconductor device, which is assumed to behave as a MOS capacitor having a metal-like gate contact. Furthermore, a simplified coupling model will be considered, namely the action of the electro-chemical bounding of ions at the interface will be neglected. Fig. 2.2.5 illustrates a detailed zoom of the bio–chip area Γ_{sub}: the electronic behavior of the substrate is driven by the ionic current coming from the biological environment and requires a careful characterization.

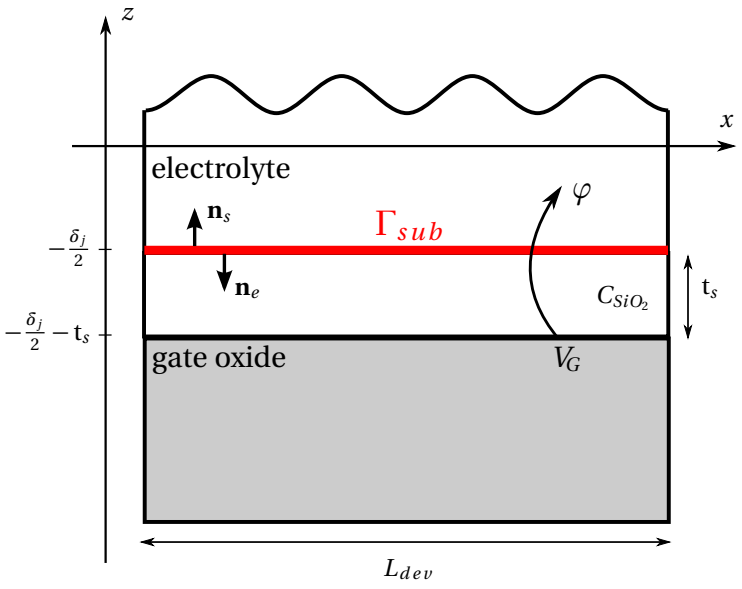

Figure 2.2.5 – Electronic substrate model and coupling with the electrolyte.

In this simplified treatise, the electrical equivalent representation of the structure in Fig. 2.2.5 is just a capacitor, because we neglect the effective electrical behaviour of the device and we do not account for this modeling part (for a detailed description see [3]). The same argument used in (2.8) can be applied on (2.6d), in order to enforce a coupling boundary condition on the potential φ on Γ_{sub}. We are then able to write, at $z = -\frac{\delta_j}{2}$

$$\mathbf{D}_s \cdot \mathbf{n}_s = -\mathbf{D}_e \cdot \mathbf{n}_e \simeq -\epsilon_s \frac{\varphi_{s2} - \varphi_{s1}}{\mathrm{t_S}} = -C_S \left(\varphi_{s2} - V_G\right), \tag{2.16}$$

where we have lumped the thin oxide layer in a similar manner as done for the cell membrane, $\mathrm{t_S}$ and ϵ_S being the region thickness and dielectric constant respectively. We have also assumed that the potential φ in this thin region varies linearly in the z-coordinate. Therefore another capacitive coupling is introduced, with the specific substrate capacitance $C_S = \epsilon_S/\mathrm{t_S}$ (this is the capacitance C_{SiO_2} in the figure, in $\mathrm{F\,m^{-2}}$) and the function $V_G = V_G(t)$ denoting the value of the potential on the gate contact, taken to be spatially constant according to the hypothesis of ideal metallic behaviour of the gate. Here φ_{s1} and φ_{s2} are the traces of φ on both sides of Γ_{sub}.

Electrolyte-electrolyte artificial coupling

In our geometrical representation, as shown in Fig. 2.2.1, we are focusing on a thin electrolyte sheet with the amplitude δ_j of the cleft. This is of course an approximation, because the whole electrolyte surrounding the cell should be studied, not just the layer under it: namely, the ions are free to flow in the entire bath, not just in the considered part. This geometrical approximation leads us to carefully think of the boundary condition to impose on the part that is called Γ_{ef}, depicted in Fig. 2.2.6, which is a fictitious boundary, not actually separating two different media.

We need to incorporate this physical flow in the model, through boundary conditions on the mass fluxes and on the electric field: this is the the aim of conditions (2.6b) and (2.6f), having set to zero the jumps of the electric field and of the currents across Γ_{ef}. These can be treated with a similar procedure as the one described for the cell membrane, ending up with a capacitive coupling and an injected current.

Beginning with the displacement vector, we can rewrite condition (2.6b) as

$$\mathbf{D}_{int} \cdot \mathbf{n}_{int} + \mathbf{D}_{ext} \cdot \mathbf{n}_{ext} = 0 \qquad \text{on } \Gamma_{ef},$$

where the subscripts indicate the internal part of electrolyte in Ω_{el} and the external one (see Fig. 2.2.6). Again assuming that the potential is a linear function of the z-

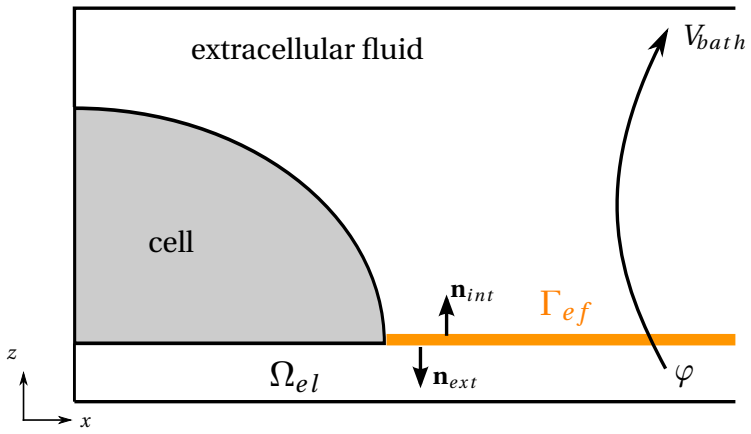

Figure 2.2.6 – Cross section in the x-z plane of the electrolyte bath, illustrating the coupling condition between Ω_{el} and the external remaining electrolyte imposed on Γ_{ef}.

direction, as for (2.8), we obtain

$$\mathbf{D}_{ext} \cdot \mathbf{n}_{ext} = -\mathbf{D}_{int} \cdot \mathbf{n}_{int} \simeq -C\left(\varphi_{int} - \varphi_{ext}\right), \tag{2.17}$$

where φ_{int} and φ_{ext} are the traces of φ respectively on the two sides of Γ_{ef}. This capacitive coupling is identical to the ones introduced for the membrane and for the substrate, but here we have to perform a further lumping procedure. Clearly the potential is changing also in the part of electrolyte outside our domain Ω_{el}, but we are not interested in its distribution. Then, we can assume that far away from the boundary Γ_{ef} the potential is at the reference value V_{bath} and, consistently, capacitive condition (2.17) becomes

$$\mathbf{D}_{int} \cdot \mathbf{n}_{int} \simeq C^*\left(\varphi_{int} - V_{bath}\right), \tag{2.18}$$

where C^* is a fictitious capacitance introduced to relate the external and the internal potential in the electrolyte. The value of C^* cannot be calculated as for C_M and C_S using a thickness and a dielectric constant, because there is no physical membrane at Γ_{ef}. A possible modeling approach consists in using the value of C_M and taking a fraction $1/\kappa$ of it: in this work we have studied the change of the phenomena as a function of this parameter and we have come to the conclusion that an appropriate value for κ can be $\simeq 1000$, as explained in Section 4.2.

Regarding the particle fluxes, one has to imagine that the ions can flow everywhere in the bath and we have to make sure that this physical behaviour is respected by our mathematical model. This is the reason why taking null fluxes would be a wrong assumption and would lead to unphysical results. The condition we are going

to impose is again the result of a lumping procedure: the ions tends to distribuite themselves in order to balance their charges with other species and are moved by the electrical field. Therefore, the normal component of their fluxes will be proportional to the difference between their concentrations over and under Γ_{ef}. Rewriting condition (2.6f) in the following way

$$\mathbf{f}^i_{ext} \cdot \mathbf{n}_{ext} + \mathbf{f}^i_{int} \cdot \mathbf{n}_{int} = 0 \qquad \text{on } \Gamma_{ef},$$

we can come to this relation

$$\mathbf{f}^i_{ext} \cdot \mathbf{n}_{ext} = -\mathbf{f}^i_{int} \cdot \mathbf{n}_{int} = -v_i \left(c_i^{int} - c_i^{ext} \right). \tag{2.19}$$

As in the case of the potential, we assume that far away the concentrations can be considered to be at their bath value c_i^{bath} and the electrolyte to be electroneutral. Then, using the bath values c_i^{bath} for c_i^{ext} in (2.19), we obtain

$$\mathbf{f}^i_{int} \cdot \mathbf{n}_{int} = v_i^* \left(c_i^{int} - c_i^{bath} \right). \tag{2.20}$$

Mathematically, v_i^* can be considered as a factor which mul the difference between the concentrations, amplifying or reducing this flux, but physically it has the dimensions of a velocity ($\mathrm{m\,s^{-1}}$). For this reason one can think of it as an "effective" permeability coefficient and model it by equating flux (2.20) to a fraction $1/\kappa$ of the flux

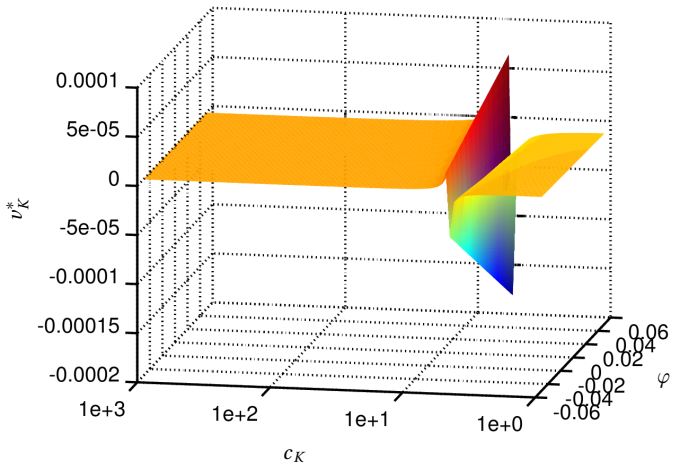

Figure 2.2.7 – Values of potassium parameter v_K^* (in $\mathrm{m\,s^{-1}}$) as a function of φ (in V) and c_K (logarithmic axis for the millimolar concentration), with $\kappa = 20$ in (2.21).

through the membrane (2.15), in the following way

$$\mathbf{f}_i \cdot \mathbf{n}|_{\Gamma_{ef}} = \frac{1}{\kappa_i} \mathbf{f}_i \cdot \mathbf{n}|_{\Gamma_{cell}} . \tag{2.21}$$

As in (2.14), we can write v_i^* as a function of φ and c_i

$$v_i^* = \frac{z_i p_i}{\kappa_i} \frac{Be\left(-z_i \frac{V_{cell}-\varphi}{V_{th}}\right) c_i^{cell} - Be\left(z_i \frac{V_{cell}-\varphi}{V_{th}}\right) c_i}{c_i - c_i^{bath}}.$$

Again conducting a parametric analysis (see Section 4.2.1), we have come to the conclusion that a reasonable value for v^* can be determined by taking $\kappa = 20$ in (2.21), as shown in Fig. 2.2.7.

2.2.5 General framework for boundary conditions

At the end of this discussion we can now summarize the boundary conditions in a general framework that we will apply to every considered geometrical setting, in both three and two dimensional cases. A part of $\partial\Omega_{el}$, denoted by Γ_b and given by the union of Γ_1, Γ_2, Γ_3 and Γ_4 in Fig. 2.2.2, is set to the bath reference values with Dirichlet boundary conditions for the potential and the concentrations.

The description of the cell and of the electronic substrate is represented through Robin coupling boundary conditions, on Γ_{cell} and Γ_{sub} respectively, and an analogous argument is applied to the surface Γ_{ef}, as analyzed in the previous paragraphs. We then have a remaining part denoted Γ_N, where Neumann homogeneous condi-

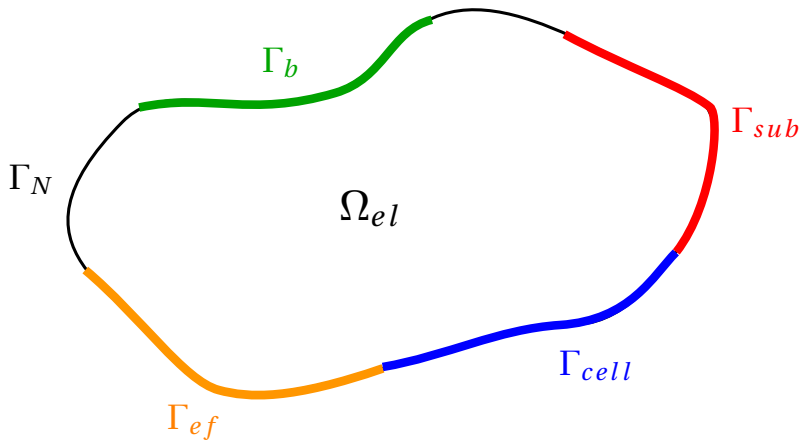

Figure 2.2.8 – General framework for boundary conditions applied to different problems and geometries.

tions for all variables hold, as in the case where the geometry requires symmetry conditions, as discussed in Section 4.1.

Referring to the notation of Fig. 2.2.8, for the Poisson problem we have the following conditions:

$$\begin{cases} \mathbf{D}\cdot\mathbf{n} = C_M\left(\varphi - V_{cell}\right) & \text{on } \Gamma_{cell} \\ \mathbf{D}\cdot\mathbf{n} = C_S\left(\varphi - V_{sub}\right) & \text{on } \Gamma_{sub} \\ \mathbf{D}\cdot\mathbf{n} = C^*\left(\varphi - V_{bath}\right) & \text{on } \Gamma_{ef} \\ \mathbf{D}\cdot\mathbf{n} = 0 & \text{on } \Gamma_N \\ \varphi = V_{bath} & \text{on } \Gamma_b, \end{cases} \tag{2.22}$$

while for the continuity equations we have:

$$\begin{cases} \mathbf{f}_i\cdot\mathbf{n} = -\dfrac{j_i^{tm}}{qz_i} & \text{on } \Gamma_{cell} \\ \mathbf{f}_i\cdot\mathbf{n} = 0 & \text{on } \Gamma_{sub} \\ \mathbf{f}_i\cdot\mathbf{n} = v^*\left(c_i - c_i^{bath}\right) & \text{on } \Gamma_{ef} \\ \mathbf{f}_i\cdot\mathbf{n} = 0 & \text{on } \Gamma_N \\ c_i = c_i^{bath} & \text{on } \Gamma_b. \end{cases} \tag{2.23}$$

2.3 Hierarchical models

The goal of the present work is to describe the ion flow and the distribution of the electrical potential in the cleft between the cell and the device. This problem, naturally, requires a three dimensional description, but in this section we derive a suitable two dimensional mathematical model, thanks to an appropriate geometrical reduction, whose aim is to gain in computational time without losing accuracy.

In order to reduce the model to a two dimensional form [5, 38], we have to consider the physical phenomena we are investigating. The opening of the transmembrane channels elicits ion currents: considering a cell with only potassium channels, we have a K^+ ion flow in the electrolyte, which causes an increase of positive charge in the cleft. Because of the resulting electric field, other ions start to move: positive ions leave the cleft and move into the surrounding bath solution, while negative ions are attracted and enter the cleft. Connected with this ion flux is a change in the concentration of the different species inside the cleft.

In physical experiments, K^+ ions enter the cleft across the membrane with a cur-

rent density vector more or less parallel to the z-axis and then, inside the cleft, the direction of the ion current density changes into the radial direction. The time needed to flow across the cleft height is of the order of 10^{-7} s (we are considering a diffusivity $D_K = 2 \times 10^{-9}\,\mathrm{m^2\,s^{-1}}$) and because the ratio between the cleft thickness and the radius of the attached area is of the order of 10^{-3}, the ions move many times up and down in the z-direction over the cleft height before leaving the cleft. The same considerations are valid for all the other considered ion species. The average of this random motion in the z-direction over an appropriate time interval (order of μs) gives a zero current density $\langle j_{i,z} \rangle_{time} = 0$ inside the cleft. With respect to this, we can build a two dimensional model neglecting the z-dependence of the physical variables.

In the next pages, we introduce an approximation in the middle plane of the cleft, reducing the three dimensional model into a two dimensional one with an averaging procedure.

2.3.1 Model reduction: from 3D to 2D

The three dimensional domain Ω_{el} is a thin layer of electrolyte (the parallelepiped shown in Fig. 2.2.2), with a height δ_j (cleft thickness) of the order of $50 \div 100$ nm. In order to reduce the model, a coordinate system with the origin in the middle of Ω_{el} should be placed. The plane in the middle of the cell-chip junction, depicted in Fig. 2.3.1, is going to be the new two dimensional domain Ω_{2D}: it is equidistant from Γ_{sub} and from $\Gamma_{el} \cup \Gamma_{cell}$, which are respectively placed at $z = -\delta_j/2$ and $z = +\delta_j/2$.

We follow a procedure based on the integration of the three dimensional equations (2.4) on the test volume of Fig. 2.3.1: this domain of integration is a parallelepiped with a volume $V_{xy} = \delta_j h_x h_y$, where h_x and h_y are infinitesimal. Then, we can introduce the following integral mean for the quantities of interest, here written for a generic function $u = u(t;x,y,z)$

$$\overline{u}\,(t;x,y) = \frac{\int_{-\delta/2}^{\delta/2} u\,(t;x,y,z)\,dz}{\delta_j}. \tag{2.24}$$

Beginning the model reduction with the continuity equations (2.4a) for each ion, we integrate them in the test volume V_{xy}

$$\int_{V_{xy}} \frac{\partial c_i}{\partial t} dV + \int_{V_{xy}} \mathrm{div}\mathbf{f}_i\, dV = 0.$$

We can use the Stokes theorem on the second term and obtain the surface integ-

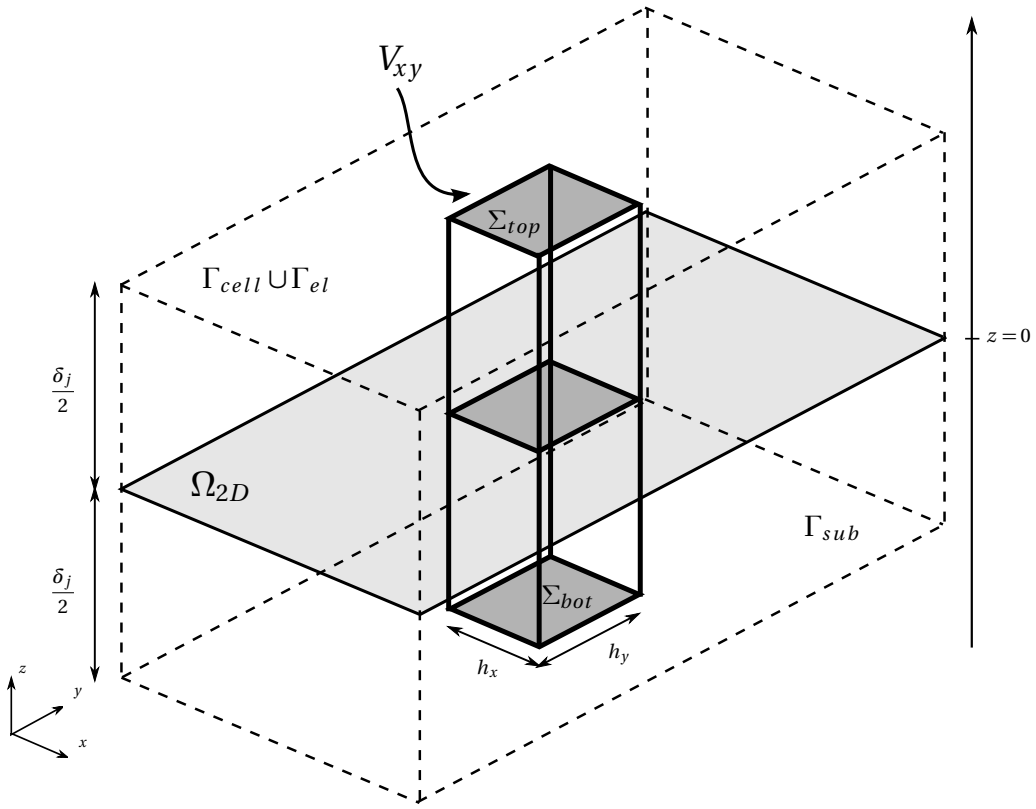

Figure 2.3.1 – Schematics for the geometrical reduction in the x-y plane: the middle plan of the cleft becomes the two-dimensional domain Ω_{2D}. V_{xy} is a control volume used to compute the integrals and the fluxes.

ral $\int_{\partial V_{xy}} \mathbf{f}_i \cdot \mathbf{n} d\Sigma$. Denoting as f_x, f_y and f_z the components of the fluxes in the three directions, the integral on ∂V_{xy} can be rewritten as sum of the integrals of the corresponding component of the flux on each face of the parallelepiped, having then six different terms

$$\begin{aligned}
&\frac{\partial}{\partial t}\int_{x-\frac{h_x}{2}}^{x+\frac{h_x}{2}} d\xi \int_{y-\frac{h_y}{2}}^{y+\frac{h_y}{2}} d\eta \int_{-\frac{\delta_j}{2}}^{\frac{\delta_j}{2}} dz\, c_i\left(t;\xi,\eta,z\right) \\
&\quad + \int_{y-\frac{h_y}{2}}^{y+\frac{h_y}{2}} d\eta \int_{-\frac{\delta_j}{2}}^{\frac{\delta_j}{2}} dz\, \mathrm{f}_x^i\left(t;\xi+\frac{h_x}{2},\eta,z\right) - \int_{y-\frac{h_y}{2}}^{y+\frac{h_y}{2}} d\eta \int_{-\frac{\delta_j}{2}}^{\frac{\delta_j}{2}} dz\, \mathrm{f}_x^i\left(t;\xi-\frac{h_x}{2},\eta,z\right) \\
&\quad + \int_{x-\frac{h_x}{2}}^{x+\frac{h_x}{2}} d\xi \int_{-\frac{\delta_j}{2}}^{\frac{\delta_j}{2}} dz\, \mathrm{f}_y^i\left(t;\xi,\eta+\frac{h_y}{2},z\right) - \int_{x-\frac{h_x}{2}}^{x+\frac{h_x}{2}} d\xi \int_{-\frac{\delta_j}{2}}^{\frac{\delta_j}{2}} dz\, \mathrm{f}_y^i\left(t;\xi,\eta-\frac{h_y}{2},z\right) \\
&\quad + \int_{x-\frac{h_x}{2}}^{x+\frac{h_x}{2}} d\xi \int_{y-\frac{h_y}{2}}^{y+\frac{h_y}{2}} d\eta\, \mathrm{f}_z^i\left(t;\xi,\eta,\frac{\delta_j}{2}\right) - \int_{x-\frac{h_x}{2}}^{x+\frac{h_x}{2}} d\xi \int_{y-\frac{h_y}{2}}^{y+\frac{h_y}{2}} d\eta\, \mathrm{f}_z^i\left(t;\xi,\eta,-\frac{\delta_j}{2}\right) = 0.
\end{aligned}$$

Each one of the surface integrals can be approximated with the baricentric formula

and we can use (2.24) on the first term with the time derivative, obtaining the following average expression

$$\begin{aligned}\frac{\partial \overline{c}_i}{\partial t}\delta_j h_x h_y &+ \mathrm{f}_x^i\left(t; x+\frac{h_x}{2}, y, 0\right)\delta_j h_y - \mathrm{f}_x^i\left(t; x-\frac{h_x}{2}, y, 0\right)\delta_j h_y \\ &+ \mathrm{f}_y^i\left(t; x, y+\frac{h_y}{2}, 0\right)\delta_j h_x - \mathrm{f}_y^i\left(t; x, y-\frac{h_y}{2}, 0\right)\delta_j h_x \\ &+ \mathrm{f}_z^i\left(t; x, y, \frac{\delta_j}{2}\right)h_x h_y - \mathrm{f}_z^i\left(t; x, y, -\frac{\delta_j}{2}\right)h_x h_y = 0. \end{aligned} \tag{2.25}$$

We need to be careful with the last two terms, because the value of the flux $\mathbf{f}_i$ on Σ_{top} and Σ_{bot} (respectively the upper and lower basis of the parallelepiped V_{xy}) is unknown and needs in turn to be computed according to the boundary conditions applied on these surfaces. For the purpose of deriving a general two dimensional model, we rewrite the boundary conditions on the two considered surfaces as:

$$\mathbf{f}_i \cdot \mathbf{n} = f_i^{top}\left(t; c_i^{top}, \overline{c}_i, \varphi_{top}, \overline{\varphi}\right) \qquad \text{on } \Sigma_{top} \tag{2.26a}$$

$$\mathbf{f}_i \cdot \mathbf{n} = f_i^{bot}\left(t; c_i^{bot}, \overline{c}_i, \varphi_{bot}, \overline{\varphi}\right) \qquad \text{on } \Sigma_{bot}, \tag{2.26b}$$

where we have introduced two functions f_i^{top} and f_i^{bot} (not necessarily linear, because we use non linear transmembrane current models). These latter functions depend on the "averaged" quantities $\overline{c}_i$ and $\overline{\varphi}$ computed as in (2.24), but also on the quantities eveluated on the surfaces Σ_{top} and Σ_{bot}, defined as:

$$c_i^{top} := c_i|_{\Sigma_{top}} \qquad c_i^{bot} := c_i|_{\Sigma_{bot}} \tag{2.27}$$

$$\varphi_{top} := \varphi\big|_{\Sigma_{top}} \qquad \varphi_{bot} := \varphi\big|_{\Sigma_{bot}}. \tag{2.28}$$

Dividing expression (2.25) by $\left|V_{xy}\right| = \delta_j h_x h_y$ and taking the limit $h_x, h_y \to 0$, we obtain the following general expression for the two dimensional continuity equations in Ω_{2D}:

$$\frac{\partial \overline{c}_i}{\partial t} + \mathrm{div}_{xy}\bar{\mathbf{f}}_i + \frac{1}{\delta_j} f_i^{top} + \frac{1}{\delta_j} f_i^{bot} = 0 \tag{2.29a}$$

$$\bar{\mathbf{f}}_i = -D_i\left(\nabla_{xy}\overline{c}_i + \frac{z_i}{V_{th}}\overline{c}_i \nabla_{xy}\overline{\varphi}\right). \tag{2.29b}$$

The boundary conditions applied on $\partial\Omega_{2D}$ simply reduce to

$$\overline{c}_i = c_i^{bath} \tag{2.29c}$$

because $\partial\Omega_{2D}$ is now a one dimensional manifold, part of the two dimensional surfaces Γ_1, Γ_2, Γ_3 and Γ_4 of Fig. 2.2.2, which were set to the bath values with Dirichlet boundary conditions.

All the same approximations and reasoning applied above to the continuity equations can be applied also to the Poisson equation, again integrating it in the test volume V_{xy} and using the Stokes theorem and the baricentric formula. We need again to rewrite the boundary conditions on the top and the bottom surface in a general form:

$$\mathbf{D}\cdot\mathbf{n} = g_{top}\left(t; c_i^{top}, \overline{c}_i, \varphi_{top}, \overline{\varphi}\right) \qquad \text{on } \Sigma_{top} \tag{2.30a}$$

$$\mathbf{D}\cdot\mathbf{n} = g_{bot}\left(t; c_i^{bot}, \overline{c}_i, \varphi_{bot}, \overline{\varphi}\right) \qquad \text{on } \Sigma_{bot}, \tag{2.30b}$$

where g_{top} and g_{bot} are functions of the unknown quantities defined in (2.24),(2.27) and (2.28). Therefore, we can complete the two dimensional model with this averaged Poisson equation in Ω_{2D}:

$$\mathrm{div}_{xy}\overline{\mathbf{D}} + \frac{1}{\delta_j} g_{top} + \frac{1}{\delta_j} g_{bot} = q\sum_i z_i \overline{c}_i \tag{2.31a}$$

$$\overline{\mathbf{D}} = -\epsilon\nabla_{xy}\overline{\varphi} \tag{2.31b}$$

with the Dirichlet boundary condition on $\partial\Omega_{2D}$, as in (2.29c),

$$\overline{\varphi} = \varphi_{bath}. \tag{2.31c}$$

Having derived a two dimensional model with an averaging procedure, we now need to provide a physical model for the quantities at the upper and at the lower surface introduced in (2.27) and (2.28), in order to close the mathematical formulation. This is the object of the next pages.

Model approximation in the boundary layers

The two dimensional model (2.29) and (2.31) requires the characterization of the functions f_i^{top}, f_i^{bot} and g_{top}, g_{bot} introduced in (2.26) and (2.30). The unknowns for our model are the averaged values $\overline{\varphi}$ and $\overline{c}_i$, but also the top and the bottom values of the potential (2.28) and of the concentrations (2.27), because we need to account for fluxes through the upper and the lower surfaces of the three dimensional domain.

With the purpose of modeling these functions, we use the boundary conditions

of the three dimensional model, discussed in Section 2.2.3. Referring to Fig. 2.3.1, the lower surface is Γ_{sub} and the upper surface is the union of two different parts, Γ_{cell} and Γ_{el}. This decomposition results, in turn, in the decomposition of f_i^{top} and g_{top} as the sum of two different functions in the following way:

$$f_i^{top} = f_{i,top}^{cell}\,\chi_{\Gamma_{cell}} + f_{i,top}^{el}\,\chi_{\Gamma_{el}} \tag{2.32a}$$

$$g_{top} = g_{top}^{cell}\,\chi_{\Gamma_{cell}} + g_{top}^{el}\,\chi_{\Gamma_{el}}, \tag{2.32b}$$

where χ_ζ is the characteristic function of a generic domain $\zeta \subset \mathbb{R}^2$.

Therefore, in the modeling hypotheses, we need to account for the presence of actual physical surfaces, namely the cell membrane and the oxide layer at Γ_{cell} and Γ_{sub}, which should be distinguished from the artificial boundary Γ_{el}.

Regarding Γ_{cell} and Γ_{sub}, we apply to both of them the same approximation, because the coupling conditions are between different environments (the cell and the electrolyte and the device and the electrolyte) and give rise to boundary layers. This behavior is illustrated in Section 4.2, where we show the distributions of potential and concentrations in the *r-z* plane and is also present in literature results as [3, 14, 34]. This actually represents an electrical double layer, namely a structure that appears on the surface of an object when it is exposed to a fluid [16]. The first layer accounts for the ions adhering to the surface due to chemical reactions. The second layer is called "diffuse layer" and is composed of free ions attracted to the surface charge, but that can move in the fluid under the influence of the electric field. As in the Gouy-Chapman approximation [16], we only model the diffuse layer, neglecting the ions attached to the surfaces.

In order to simplify the mathematical treatment of the problem, we consider a fixed value of the coordinate $\bar{y} \in [0; L]$ (see Fig. 2.2.1) and we focus our attention on a *x-z* cross section of the whole three dimensional electrolyte cleft at $y = \bar{y}$. Referring to Fig. 2.3.2, the partition along the z-direction is defined as $\Omega_{xz} = \Omega_1 \cup \Omega_2 \cup \Omega_3$, where $\Omega_1 = \left\{(x,z) \text{ s.t. } z \in \left[\delta_j/2 - H;\, \delta_j/2\right]\right\}$, $\Omega_2 = \left\{(x,z) \text{ s.t. } z \in \left[-\delta_j/2 + H;\, \delta_j/2 - H\right]\right\}$ and $\Omega_3 = \left\{(x,z) \text{ s.t. } z \in \left[-\delta_j/2;\, -\delta_j/2 + H\right]\right\}$, H being the amplitude of the boundary layers. According to physical evidence, for every fixed point $\bar{x}$ of the x axis, we assume that

$$\frac{\partial \varphi(\bar{x},z)}{\partial z} = \frac{\partial c_i(\bar{x},z)}{\partial z} = 0 \quad \text{in } \Omega_2,$$

and we set $\varphi(\bar{x},z) = \overline{\varphi}(\bar{x},z)$ and $c_i(\bar{x},z) = \overline{c}_i(\bar{x},z)$ for all $z \in \Omega_2$. These two definitions amount to extending along the z-direction (in the sole interval Ω_2) the averaged val-

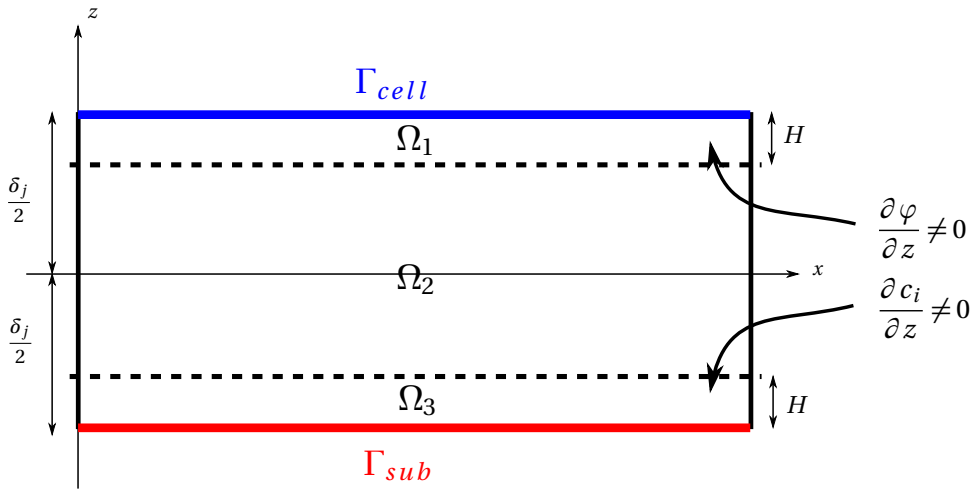

Figure 2.3.2 – Cross section in the x-z plane of the three dimensional cleft, showing the schematics for the modeling hypothesis of the boundary layers near the surfaces Γ_{cell} and Γ_{sub} (H is the layers amplitude).

ues determined by the model described in Section 2.3.1. We also introduce further assumptions on the electric potential and the particle fluxes in the two boundary layer subdomains. Precisely, we assume that:

1. φ is linear in Ω_1 and Ω_3 and continuous at $z = \delta_j/2 - H$ and at $z = -\delta_j/2 + H$;

2. $\mathbf{f}_i$ is constant in Ω_1 and Ω_3.

The spatial distribution of $\varphi(\bar{x}, z)$ for a fixed point $\bar{x}$ is schematically depicted in Fig. 2.3.3-(a). Assumption 1. indicates that the electric field is piecewise constant over Ω_{xz} (and equal to zero in Ω_2). Also the particle fluxes are piecewise constant over Ω_{xz} (and equal to zero in Ω_2 because both drift and diffusion terms are null there).

In order to determine the concentration $c_i(\bar{x}, z)$, we integrate the Nernst-Planck transport equation (2.4b) in Ω_1 and Ω_3. The resulting distribution of ions is piecewise exponential over Ω_{xz}, continuous at $z = \delta_j/2 - H$ and at $z = -\delta_j/2 + H$, and constant in Ω_2 as depicted in Fig. 2.3.3-(b). The corresponding mathematical expressions for the boundary fluxes $f_{i,top}^{cell}$ and f_{bot} are:

$$f_{i,top}^{cell} = -\frac{D_i}{H}\left(Be\left(-\frac{z_i(\varphi_{top} - \overline{\varphi})}{V_{th}}\right)c_i^{top} - Be\left(\frac{z_i(\varphi_{top} - \overline{\varphi})}{V_{th}}\right)\overline{c}_i\right) \quad (2.33a)$$

$$f_i^{bot} = -\frac{D_i}{H}\left(Be\left(\frac{z_i(\overline{\varphi} - \varphi_{bot})}{V_{th}}\right)c_i^{bot} - Be\left(-\frac{z_i(\overline{\varphi} - \varphi_{bot})}{V_{th}}\right)\overline{c}_i\right), \quad (2.33b)$$

where we use again the inverse of the Bernoulli function (2.12). The above described modeling reduction procedure is equivalent to applying the Scharfetter-Gummel (SG)

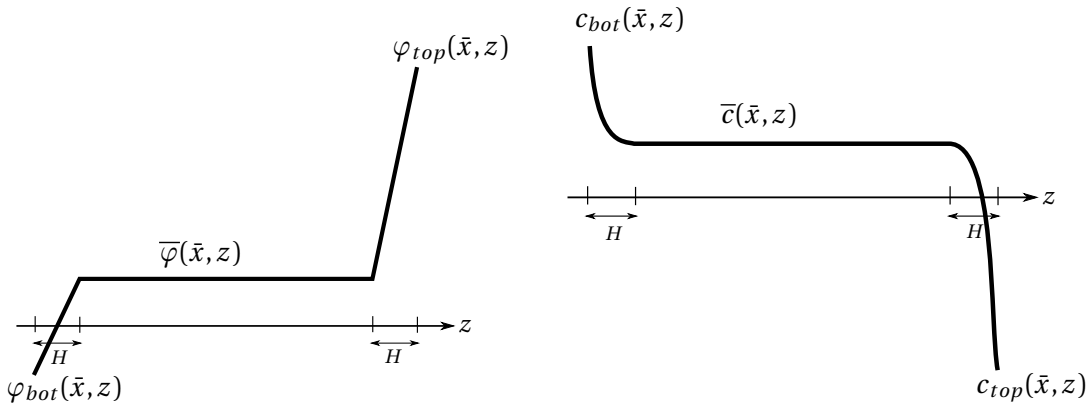

(a) Potential (b) Concentration

Figure 2.3.3 – Schematics of the assumptions on the distributions in the z-direction at a fixed $\bar{x}$ for $\varphi(\bar{x},z)$ and for $c_i(\bar{x},z)$ (where the considered ion is positively charged) for the cross section depicted in Fig. 2.3.2.

exponentially fitted approximation in Ω_1 and Ω_3 [47].

Regarding the electric displacement, with the above approximation we obtain:

$$g_{top}^{cell} = -\epsilon\frac{\varphi_{top}-\overline{\varphi}}{H} \tag{2.33c}$$

$$g_{bot} = -\epsilon\frac{\varphi_{bot}-\overline{\varphi}}{H}. \tag{2.33d}$$

In order to close the mathematical formulation of the system, we need to use the boundary conditions of the three dimensional model. Conditions on the particle fuxes (2.23) give the following expressions for f_i^{top} and f_i^{bot}:

$$f_{i,top}^{cell} = \mathbf{f}_i\cdot\mathbf{n}|_{\Gamma_{cell}} = -\frac{j_i^{top}}{qz_i} \tag{2.34a}$$

$$f_i^{bot} = \mathbf{f}_i\cdot\mathbf{n}|_{\Gamma_{sub}} = 0, \tag{2.34b}$$

where j_i^{top} is the transmembrane current computed at Γ_{cell} using φ_{top} and c_i^{top} . For example, using the resistive model (2.10), we set

$$j_i^{top}(\varphi_{top},c_i^{top}) = g_{JM}^i\left(\left(V_{cell}-\varphi_{top}\right)+\frac{V_{th}}{z_i}\ln\left(\frac{c_i^{cell}}{c_i^{top}}\right)\right). \tag{2.34c}$$

Conditions on the electric displacement (2.22), in turn, give the following relations

for g_{top} and g_{bot}:

$$g_{top}^{cell} = \mathbf{D}\cdot\mathbf{n}|_{\Gamma_{cell}} = C_M\left(\varphi_{top} - V_{cell}\right) \tag{2.34d}$$

$$g_{bot} = \mathbf{D}\cdot\mathbf{n}|_{\Gamma_{sub}} = C_S\left(\varphi_{bot} - V_G\right). \tag{2.34e}$$

Then, by equating the Scharfetter-Gummel expressions (2.33a)-(2.33b) and (2.33c)-(2.33d) with the coupling boundary conditions (2.34a)-(2.34b) and (2.34d)-(2.34e) respectively, we are able to compute , c_i^{top}, c_i^{bot}, φ_{top} and φ_{bot} at Γ_{cell} and Γ_{sub}, ending up with

$$c_i^{top}\Big|_{\Gamma_{cell}} = \frac{1}{Be\left(-z_i(\varphi_{top}-\overline{\varphi})/V_{th}\right)}\left(\overline{c}_i Be\left(z_i(\varphi_{top}-\overline{\varphi})/V_{th}\right) + \frac{j_i^{top}H}{qz_iD_i}\right) \tag{2.35a}$$

$$c_i^{bot}\Big|_{\Gamma_{sub}} = \frac{Be\left(-z_i(\overline{\varphi}-\varphi_{bot})/V_{th}\right)}{Be\left(z_i(\overline{\varphi}-\varphi_{bot})/V_{th}\right)}\overline{c}_i \tag{2.35b}$$

$$\varphi_{top}\Big|_{\Gamma_{cell}} = \frac{1}{C_M+\epsilon/H}\left(C_M V_{cell} + \frac{\epsilon}{H}\overline{\varphi}\right) \tag{2.35c}$$

$$\varphi_{bot}\Big|_{\Gamma_{sub}} = \frac{1}{C_S+\epsilon/H}\left(C_S V_G + \frac{\epsilon}{H}\overline{\varphi}\right). \tag{2.35d}$$

The modeling procedure described so far accounts for the steep layers in the neighbourhood of Γ_{cell} and Γ_{sub}. As anticipated, a different approach is required for the surface Γ_{el}, where the coupling conditions are artificial and we do not have an actual physical surface giving rise to a boundary layer. Therefore, in this part of electroyte, we can assume that the potential and the concentrations are constant along z. We do not need to introduce further relations because we have:

$$\varphi_{top}\Big|_{\Gamma_{el}} = \overline{\varphi} \tag{2.35e}$$

$$c_i^{top}\Big|_{\Gamma_{el}} = \overline{c}_i. \tag{2.35f}$$

The functions $f_{i,top}^{el}$ and g_{top}^{el} introduced in (2.32) are then computed using the electrolyte-electrolyte coupling conditions (2.18) and (2.20) in the following way:

$$f_{i,top}^{el} = v^*\left(\overline{c}_i - c_i^{bath}\right)$$

$$g_{top}^{el} = C^*\left(\overline{\varphi} - V_{bath}\right).$$

The final two dimensional model in Ω_{2D} then reads:

$$\frac{\partial \overline{c}_i}{\partial t} + \mathrm{div}_{xy}\bar{\mathbf{f}}_i + \frac{1}{\delta_j} f_{i,cell}^{top}\, \chi\big|_{\Gamma_{cell}} + \frac{1}{\delta_j} f_i^{bot} + \frac{1}{\delta_j} v^* \left(\overline{c}_i - c_i^{bath}\right) \chi\big|_{\Gamma_{el}} = 0 \tag{2.36a}$$

$$\bar{\mathbf{f}}_i = -D_i(\nabla_{xy}\overline{c}_i + \frac{z_i}{V_{th}}\overline{c}_i \nabla_{xy}\overline{\varphi}) \tag{2.36b}$$

$$\mathrm{div}_{xy}\overline{\mathbf{D}} + \frac{1}{\delta_j} g_{top}^{cell}\, \chi\big|_{\Gamma_{cell}} + \frac{1}{\delta_j} g_{bot} + \frac{1}{\delta_j} C^* \left(\overline{\varphi} - V_{bath}\right) \chi\big|_{\Gamma_{el}} = q \sum_i z_i \overline{c}_i \tag{2.36c}$$

$$\overline{\mathbf{D}} = -\epsilon \nabla_{xy}\overline{\varphi}, \tag{2.36d}$$

to be closed by relations (2.35).

2.3.2 Area contact lumped model

In this section we illustrate the derivation of a model in the same spirit as done by Fromherz et al. in [5, 53], having as starting point the model reduction discussed in Section 2.3.1.

In this version, we focus our attention only on the attached area (the one colored in grey in Fig. 2.3.4, which is our computational domain Ω) as in [5, 38] and consider the quantities $\overline{\varphi} = \varphi\,(x,y;t)$ and $\overline{c_i} = c_i\,(x,y;t)$. In this approximate description, we neglect the variation of the quantities in the z-direction: therefore the functions f_i^{top}, f_i^{bot}, g_{top} and g_{bot} introduced in (2.26) and (2.30) are computed with the three dimensional boundary conditions as if $\varphi_{top} = \varphi_{bot} = \overline{\varphi}$ and $c_i^{top} = c_i^{bot} = \overline{c}_i$.

Neglecting from now on the symbol $\overline{(\cdot)}$ to simplify the notation, we sum the M

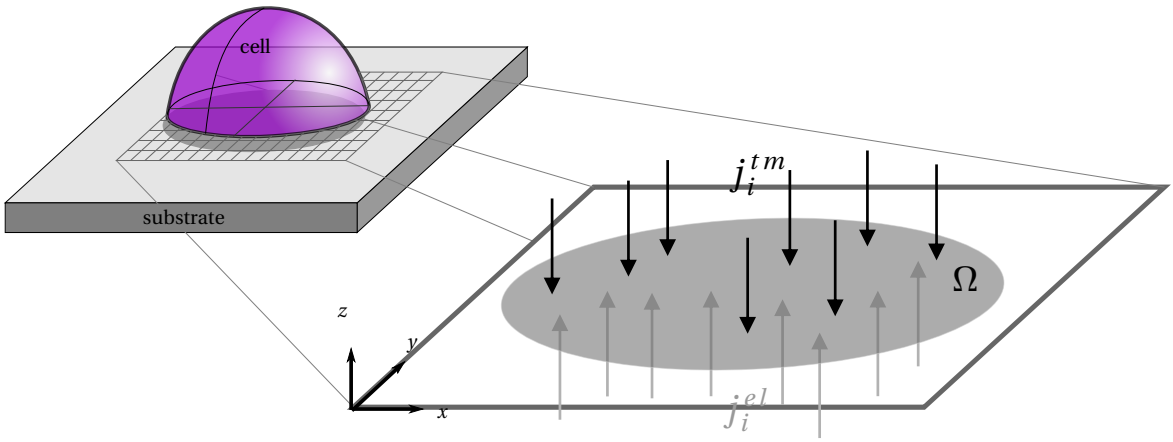

Figure 2.3.4 – Area contact model: reduction in the x-y plane [3].

continuity equations (2.29a) and come to this relation

$$\delta_J \sum_{i=1}^{M} \frac{\partial c_i}{\partial t} + \mathrm{div}_{xy} \mathbf{f}_{tot}^{cond} = \frac{j_{tot}^{tm}}{q}, \tag{2.37}$$

where $\mathbf{f}_{tot}^{cond} = \sum_{i=1}^{M} \mathbf{f}_i \delta_j$. Here the transmembrane current j_i^{tm} for the i-th ion is not computed as in (2.34c), with φ_{top} and c_i^{top}, but using φ and c_i instead.

If the first term is multiplied by q and by each ion valence z_i, one can immediately recognize the time derivative of the surface charge density $\rho\delta_J = q\sum_{i=1}^{M} z_i c_i \delta_J$ ($\mathrm{C\,m^{-2}}$). Using the Poisson equation and the boundary coupling conditions defined for the cell and the substrate in (2.8) and (2.16), we can express the time derivative of ρ in the following way

$$\frac{\partial}{\partial t}\left(\rho\delta_J\right) = \frac{\partial}{\partial t}\left(\mathrm{div}_{xy}\mathbf{D}\right) + \frac{\partial}{\partial t}\left(C_M\varphi + C_S\varphi\right) - \frac{\partial}{\partial t}\left(C_M V_{cell} + C_S V_G\right). \tag{2.38}$$

Then, substituting (2.38) into the sum of the M equations (2.37) (each one multiplied by qz_i), we reach this final result

$$(C_M + C_S)\frac{\partial \varphi}{\partial t} + \mathrm{div}_{xy}\left(\mathbf{j}_{tot}^{cond} + \frac{\partial \mathbf{D}}{\partial t}\right) = j_{tot}^{tm} + \frac{\partial}{\partial t}\left(C_M V_{cell} + C_S V_G\right). \tag{2.39}$$

We can rewrite (2.39) in the following way

$$(C_M + C_S)\frac{\partial \varphi}{\partial t} + \mathrm{div}_{xy}\mathbf{j}_{tot} = j_{tot}^{tm} + \frac{\partial}{\partial t}\left(C_M V_{cell} + C_S V_G\right),$$

with the introduction of the current per unit length ($\mathrm{A\,m^{-1}}$)

$$\mathbf{j}_{tot} = \mathbf{j}_{tot}^{cond} + \frac{\partial \mathbf{D}}{\partial t} = \sigma_{el}\mathbf{E} + \epsilon\frac{\partial \mathbf{E}}{\partial t}. \tag{2.40}$$

As one can see, this conduction current is the sum of each ion currents

$$\mathbf{j}_{tot}^{cond} = q\sum_i |z_i|\mu_i c_i \delta_J \mathbf{E} = \sum_i \sigma_i^{el}\mathbf{E}, \tag{2.41}$$

where σ_i^{el} is the conductance of the i-th ion. Using the expression of the electric field as $\mathbf{E} = -\nabla\varphi$, we rewrite (2.39) and (2.41) as

$$(C_M + C_S)\frac{\partial \varphi}{\partial t} + \mathrm{div}_{xy}\left(\mathbf{j}_{tot}^{cond} - \frac{\partial\left(\epsilon\nabla\varphi\right)}{\partial t}\right) = j_{tot}^{tm} + \frac{\partial}{\partial t}\left(C_M V_{cell} + C_S V_G\right) \tag{2.42a}$$

$$\mathbf{j}_{tot}^{cond} = -q \sum |z_i| \mu_i c_i \delta_J \nabla \varphi, \tag{2.42b}$$

where the unknowns are the potential φ and the concentrations c_i.

This is a simplified version of the reduced model mathematically derived in Section 2.3.1, because here we are working under the simplifying assumption that the potential and the concentration values in the middle of the cleft are the same as their values on Σ_{top} and Σ_{bot}. In order to close formulation (2.42), we adopt the approach proposed by Brittinger and Fromherz in [5], which basically amounts to neglecting the spatial variations of the ion concentrations.

The authors first introduce a simple electrical model for the cell-chip junction: the concentrations should be here considered constant both in space and time, not accounting for the electrodiffusive part of the phenomenon. They propose the following one compartment model of the core-coat conductor

$$(C_M + C_S) \frac{d V_J}{d t} + g_J \left(V_J - V_{cell} \right) = g_{JM}^K \left(V_{cell} - V_J - V_{M0}^K \right). \tag{2.43}$$

The electrical state of the system is described by different electrical potentials: V_J for the electrolyte junction, V_{cell} for the cell interior, V_G for the substrate and V_{bath} for the electrolyte bath. A global ohmic conductance g_J is introduced to model the coupling between the junction and the bath and the Nernst potential V_{M0}^K drops across the attached membrane. Fig. 2.3.5-(a) shows the equivalent electrical representation of this model. The dynamics of the system is then determined by an electrical time constant $\tau_J = (C_M + C_S)/g_J$, because instantaneous opening and closing of the channels is assumed: this basic representation is able to reproduce the component of the transistor record that matches the membrane current, but it cannot account for the slow component.

The above described electrical model is very simple and not accurate, because a flow of ions may lead to changes of concentration in the cell-chip junction. Therefore, Brittinger and Fromherz propose an electrodiffusion model [5], whose dynamics is determined by two-dimensional electrodiffusion. This characterization is made possible with the introduction of the ion conductances g_J^i and of the Nernst potentials V_{J0}^i, as shown in the equivalent circuit in Fig. 2.3.5-(b). Now the Nernst potential across the membrane is V_{JM0}^i with $V_{M0}^i = V_{J0}^i + V_{JM0}^i$.

Electrodiffusion is described with the variation in time of each ion concentration (again lumped parameters) in the cell-chip junction. The following nonlinear system

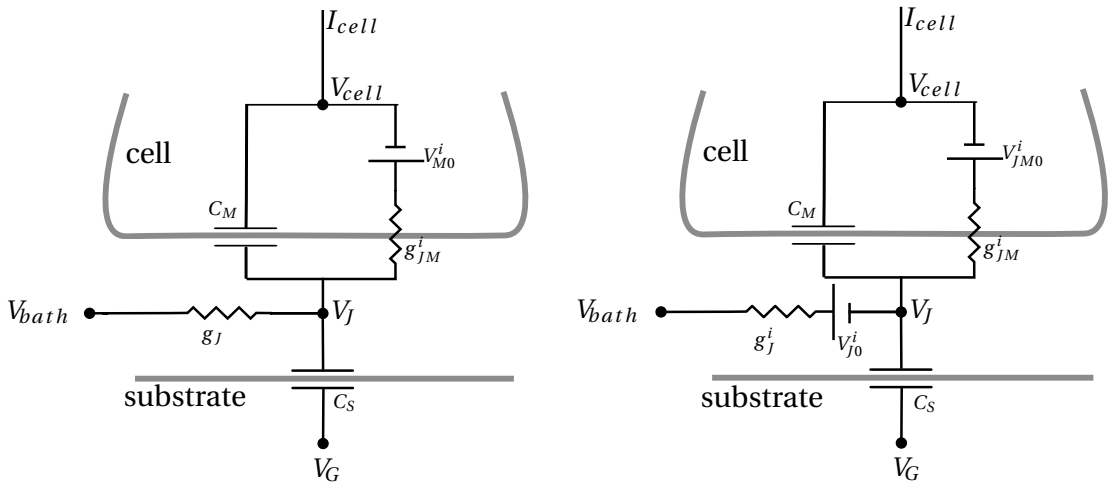

(a) Electrical model (b) Electrodiffusion model

Figure 2.3.5 – Equivalent circuits for lumped models [5]. Left: electrical model, with a global ohmic conduction g_J from junction to bath. Right: electrodiffusion model, where the variation in time of the concentrations gives a further Nernst potential V^i_{J0} and ion conductances g^i_J (for all ions i in parallel) from junction to bath.

characterizes the concentration dynamics [5]:

$$qA_J\delta_J\frac{dc_K}{dt}+g^K_J\left(V_J-V_{bath}-V^K_{J0}\right)=g^K_{JM}\left[\left(V_{cell}-V_J\right)-\left(V^K_{M0}-V^K_{J0}\right)\right] \tag{2.44a}$$

$$qz_iA_J\delta_j\frac{dc_i}{dt}+g^i_J\left(V_J-V_{bath}-V^i_{J0}\right)=0 \qquad \text{for } i\neq K. \tag{2.44b}$$

The total driving force along the junction is given by the voltage $V_J - V_E$ and by the Nernst potentials V^i_{J0} between junction and bath, defined as

$$V^i_{J0}=-\frac{V_{th}}{z_i}\ln\frac{c_i}{c_i^{bath}},$$

while the ion flow along the junction is described by the conductances defined as

$$g^i_J=5.78\pi\delta_J\frac{z_i^2q}{V_{th}}D_ic_i, \tag{2.45}$$

where D_i are the ion diffusivities. The concentration changes in the junction determine the net electrical charge that gives rise to the electrical potential V_J and, as discussed in Section 4.3.2, the time constant is now quite larger than the one of the electrical model.

Brittinger and Fromherz's model is a zero-dimensional representation of the bioelectrical system and uses a lumped parameter approach. Yet in our two dimensional

description we have a cleft potential $\varphi(x,y)$, so that we can compare our model (2.43) with their results using the integral mean of the potential in the cell-chip adhesion area Ω (see Fig. 2.3.4), by setting

$$V_J := \frac{\int_\Omega \varphi(x,y)\,dxdy}{|\Omega|}.$$

Therefore, we solve the two dimensional equation (2.39) computing the spatial distribution of the cleft potential φ and we use its integral mean in the lumped equations (2.44a)-(2.44b) for the concentrations, finding their time variation. The area-contact system to be solved in Ω reads:

$$(C_M + C_S)\frac{\partial \varphi}{\partial t} + \mathrm{div}_{xy}\mathbf{J}_{tot} = j_{tm} + \frac{\partial}{\partial t}(C_M V_{cell} + C_S V_G) \tag{2.46a}$$

$$V_J = \frac{\int_\Omega \varphi(x,y)\,dxdy}{|\Omega|} \tag{2.46b}$$

$$qA_J\delta_J\frac{dc_K}{dt} + g_J^K\left(V_J - V_{bath} - V_{J0}^K\right) = g_{JM}^K\left[\left(V_{cell} - V_J\right) - \left(V_{M0}^K - V_{J0}^K\right)\right] \tag{2.46c}$$

$$qz_iA_J\delta_j\frac{dc_i}{dt} + g_J^i\left(V_J - V_{bath} - V_{J0}^i\right) = 0 \qquad \text{for } i \neq K \tag{2.46d}$$

with the usual boundary conditions $\varphi = V_{bath}$ on $\partial\Omega$ and with the following initial conditions:

$$\varphi(0,x,y) = V_{bath} \tag{2.46e}$$

$$c_i(0) = c_i^{bath}. \tag{2.46f}$$

Chapter 3

Numerical Methods

In this chapter we illustrate the main numerical techniques adopted to solve the mathematical models introduced in Chapter 2.

We start presenting the temporal discretization, which is based on the Backward-Euler scheme and then we describe the fixed point iteration used to handle the intrinsic nonlinearity of all our models, namely the Gummel Map. The map is implemented in several different variants, adapting the algorithm to the specific considered problem.

The obtained linear differential problems are numerically solved using the Edge Averaged Finite Element method (EAFE) [1, 8, 15, 56]. This method is an exponentially fitted discretization scheme that satisfies a Discrete Maximum Principle (DMP) under mild conditions on the triangulation. A full characterization of the investigated phenomena would require three dimensional simulations, but to avoid the computational burden caused by a three dimensional spatial discretization, we take advantage of the intrinsic axial symmetry of most of our problems, which allows us to solve them in a two dimensional domain, namely a cross section in the r-z plane. Therefore, we adapt the EAFE method to this particular configuration, using radial and cylindrical coordinates and we give a detailed description of this finite element discretization in Section 3.3.

3.1 Time discretization

Most of the models described in Chapter 2 are based on systems of parabolic equations of the form:

$$\begin{cases} \dfrac{\partial u}{\partial t} + Lu = f(t) \quad t \in (0,T) \\ u|_{t=0} = u_0 \end{cases}$$

where L is an elliptic second order differential operator (for a complete treatise of this problems see [42]). For each model numerically solved, time dependence is managed with the introduction of a simple temporal semi-discretization, applying the so-called θ-method to approximate all time derivatives ($\theta \in (0,1)$ is a parameter)

$$\frac{u^{n+1}-u^n}{\Delta t} + \theta L\left(t^{n+1}, u^{n+1}\right) + (1-\theta) L(t^n, u^n) = \theta f\left(t^{n+1}\right) + (1-\theta) f(t^n). \quad (3.1)$$

In all computations, we use the Backward-Euler (BE) method, choosing $\theta = 1$. It is well known that the BE method is unconditionally stable, is easy to implement and introduces a time discretization error of order $\triangle t$.

We choose to have a time-span of $[0, T_{end}]$, T_{end} being the final time, but the time stepping Δt in (3.1) is not uniform over this span. Since in most of our applications the input signals (usually the intracellular potential $V_{cell}(t)$) are a combination of Heaviside functions, the time stepping is a-priori appropriately chosen. At each time level, a nonlinear system of equations must be solved and we have seen in our numerical experiments that the linearization methods may suffer from convergence problems when we do not use a refining procedure after discontinuities. Therefore, in correspondence of the switch time on/off of the signal, the value of Δt is set to an appropriately small value, in order to track the fast rise time of the solution. After this initial transient part, a such refined time stepping is not mandatory anymore, so that we can use a larger value of Δt, reducing the computational effort. We have then M_T non uniform intervals, in such a way that $t_m = \sum_m \triangle t_m$ is the m-th time level, where $m = 0, 1, ..., M_T - 1$ and $\triangle t_m$ is the a-priori chosen discretization step.

In all our simulations, the time stepping used is of the order of 1×10^{-8} s in the neighborhood of signal switching on and of the order of 1×10^{-4} s when the transients are exhausted.

3.2 Linearization methods

The partial differential models introduced in Chapter 2 are nonlinear. In order to treat this difficulty, we apply a functional iteration procedure widely used in the decoupled solution of the Drift-Diffusion semiconductor device equations. This is the well known Gummel Map [25, 27, 17, 2], a staggered algorithm where each variable of the problem and its corresponding equation are treated in sequence until convergence.

The nonlinearity of the considered models is related to the coupling between the potential φ and the ion concentrations c_i, due to the drift term $z_i\mu_i c_i\mathbf{E} = -z_i\mu_i c_i\nabla\varphi$ in the ionic flux constitutive equation (2.4b), and due to the nonlinear nature of the equations describing the ionic membrane currents for both the resistive (2.10) and the GHK model (2.11). Functional iterations provide an approach to translate the nonlinear system into a sequence of linear problems, the solution of which should converge to a corresponding, but non necessarily unique, solution of the original problem. The most relevant example of functional iteration is the Newton method.

While this method has the property of being quadratically convergent, some essential drawbacks must be pointed out: first, a "good" initial guess must be provided to reach the correct solution (the method could stop in a local minimizer or not even converge); second, the algebraic system associated with the discretization of the linearized problem may be very large in size, because it has to be solved for all variables simultaneously. This large size strongly increases the amount of computational time and often results in an ill-conditioned Jacobian matrix.

These are the main reasons why we have decided to use a staggered algorithm as the main basic approach of the present work. The equations defining the potential and each ion concentration are solved separately, instead of using a monolithic algorithm. This is the so called Gummel Map approach and it simplifies the problem because of the following properties:

- the decoupling of the potential from the concentration variables renders the continuity equations linear, hence easily solvable;

- the size of the corresponding algebraic system is reduced, decreasing the global time required to reach a solution, as well as improving the numerical conditioning of the coefficient matrix.

3.2.1 Linearization of the electrodiffusion model

The first case we analyze is the simplified model presented in Section 2.3.2, where a two dimensional equation for the potential $\varphi\left(t,x,y\right)$ and then the lumped equations for each ion concentration $c_i(t)$ need to be solved.

Regarding the first equation, the nonlinearity is caused by the Nernst potentials in the transmembrane current but also by $\mathbf{j}_{tot}^{cond} = -\sigma_{el}\nabla\varphi$, because the cleft conductance depends on the unknown concentrations. In the system of ODEs for each ion concentration, (2.44a) and (2.44b) are decoupled from one another but again nonlinear because of the Nernst potential and the cleft conductances (defined in (2.45)) depending on the concentrations.

We apply a simple staggered algorithm to this model: at each time step the considered problem needs an iterative procedure to reach the current solution. We use the temporal discretization with the BE method introduced in Section 3.1 for the specific area contact equation (2.46a), ending up with the following semi-discretized equation

$$\begin{aligned}
&\frac{1}{\delta_j}\left(C_M + C_S\right)\frac{\varphi^{n+1}}{\Delta t} + \operatorname{div}\left(\frac{\sigma_{tot}^{n+1}}{\epsilon}D^{n+1} + \frac{D^{n+1}}{\Delta t}\right) \\
&= \frac{1}{\delta_j}\left(C_M\frac{V_{cell}^{n+1} - V_{cell}^{n}}{\Delta t} + C_S\frac{V_G^{n+1} - V_G^{n}}{\Delta t}\right) + \frac{1}{\delta_j}\left(C_M + C_S\right)\frac{\varphi^{n}}{\Delta t} + \operatorname{div}\left(\frac{D^{n}}{\Delta t}\right) + \frac{j_{tm}^{n+1}}{\delta_j},
\end{aligned}$$

where σ_{tot}^{n+1} is a function of the unknown concentrations c_i^{n+1}. Regarding the ODE system proposed in [5], we come to this discretization

$$\begin{aligned}
&qA_J\delta_J\frac{dc_i^{n+1}}{\Delta t} + g_{Ji}^{n+1}\left(V_J^{n+1} - V_{bath} - V_{J0i}^{n+1}\right) \\
&= qA_J\delta_J\frac{dc_i^{n}}{\Delta t} + g_{JM}^{K}\left[\left(V_{cell}^{n+1} - V_J^{n+1}\right) - \left(V_{M0i}^{n+1} - V_{J0i}^{n+1}\right)\right].
\end{aligned}$$

Each step of the algorithm, as shown by the diagram of Fig. 3.2.1, requires the following two solution blocks:

- computing the updated potential $\varphi^{(k+1)}$ as solution of the linear area contact equation, where, as initial guesses, we use the concentrations $c_i^{(k)}$ at the previous step in the conductivity $\sigma_{tot}^{(k)}$ and in the transmembrane currents

$$j_{tm}^{(k+1)} = g_{JM}^{i}\left(\left(\varphi^{(k+1)} - V_{cell}^{n+1}\right) - \frac{V_{th}}{z_i}\ln\left(\frac{c_i^{cell}}{c_i^{(k)}}\right)\right);$$

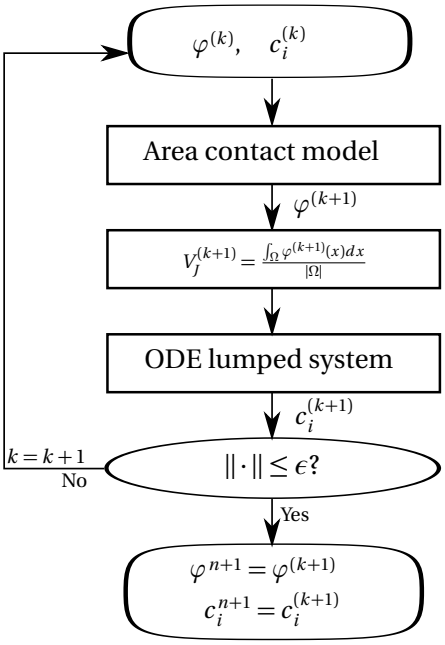

Figure 3.2.1 – Solution map for the electrodiffusion model.

- solving the M nonlinear ordinary differential equations to update the concentrations $c_i^{(k+1)}$; with the potential $\varphi^{(k+1)}$ one is now able to compute its integral mean $V_J^{(k+1)}$ and use it in the ODE system. The system is still nonlinear, due to the Nernst potentials V_{M0} and V_{J0} and the conductance g_J^i defined in (2.45).

Different methods can be used to treat the nonlinearity in this second computational block. We compare three different approaches:

1. Nernst potentials and cleft conductaces are evaluated at the previous Gummel step. The corresponding system is then linear;

2. the concentrations are taken at the previous Gummel step in the Nernst potentials, but the conductances are considered unknown (at the current Gummel step). Again the system is reduced to a linear one;

3. lastly, a nonlinear system can be solved, using the unknown concentrations $c_i^{(k+1)}$ at the current Gummel step in all the equations. To handle this nonlinearity, we introduce a further sub-iteration (tipically a Newton method).

The Gummel cycle needs a stopping criterion, as one can see in Fig. 3.2.1. The convergence check of each iteration is carried out by verifying whether the maximum absolute difference between two consecutive iterates $^{(k)}$ and $^{(k+1)}$ is less than a prescribed tolerance ϵ. For the potential and for the M concentrations the convergence

check is:

$$\|\varphi^{(k+1)} - \varphi^{(k)}\|_{L^\infty(\Omega)} < \epsilon_\varphi \qquad \|c_i^{(k+1)} - c_i^{(k)}\|_{L^\infty(\Omega)} < \epsilon_c, \tag{3.2}$$

where, for any measurable function f, we set

$$\|f\|_{L^\infty(\Omega)} = \inf\left\{M \geq 0 : |f(x)| \leq M \text{ almost everywhere in } \Omega\right\}.$$

3.2.2 Linearization of the PNP system

As pointed out in Section 2.2.2, the PNP system is formally identical to the drift-diffusion (DD) model for semiconductor devices. One can thus profitably apply a change of variable, known as Cole-Hopf transformation [22] in such a way that expression (2.4b) for the fluxes can be rewritten as

$$\mathbf{f}_i = -\left(D_i \nabla c_i + z_i c_i \mu_i \nabla \varphi\right) = -z_i D_i c_i \left(\frac{\nabla c_i}{z_i c_i} + \frac{\nabla \varphi}{V_{th}}\right), \tag{3.3}$$

where we have used the Einstein relation (2.4e). Then, with the introduction of a suitable reference concentration c_{ref} (for example $c_{ref} = \max_i \left\{c_i^{bath}, c_i^{cell}\right\}$), we are able to define the electro-chemical potential associated with the i-th ionic species as

$$\varphi_{c_i} := \varphi + \frac{V_{th}}{z_i} \ln \frac{c_i}{c_{ref}}, \tag{3.4}$$

and then the ion concentrations can be computed in the following way

$$c_i = c_{ref} \exp\left(\frac{z_i(\varphi_{ci} - \varphi)}{V_{th}}\right). \tag{3.5}$$

Resubstituting (3.4) into expression (3.3), we end up with the following gradient form for the ion flux constitutive equation

$$\mathbf{f}_i = -z_i D_i c_i \frac{\nabla \varphi_{c_i}}{V_{th}}.$$

This deep similarity between the PNP and the DD model, is a valid motivation for the choice of the Gummel map in the iterative solution of the PNP system. As shown in the flow chart in Fig. 3.2.2, at each time level t_m, the iterative procedure starts with initial guesses for the electric and electro-chemical potentials, $\varphi^{(0)}$ and $\varphi_{c_i}^{(0)}$ (or equivalently, with a concentration guess $c_i^{(0)}$). Each single k-th iteration of the Gummel process consists of:

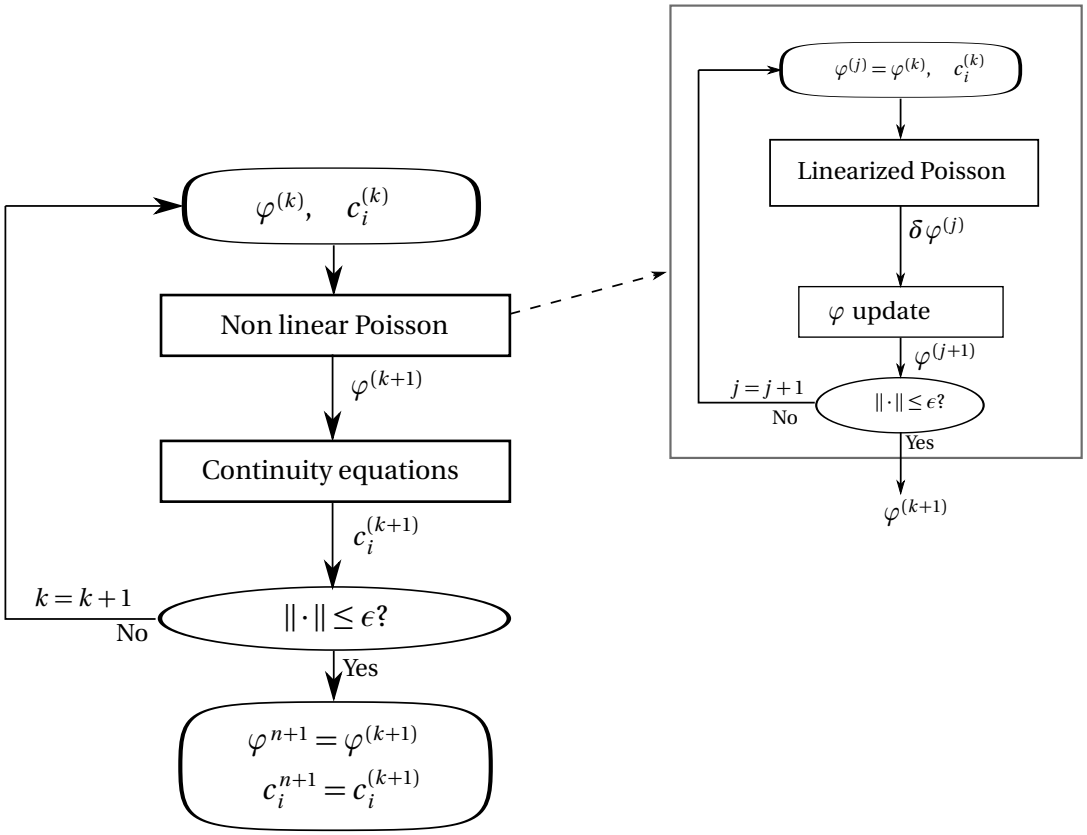

Figure 3.2.2 – Solution map for the PNP system: Gummel map and Newton subcycle for the non linear Poisson problem.

- the solution of a non linear Poisson equation to obtain an updated potential $\varphi^{(k+1)}$. In detail, with the use of (3.5), one can rewrite (2.4c) as

$$\operatorname{div}\left(-\epsilon\nabla\varphi\right) = q\sum_{i=1}^{M} z_i c_{ref} \exp\left(\frac{z_i(\varphi_{ci}-\varphi)}{V_{th}}\right)$$

  and an iterative Newton method [50] can be applied to find a solution. We need then to introduce another sub-cycle using the index j to indicate the subiterations. With this procedure we are able to find the solution for the Newton update $\delta\varphi^{(j)} = \varphi^{(j+1)} - \varphi^{(j)}$ of the following linearized problem

$$F'\left(\varphi^{(j)}\right)\delta\varphi^{(j)} = -F\left(\varphi^{(j)}\right),$$

  where

$$F\left(\varphi\right) = \operatorname{div}\left(-\epsilon\nabla\varphi\right) - q\sum_{i=1}^{M} z_i c_{ref} \exp\left(\frac{z_i(\varphi_{ci}-\varphi)}{V_{th}}\right)$$

and where $F'(\varphi)$ is the Fréchet derivative of F, evaluated at $\varphi^{(j)}$ and acting in a linear manner on the increment function $\delta\varphi^{(j)}$;

- the solution of a linear continuity equation for each ion species $c_i^{(k+1)}$, $i = 1,...,M$, given the known updated potential $\varphi^{(k+1)}$. We treat the nonlinear transmembrane currents using the concentrations $c_i^{(k)}$ at the previous step, thus obtaining a linear system to solve;

- the check of convergence (3.2) of the current iteration, already illustrated in Section 3.2.1.

A complete analysis of the convergence of the Gummel map is carried out in [25] in the case $M = 2$ for the drift diffusion model: the main result is that as $k \to \infty$, the map converges to a unique solution φ and c_i, $i = 1,2$, provided that suitable constraints are enforced on boundary data and problem coefficients. With minor modifications we expect this result to be extendable also to the case of the PNP model examined in this thesis.

3.3 Finite element approximation in axisymmetric geometries

Once the linearization is applied, one needs to numerically approximate the resulting linear system of PDEs with a Galerkin-Finite Element Method (G-FEM). Standard G-FEM are in general not suitable for problems where drift terms are dominant. Since this latter situation is what typically occurs in the study of ion-electronic interfaces, in the present work we have decided to use the Edge Averaged Finite Element method (EAFE). This is a multidimensional extension of the Scharfetter-Gummel one dimensional difference scheme, which provides an exponential fitting finite element discretization [1, 8, 15, 28, 56]. The advantage of the EAFE method is that if a maximum principle holds for the problem on the continuous level, then the discrete counterpart holds too, giving rise to a "monotone scheme". A well-known sufficient condition for a scheme to be monotone is that the corresponding stiffness matrix is an M-matrix and it can be shown that the stiffness matrix obtained with the EAFE method is an M-matrix under the sole assumption that the triangulation of the domain is of Delaunay type [56]. This result is very important, since applying the EAFE method to the continuity equations in the PNP system ensures that the computed concentrations are strictly positive.

As already anticipated, most of the geometrical models studied in the present work require the introduction of cylindrical coordinates in axial symmetry. Therefore, we extend the EAFE method, originally proposed in the case of cartesian orthogonal coordinates, to treat this particular configuration, building the two dimensional numerical discretization with the use of cylindrical coordinates.

3.3.1 Model problem in an axisymmetric configuration

For the sake of clarity, we introduce a model continuity problem for a function u, on a domain $\Omega \subset \mathbb{R}^3$ with a Lipschitz boundary $\partial\Omega = \Gamma_D \cup \Gamma_N$ such that $\Gamma_D \cap \Gamma_N = \emptyset$, as follows:

$$\begin{cases} -\mathrm{div}\mathbf{J}(u) + cu = f & \text{in } \Omega \\ \mathbf{J}(u) = \mu(\nabla u - \mathbf{b}u) & \text{in } \Omega \\ u = 0 & \text{on } \Gamma_D \\ -\mathbf{J}(u)\cdot\mathbf{n} = j_N & \text{on } \Gamma_N. \end{cases} \tag{3.6}$$

Here $\mu \in C^0(\overline{\Omega})$ is a strictly positive real function such that $\mu = \mu(x) \geq \mu_0 > 0 \ \forall x \in \overline{\Omega}$. The drift field can be written as $\mathbf{b} := \nabla\psi$, ψ being a continuous piecewise linear function over $\overline{\Omega}$, the reaction coefficient $c \in L^\infty(\Omega)$, $c \geq 0$ a.e. in Ω and $f \in L^2(\Omega)$. Regarding the boundary conditions, only for ease of presentation we are considering homogeneous Dirichlet boundary conditions on Γ_D, while on Γ_N Neumann conditions are applied, having $j_N \in L^2(\Gamma_N)$ as a given datum.

Under these assumptions, we can reformulate the flux expression in a way that will be useful when studying the spatial discretization of the flux. Introducing the following change of variable

$$u := ne^{\psi} \tag{3.7}$$

and replacing (3.7) into the definition of the flux, yields

$$\mathbf{J}(n) = \mu e^{\psi}\nabla n. \tag{3.8}$$

Thanks to this change of variables, problem (3.6) reads as follows:

$$\begin{cases} -\mathrm{div}\mathbf{J}(n)+ce^{\psi}n=f & \text{in }\Omega \\ \mathbf{J}(n)=\mu e^{\psi}\nabla n & \text{in }\Omega \\ n=0 & \text{on }\Gamma_D \\ -\mathbf{J}(n)\cdot\mathbf{n}=j_N & \text{on }\Gamma_N. \end{cases} \tag{3.9}$$

For our geometrical purpose, one can then rewrite problem (3.9) with the use of cylindrical coordinates (r,ϕ,z) and obtain the boundary value problem:

$$\begin{cases} \dfrac{1}{r}\dfrac{\partial}{\partial r}(rJ_r)+\dfrac{1}{r}\dfrac{\partial}{\partial\phi}J_\phi+\dfrac{\partial}{\partial z}J_z+ce^{\psi}n=f & \text{in }\Omega \\ n=0 & \text{on }\Gamma_D \\ -\mathbf{J}(n)\cdot\mathbf{n}=j_N & \text{on }\Gamma_N, \end{cases} \tag{3.10}$$

where the operator $\mathbf{J}=\mathbf{J}(n)$ is defined as

$$\mathbf{J}=\begin{bmatrix} J_r \\ J_\phi \\ J_z \end{bmatrix}=\begin{bmatrix} \mu e^{\psi}\dfrac{\partial n}{\partial r} \\ \mu\dfrac{1}{r}e^{\psi}\dfrac{\partial n}{\partial\phi} \\ \mu e^{\psi}\dfrac{\partial n}{\partial z} \end{bmatrix}, \tag{3.11}$$

and the outward unit normal vector in cylindrical coordinates is $\mathbf{n}=\left[n_r,n_\phi,n_z\right]$.

At this point, we choose to study problem (3.10) in an axisymmetric configuration, for example the domain Ω_{as} schematically depicted in Fig. 3.3.1. This two dimensional domain, if rotated around its symmetry axis, becomes a three dimensional rotational solid. Therefore we can say that performing two dimensional computations, we are actually able to reconstruct three dimensional distributions of the considered quantities. This configuration is independent of the ϕ-coordinate and then we can take $\frac{\partial}{\partial\phi}=0$, ending up with the following model problem on Ω_{as}:

$$\begin{cases} \dfrac{1}{r}\dfrac{\partial}{\partial r}(rJ_r)+\dfrac{\partial}{\partial z}J_z+ce^{\psi}n=f & \text{in }\Omega_{as} \\ n=0 & \text{on }\Gamma_D \\ -\mathbf{J}(n)\cdot\mathbf{n}=j_N & \text{on }\Gamma_N, \end{cases} \tag{3.12}$$

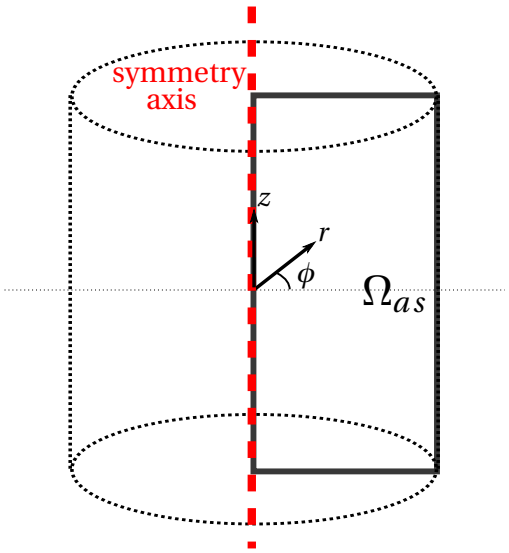

Figure 3.3.1 – Schematics of an axisymmetric configuration: the dependence on the ϕ-coordinate can be neglected and the problem can be solved only in the Ω_{as} part, obtaining a three dimensional domain with the rotation of Ω_{as} around the symmetry axis.

where now we have

$$\mathbf{J} = \begin{bmatrix} J_r \\ J_z \end{bmatrix}, \qquad \mathbf{n} = \begin{bmatrix} n_r \\ n_z \end{bmatrix}$$

and where, for ease of notation, the boundaries $\Gamma_N \cap \partial\Omega_{as}$ and $\Gamma_D \cap \partial\Omega_{as}$ of the new domain are simply denoted Γ_N and Γ_D, respectively.

To solve system (3.12), we need to introduce a spatial discretization on the domain Ω_{as}. Dealing with radial and cylindrical coordinates is a little different from the usual cartesian case, because the operators assume a different form. Besides, when writing the weak formulation, the integration procedure leads to the introduction of a new scalar product. The cylindrical test volume of integration is $d\omega = r\,dr\,d\phi\,dz$, which can be reduced to $d\omega = r\,dr\,dz$ thanks to axial symmetry, having $\int_0^{2\pi} d\phi = 2\pi$. Therefore, for a given open set $\Omega \subseteq \mathbb{R}^2$ we can define on $L^2(\Omega)$ a new scalar product $\langle \cdot, \cdot \rangle_\omega$ as

$$\begin{aligned} \langle f, g \rangle_\omega &:= \int_\Omega f(\omega) g(\omega) d\omega \\ &= \int_0^Z \int_0^R f(r,z) g(r,z) r\,dr\,dz \\ &= \int_0^Z \int_0^R \widetilde{f}(r,z) \widetilde{g}(r,z) dr\,dz = \left\langle \widetilde{f}, \widetilde{g} \right\rangle, \end{aligned} \tag{3.13}$$

where $\widetilde{f} := \sqrt{r} f$ and $\widetilde{g} := \sqrt{r} g$. Expression (3.13) shows that $\langle \cdot, \cdot \rangle_\omega$ inherits all the

properties of the usual scalar product (for a detailed treatise of this issue see [40]). With the use of an analogous argument, one can introduce a "cylindrical measure" ω starting from the Lebesgue measure λ [40], to actually measure manifolds using cylindrical coordinates and also to build the L^p spaces. In this way, all the usual properties are inherited and the usual results valid in the standard cartesian orthogonal case easily follow. For example, the new norm in $L^2(\Omega)$ is defined on the scalar product (3.13) as

$$\|w\|_{\omega,L^2(\Omega)} = \langle w, w\rangle_\omega^{1/2} \quad \forall w \in L^2(\Omega). \tag{3.14}$$

Proceeding with the derivation of the weak formulation of problem (3.12), we can now integrate it against a test function $v = v(r,z)$ and obtain

$$\int_0^Z \int_0^R \frac{1}{r}\frac{\partial}{\partial r}(rJ_r)vrdrdz + \int_0^Z \int_0^R \frac{\partial}{\partial z}J_z vrdrdz + \int_0^Z \int_0^R ce^{\psi}nvrdrdz = \int_0^Z \int_0^R fvrdrdz.$$

The $1/r$ term in the first integral can be simplified with the integrating r, and using as usual the Gauss theorem we end up with

$$-\int_{\Omega_{as}} J_r\frac{\partial v}{\partial r}d\omega + \int_{\partial\Omega_{as}} J_r v n_r ds_\omega - \int_{\Omega_{as}} J_z\frac{\partial v}{\partial z}d\omega + \int_{\partial\Omega_{as}} J_z v n_z ds_\omega + \int_{\Omega_{as}} ce^{\psi}nvd\omega = \int_{\Omega_{as}} fvd\omega.$$

Here we have introduced the curvilinear abscissa in radial coordinates $ds_\omega = rds$, where ds is the usual curvilinear abscissa. At the end of this procedure we can regroup the terms and come to the usual weak formulation:

find $n \in V$ such that:

$$\begin{aligned}
a_\omega(n,v) &= F_\omega(v) \qquad \forall v \in V && \text{(3.15a)}\\
a_\omega(n,v) &= -\left\langle \mu e^{\psi}\nabla n, \nabla v\right\rangle_\omega + \left\langle ce^{\psi}n, v\right\rangle_\omega && \text{(3.15b)}\\
&= -\int_{\Omega_{as}} \mathbf{J}\cdot\nabla v d\omega + \int_{\Omega_{as}} ce^{\psi}nvd\omega\\
F_\omega(v) &= \langle f, v\rangle_\omega + \int_{\Gamma_N} j_N v ds_\omega && \text{(3.15c)}\\
&= \int_{\Omega_{as}} fvd\omega + \int_{\Gamma_N} j_N v ds_\omega,
\end{aligned}$$

where the vector $\mathbf{J}$ is defined in (3.11). The functional space is defined on the new

measure space in the usual way

$$V := H^1_{\Gamma_D}(\Omega_{as}) = \left\{ v \in H^1(\Omega_{as}) : \ v|_{\Gamma_D} = 0 \right\}, \tag{3.15d}$$

with the norm defined as follows, thanks to the Poincaré inequality [42][1]

$$\|w\|_V := \|\nabla w\|_{\omega, L^2(\Omega_{as})}. \tag{3.16}$$

The following theorem can be proved, as in the usual case of cartesian orthogonal coordinates.

Theorem. *The bilinear form (3.15b) is continuous and coercive on V and the functional (3.15c) is continuous on V. Therefore the application of the Lax-Milgram Lemma ensures that problem (3.15) has a unique solution and that the following a-priori estimate holds*

$$\|n\|_V \leq \frac{C_{\Omega_{as}} \left\| f \right\|_{L^2(\Omega_{as})} + C_T \left\| j_N \right\|_{L^2(\Gamma_N)}}{e^{\psi_m} \mu_o}.$$

This automatically implies that (3.12) admits a unique weak solution $u \in V$.

Proof. Thanks to the hypotheses introduced for problem (3.6), we define the maximum and the minimum values of the functions ψ and μ over $\overline{\Omega}$ in the following way:

$$\psi_M := \max_{\mathbf{x} \in \overline{\Omega}} \psi(\mathbf{x}) \qquad \psi_m := \min_{\mathbf{x} \in \overline{\Omega}} \psi(\mathbf{x})$$
$$\mu_M := \max_{\mathbf{x} \in \overline{\Omega}} \mu(\mathbf{x}).$$

Using the norms defined in (3.14) and (3.16) and omitting the subscript $\|\cdot\|_\omega$ for ease of notation, we start proving that the bilinear form $a_\omega(\cdot,\cdot)$ is continuous on V. Thanks to the Hölder and Cauchy-Schwarz inequalities, the first integral in (3.15b) can be upper bounded as follows

$$\left| \int_{\Omega_{as}} \mu e^{\psi} \nabla n \cdot \nabla v \, d\omega \right| \leq \mu_M e^{\psi_M} \|\nabla n\|_{L^2(\Omega_{as})} \|\nabla v\|_{L^2(\Omega_{as})} = \mu_M e^{\psi_M} \|n\|_V \|v\|_V.$$

Using the Poincaré inequality on the second term, we obtain

$$\left| \int_{\Omega_{as}} c e^{\psi} n v \, d\omega \right| \leq e^{\psi_M} \|c\|_{L^\infty(\Omega_{as})} C^2_{\Omega_{as}} \|n\|_V \|v\|_V.$$

[1] The Poincaré inequality $\|w\|_{L^2(\Omega_{as})} \leq C_{\Omega_{as}} \|w\|_{H^1_{\Gamma_D}(\Omega_{as})} = C_{\Omega_{as}} \|\nabla w\|_{L^2(\Omega_{as})}$ holds in this case because we are considering $w \in H^1_{\Gamma_D}(\Omega_{as})$, having homogeneous boundary conditions on Γ_D.

We have then proved the continuity of $a_\omega(\cdot,\cdot)$ on V, namely that there exists a constant $M>0$ such that

$$|a_\omega(n,v)| \leq M\|n\|_V\|v\|_V \ \forall n,v\in V, \qquad M = e^{\psi_M}\left(\mu_M + C^2_{\Omega_{as}}\|c\|_{L^\infty(\Omega_{as})}\right).$$

The coercivity can be easily proved by considering only the first term of (3.15a), thanks to the hypothesis on the reaction term that $c\geq 0$ a.e. in Ω. Using the the definition of the norm on V, we obtain

$$a_\omega(v,v) \geq \mu_0 e^{\psi_m}\|\nabla v\|^2_{L^2(\Omega_{as})} = \mu_0 e^{\psi_m}\|v\|^2_V.$$

The bilinear form is therefore coercive with a coercivity constant α, as follows

$$a_\omega(v,v) \geq \alpha\|v\|^2_V \ \forall v\in V, \qquad \alpha = \mu_0 e^{\psi_m}.$$

Lastly, we need to prove the continuity of the functional (3.15c). Using again the Poincaré inequality, we can find an upper bound for the first term as

$$\left|\int_{\Omega_{as}} f v\, d\omega\right| \leq \left\|f\right\|_{L^2(\Omega_{as})}\|v\|_{L^2(\Omega_{as})} \leq C_{\Omega_{as}}\left\|f\right\|_{L^2(\Omega_{as})}\|v\|_V.$$

On the boundary integral, after the Cauchy-Schwarz inequality, we apply a trace inequality[2] in the following way

$$\left|\int_{\Gamma_N} j_N v\, ds_\omega\right| \leq \left\|j_N\right\|_{L^2(\Gamma_N)}\|v\|_{L^2(\Gamma_N)} \leq C_T\left\|j_N\right\|_{L^2(\Gamma_N)}\|v\|_V.$$

The linear functional is then continuous, with a continuity constant $\Lambda>0$ such that

$$|F_\omega(v)| \leq \Lambda\|v\|_V \ \forall v\in V, \qquad \Lambda = C_{\Omega_{as}}\left\|f\right\|_{L^2(\Omega_{as})} + C_T\left\|j_N\right\|_{L^2(\Gamma_N)}.$$

Therefore, the assumptions of the Lax-Milgram lemma are verified for problem (3.15), and the following a-priori estimate holds

$$\|n\|_V \leq \frac{\Lambda}{\alpha} = \frac{C_{\Omega_{as}}\left\|f\right\|_{L^2(\Omega_{as})} + C_T\left\|j_N\right\|_{L^2(\Gamma_N)}}{e^{\psi_m}\mu_0}.$$

□

[2]For a function $w\in L^p(\Gamma)$, with $\Gamma\subseteq\partial\Omega$, the trace inequality states $\left\|w|_\Gamma\right\|_{L^p(\Gamma)} \leq C_T\|w\|_{H^1(\Omega)}$.

3.3.2 Spatial discretization

We are now able to apply the EAFE method [8, 6] to the model problem in cylindrical coordinates introduced in Section 3.3.1. In order to do that, we use piecewise linear finite elements on a regular triangulation T_h of the domain Ω_{as} such that

$$\overline{\Omega}_{as} = \bigcup_{K \in T_h} K$$

with the following properties:

- $\text{int}(K) \neq \emptyset$;
- $\text{int}(K_1) \cap \text{int}(K_2) = \emptyset$ for each distinct $K_1, K_2 \in T_h$;
- if $F = K_1 \cap K_2 \neq \emptyset$ (with K_1 and K_2 distinct elements of T_h) then F is a common side or vertex of $K_1$and K_2;
- $\text{diam}(K) \leq h \; \forall K \in T_h$.

For the purpose of simplifying the presentation, we assume that the triangulation covers Ω_{as} exactly. Given $K \in T_h$, we introduce in Fig. 3.3.2 a local notation for the triangles in such a way that the verteces v_i, $i = 1,2,3$ are labeled in counterclockwise order and we denote with $\mathbf{e}_i$ the edge opposite to v_i, orienting it in such a way that it connects v_{i+1} to v_{i-1}. The cylindrical coordinates of the verteces are (r_i, z_i). l_i denotes each edge length, $\mathbf{t}_i$ is the unit tangent vector oriented in the same direction as $\mathbf{e}_i$ and $\mathbf{n}_i$ is the unit outward normal vector to edge $\mathbf{e}_i$. Lastly, the segment from the midpoint of $\mathbf{e}_i$ to the intersection of the perpendicular edge bisectors is denoted

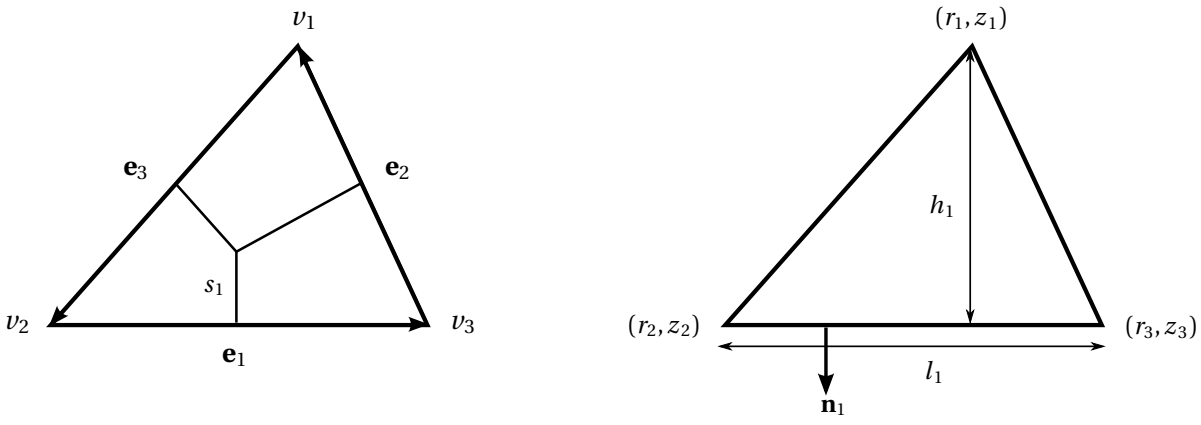

Figure 3.3.2 – Parameters associated with a generic triangle K of the triangulation.

by s_i. We will also need a difference operator along $\mathbf{e}_i$, defined, for each continuous function η, as

$$\delta_i(\eta) := \eta(v_{i-1}) - \eta(v_{i+1}). \tag{3.17}$$

Let then

$$V_h = \{v \in C^0(\overline{\Omega}_{as}) : v|_K \in \mathbb{P}^1(K),\ \forall K \in T_h\} \subset H^1_{\Gamma_D}(\Omega_{as})$$

be the piecewise linear finite element space (subspace of the functional space V defined in (3.15d)) and denote by φ_i the nodal basis function, which is equal to one at v_i and to zero at the other vertices.

The equation associated with the generic test function φ_h over a generic element K for problem (3.15a) reads as follows

$$\begin{aligned} &-\int_K \mathbf{J}(n_h)\cdot\nabla\varphi_h r\,dr\,dz + \int_K ce^{\psi} n_h \varphi_h r\,dr\,dz \\ &= \int_K f_h \varphi_h r\,dr\,dz + \int_{\partial K\cap\Gamma_N} j_N \varphi_h\, ds_\omega \end{aligned} \tag{3.18}$$

for $n_h, \varphi_h \in V_h$.

We start analyzing the first integral, namely we build an approximation $\mathbf{J}_h$ of the flux. This problem is dealt in the present work with the EAFE method, characterized by the approximation of the diffusion coefficient of the flux differential operator with an armonic average along the triangle sides $\mathbf{e}_i$. Given a function $\eta \in C^0(\overline{K})$, the harmonic average of η along the edge $\mathbf{e}_i$ is defined as

$$\widehat{\eta}_i := \left(\frac{1}{l_i}\int_{\mathbf{e}_i} \eta^{-1} ds\right)^{-1}. \tag{3.19}$$

The first term in (3.18) becomes then

$$\int_K \mathbf{J}_h^{EA}(n_h)\cdot\nabla\varphi_h r\,dr\,dz, \tag{3.20}$$

where we are introducing the discretized EAFE expression for the flux, defined with the use of relation (3.19) in the following way

$$\mathbf{J}_h^{EA}(n_h) = \sum_{j=1}^{3} J_j^{EA}(n_h)\mathbf{j}_j. \tag{3.21}$$

In this latter, $\mathbf{j}_j$ is a vector-valued shape function associated with edge $\mathbf{e}_j$ to be suitably defined, while J_j^{EA} is the associated degree of freedom for the flux. Since n_h is

a piecewise linear function, using δ_i defined in (3.17), each component of the first term in the last relation can be explicitly written as

$$J_j^{EA} = \widehat{a}_j \nabla n_h \cdot \mathbf{t}_j = \widehat{a}_j \frac{\delta_j(n_h)}{l_j}, \tag{3.22}$$

where $\widehat{a}_j$ is the harmonic average of μe^{ψ} along $\mathbf{e}_j$, in this case equal to

$$\begin{aligned} \widehat{a}_j &:= \left(\frac{1}{l_j} \int_{\mathbf{e}_j} \left(\mu e^{\psi}\right)^{-1} ds \right)^{-1} \\ &= \mu e^{\psi_{j-1}} Be(\psi_{j-1} - \psi_{j+1}), \end{aligned}$$

where $Be(\cdot)$ is the usual inverse of the Bernoulli function defined in (2.12).

The choice of piecewise linear finite elements for the approximation of n is crucial, because in this way the flux projection J_j^{EA} along each triangle edge is a constant value, that can be used to construct the numerical approximation of $\mathbf{J}$ over each triangle K. The basis function set for the flux approximation along the edge is defined as follows

$$\mathbf{j}_j = \frac{l_j s_j}{|K|} \mathbf{t}_j \qquad j = 1, 2, 3.$$

The above description therefore shows that $\mathbf{J}_h^{EA}(n_h)$ is a constant approximation of $\mathbf{J}(n)$ over the element K and a linear operator that allows to reconstruct a vector field over K starting from its tangential components along the triangle edges [1]. To numerically implement the method and to analyze its monotonicity, it is essential to write the stiffness matrix associated with the generic element K. Substituting the test function φ_h with the basis function φ_i, $i = 1,2,3$ (see Fig. 3.3.2) defined on the triangle K, we obtain

$$\begin{aligned} \int_K \mathbf{J}_h^{EA}(n_h) \cdot \nabla \varphi_i r dr dz &= \sum_{j=1}^{3} J_j^{EA}(n_h) \int_K \mathbf{j}_i \cdot \nabla \varphi_i r dr dz \\ &= J_{i-1}^{EA}(n_h) \int_K \frac{l_{i-1} s_{i-1} \mathbf{t}_{i-1}}{|K|} \cdot \nabla \varphi_i r dr dz \\ &+ J_i^{EA}(n_h) \int_K \frac{l_i s_i \mathbf{t}_i}{|K|} \cdot \nabla \varphi_i r dr dz \\ &+ J_{i+1}^{EA}(n_h) \int_K \frac{l_{i+1} s_{i+1} \mathbf{t}_{i+1}}{|K|} \cdot \nabla \varphi_i r dr dz. \end{aligned} \tag{3.23}$$

For the approximation of the integrals, we recall that the following relationships hold on an arbitrary triangle K:

$$\begin{aligned} \nabla\varphi_i &= -\frac{\mathbf{n}_i}{h_i} \\ l_i\mathbf{t}_i\cdot\nabla\varphi_i &= 0 \\ l_{i\pm1}\mathbf{t}_{i\pm1}\cdot\nabla\varphi_i &= \pm 1. \end{aligned}$$

Using these properties, (3.23) becomes

$$\begin{aligned} &\int_K \mathbf{J}_h^{EA}(n_h)\cdot\nabla\varphi_i r\,dr\,dz \\ &= \frac{J_{i+1}^{EA}(n_h)s_{i+1}}{|K|}\int_K r\,dr\,dz \;-\; \frac{J_{i-1}^{EA}(n_h)s_{i-1}}{|K|}\int_K r\,dr\,dz \qquad i=1,2,3. \end{aligned} \tag{3.24}$$

So far, the procedure is identical to that valid in the cartesian case, but here we also need to account for the presence of r and to use a quadrature rule in order to approximate the term $\int_K r\,dr\,dz$. We adopt a baricentric formula, which is exact in this case, because we are dealing with the approximation of a first-degree polynomial in cylindrical coordinates. Therefore we can exactly compute the integral in the following way

$$\int_K r\,dr\,dz = \overline{r_K}|K| = \frac{r_1+r_2+r_3}{3}|K|, \tag{3.25}$$

where we are introducing the baricenter $\overline{r_K}$ of element K in radial coordinates (r_i are the r coordinates of the verteces v_i, as shown in Fig. 3.3.2).

Combining the use of relations (3.22) and (3.25) in (3.24), the explicit form of the flux integration over K can be easily written, highlighting the contribution of each basis function:

$$\begin{aligned} \int_K \mathbf{J}_h^{EA}(n_h)\cdot\nabla\varphi_1 r\,dr\,dz &= J_2^{EA}(n_h)s_2\overline{r_K} - J_3^{EA}(n_h)s_3\overline{r_K} \\ &= \left(\left(\widehat{a}_2\frac{s_2}{l_2}+\widehat{a}_3\frac{s_3}{l_3}\right)n_1 - \widehat{a}_3\frac{s_3}{l_3}n_2 - \widehat{a}_2\frac{s_2}{l_2}n_3\right)\overline{r_K} \\ \int_K \mathbf{J}_h^{EA}(n_h)\cdot\nabla\varphi_2 r\,dr\,dz &= J_3^{EA}(n_h)s_3\overline{r_K} - J_1^{EA}(n_h)s_1\overline{r_K} \\ &= \left(\widehat{a}_3\frac{s_3}{l_3}n_1 + \left(\widehat{a}_1\frac{s_1}{l_1}+\widehat{a}_3\frac{s_3}{l_3}\right)n_2 - \widehat{a}_1\frac{s_1}{l_1}n_3\right)\overline{r_K} \\ \int_K \mathbf{J}_h^{EA}(n_h)\cdot\nabla\varphi_{23} r\,dr\,dz &= J_1^{EA}(n_h)s_1\overline{r_K} - J_2^{EA}(n_h)s_2\overline{r_K} \\ &= \left(-\widehat{a}_2\frac{s_2}{l_2}n_1 - \widehat{a}_1\frac{s_1}{l_1}n_2 + \left(\widehat{a}_1\frac{s_1}{l_1}+\widehat{a}_2\frac{s_2}{l_2}\right)n_3\right)\overline{r_K} \end{aligned}$$

The last expression in algebraic form reads as follows

$$A^K \mathbf{n}^K = \mathbf{f}^K,$$

where

$$A^K = \begin{bmatrix} \hat{a}_2 \dfrac{s_2}{l_2} + \hat{a}_3 \dfrac{s_3}{l_3} & -\hat{a}_3 \dfrac{s_3}{l_3} & -\hat{a}_2 \dfrac{s_2}{l_2} \\ -\hat{a}_3 \dfrac{s_3}{l_3} & \hat{a}_3 \dfrac{s_3}{l_3} + \hat{a}_1 \dfrac{s_1}{l_1} & -\hat{a}_1 \dfrac{s_1}{l_1} \\ -\hat{a}_2 \dfrac{s_2}{l_2} & -\hat{a}_1 \dfrac{s_1}{l_1} & \hat{a}_1 \dfrac{s_1}{l_1} + \hat{a}_2 \dfrac{s_2}{l_2} \end{bmatrix} \overline{r_K} \qquad \mathbf{n}^K = \begin{bmatrix} n_1 \\ n_2 \\ n_3 \end{bmatrix}.$$

Summing the above local contributions over each mesh triangle K, we can assemble the global stiffness matrix A of the problem. It is immediate to check that A is a symmetric and positive definite M-matrix (as in the cartesian case), because its entries satisfy the following conditions:

$$\begin{aligned} &A_{jj} > 0 \quad \forall j; && A_{ij} \leq 0 \quad \forall i, j : i \neq j; \\ &A_{jj} \geq \sum_{i=1, i\neq j}^{N_h} |A_{ij}| \quad \forall j; && A_{jj} > \sum_{i=1, i\neq j}^{N_h} |A_{ij}| \quad \text{for at least one } j. \end{aligned} \tag{3.26}$$

Under the regularity assumptions on the problem coefficients and if the triangulation is of Delaunay type, then A is an irreducible M-matrix with respect to its columns and the discrete maximum principle holds for the EAFE method. For a more general diffusion-convection equation, if we assume that the coefficients are piecewise smooth functions and the triangulation is weakly acute, then the stiffness matrix is still an M-matrix [83]. Returning to the original u variable, we have to invert (3.7) at each mesh node, obtaining

$$A^K \mathbf{n} = \left(A^K \begin{bmatrix} e^{-\psi_1} & 0 & 0 \\ 0 & e^{-\psi_2} & 0 \\ 0 & 0 & e^{-\psi_3} \end{bmatrix} \right) \mathbf{u}^K \qquad \mathbf{u}^K = \begin{bmatrix} u_1 \\ u_2 \\ u_3 \end{bmatrix},$$

giving back the two-dimensional Scharfetter-Gummel method on triangular meshes.

Proceeding with the discretization of the reaction term $\int_K c e^{\psi} n_h \varphi_h r\,dr\,dz$ and of the source term $\int_K f_h \varphi_h r\,dr\,dz$ in (3.18), we adopt the same approximation used for the cartesian case in [8] to build the corresponding local matrix and local load vector.

For the reaction term we can invert (3.7) and return to the original variable u before starting with the discretization procedure, having

$$\int_K ce^{\psi} n_h \varphi_h r dr dz = \int_K cu_h \varphi_h r dr dz.$$

We introduce the discretization of the function u using its nodal values u_j over the generic triangle K as $u = \sum_{j=1}^{3} u_j \varphi_j$. Once again, we substitute the test function φ_h with the basis function φ_i, $i = 1,2,3$ defined on the triangle K and in order to approximate the integrals we use a trapezoidal quadrature rule, which for the reaction term yields

$$\begin{aligned}\int_K cu_h \varphi_h r dr dz &= \sum_{j=1}^{3} \int_K c_j u_j \varphi_j \varphi_i r dr dz \\ &= \frac{|K|}{3} \sum_{i=1}^{3} c_i u_i r_i,\end{aligned}$$

where again r_i are the vertex coordinates. We are approximating the integral of a third-degree polynomial (result of the product of three first-degree polynomials), having then a quadrature error of the order of h^2, which is the usual error of the EAFE method. The same procedure and quadrature rule are applied to the source integral, having

$$\int_K f_h \varphi_h r dr dz = \frac{|K|}{3} \sum_{i=1}^{3} f_i r_i.$$

Regarding the boundary term in (3.18), we approximate the integral $\int_{\partial K \cap \Gamma_N} j_N \varphi_h ds_\omega$ using the same argument as before. We need to account for all the edges **e** lying on the Neumann boundary $\partial K \cap \Gamma_N$ of the considered triangle K, therefore we obtain

$$\sum_{\mathbf{e} \in \partial K \cap \Gamma_N} \sum_{i \in \mathbf{e}} \int_{\mathbf{e}} j_N \varphi_i r ds = \sum_{\mathbf{e} \in \partial K \cap \Gamma_N} \frac{|\mathbf{e}|}{2} \sum_{i \in \mathbf{e}} j_{N,i} r_i.$$

At the end of the above discretization procedure, we are able to write the local mass matrix over a triangle K as

$$M^K = \begin{bmatrix} c_1 r_1 & 0 & 0 \\ 0 & c_2 r_2 & 0 \\ 0 & 0 & c_3 r_3 \end{bmatrix} \frac{|K|}{3}$$

and the local load vector as

$$\mathbf{F}^K = \begin{bmatrix} f_1 r_1 \\ f_2 r_2 \\ f_3 r_3 \end{bmatrix} \frac{|K|}{3} + \sum_{\mathbf{e} \in \partial K \cap \Gamma_N} \frac{|\mathbf{e}|}{2} \sum_{i \in \mathbf{e}} j_{N,i} r_i.$$

Therefore, the discretized formulation of the system for the variable u derived above reads as follows

$$\left(A^K \begin{bmatrix} e^{-\psi_1} & 0 & 0 \\ 0 & e^{-\psi_2} & 0 \\ 0 & 0 & e^{-\psi_3} \end{bmatrix} + M^K \right) \mathbf{u}^K = \mathbf{F}^K.$$

Defining the local matrix of the system as

$$\Sigma^K = A^K \begin{bmatrix} e^{-\psi_1} & 0 & 0 \\ 0 & e^{-\psi_2} & 0 \\ 0 & 0 & e^{-\psi_3} \end{bmatrix} + M^K,$$

we can sum the above local contributions over each mesh triangle K and assemble the global matrix Σ of the entire system. In an analogous manner we assemble the global load vector $\mathbf{F}$, so that the linear algebraic system asociated with the EAFE discretization of (3.15) reads

$$\Sigma \mathbf{u} = \mathbf{F}. \tag{3.27}$$

As already pointed out above, the global stiffness matrix is an M-matrix, with the conditions expressed in (3.26) and it is easy to extend these properties to the matrix Σ because the mass matrix is diagonal. One can then prove that for this discretized system in cylindrical coordinates the following theorem applies.

Theorem. *The global matrix Σ of system (3.12) is an irreducible M-matrix with respect to its columns and the discrete maximum principle holds for the EAFE method, under the regularity assumptions on the problem coefficients and if the triangulation is of Delaunay type. Thus, as a consequence, if $\mathbf{F} \geq 0$, then the solution of (3.27) is such that $\mathbf{u} \geq 0$.*

3.4 Substructuring methods

In the present work we study a geometrical configuration (analyzed in Section 4.2.1) where we need to partition the domain into two separate but communicating parts and to solve the system of PDEs in each domain.

To handle this problem, as in [6, 11], we apply a substructuring method properly designed for systems of partial differential equations. For the sake of clarity, we introduce the following simplified model boundary value problem:

$$\begin{cases} -\mathrm{div}\mathbf{J}(u) = f & \text{in } \Omega \\ u = \varphi_D & \text{on } \Gamma_D \\ \mathbf{J}(u)\cdot\mathbf{n} = \varphi_N & \text{on } \Gamma_N. \end{cases} \tag{3.28}$$

The domain Ω is a two-dimensional open bounded set with Lipschitz boundary $\partial\Omega = \Gamma_D \cup \Gamma_N$, such that $\Gamma_D \cap \Gamma_N = \emptyset$, whose outer normal unit vector is denoted by $\mathbf{n}$. We assume for the operator $\mathbf{J}(u) = \mu\left(\nabla u + u\nabla\psi\right)$, that $\mu \in L^\infty(\Omega)$, $\mu(x) \geq \mu_0 > 0$ in Ω and $\psi \in H^1(\Omega)$. Moreover we choose $f \in L^2(\Omega)$ and φ_D, $\varphi_N \in L^\infty(\Omega)$.

Proceeding to a multi-domain formulation, we introduce a partition of the computational domain Ω into two non overlapping subdomains Ω_1 and Ω_2, as schematically depicted in Fig. 3.4.1. The interface $\Gamma = \overline{\Omega_1} \cap \overline{\Omega_2}$ is supposed to be a Lipschitz one-dimensional manifold. We indicate by $u^{(i)}$ the restrictions on Ω_i, $i = 1,2$ of the solution u, and by $\mathbf{n}_i$ the outward normal on of domain Ω_i. Then, our multi-domain

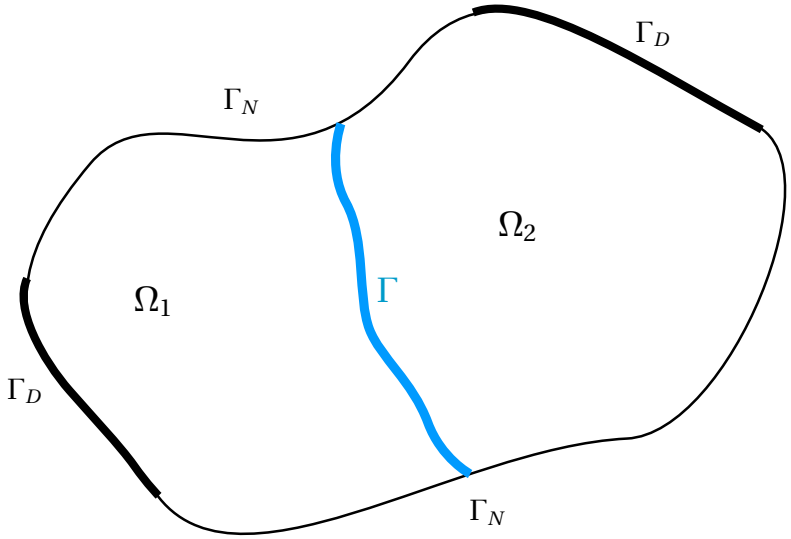

Figure 3.4.1 – Partition of a computational heterogeneous domain Ω into two different parts.

reference problem is:

$$\begin{cases} -\mathrm{div}\,\mathbf{J}\left(u^{(i)}\right) = f_i & \text{in } \Omega_i \\ u^{(i)} = \varphi_D & \text{on } \Gamma_D \cap \partial\Omega_i \\ \mathbf{J}\left(u^{(i)}\right)\cdot \mathbf{n}_i = \varphi_N & \text{on } \Gamma_N \cap \partial\Omega_i \\ [\![u^{(i)}]\!]_\Gamma = 0 & \text{on} \quad \Gamma \\ [\![\mathbf{J}\left(u^{(i)}\right)\cdot \mathbf{n}_i]\!]_\Gamma = 0 & \text{on} \quad \Gamma \end{cases} \tag{3.29}$$

with $i = 1,2$. The last two equations in (3.29) represent the transmission conditions for u and for the flux $\mathbf{J}$ at the interface Γ.

In order to write the weak form for problem (3.29), we introduce the bilinear forms

$$a_{\Omega_i}\left(w^{(i)}, v^{(i)}\right) = \int_{\Omega_i} \mathbf{J}\left(w^{(i)}\right)\cdot \nabla v^{(i)} d\Omega_i, \quad i = 1,2 \tag{3.30a}$$

and the linear functionals

$$F_{\Omega_i}\left(v^{(i)}\right) = \int_{\Omega_i} f v^{(i)} d\Omega_i + \int_{\partial\Omega_i} H v^{(i)}\big|_{\partial\Omega_i}\, ds_i, \quad i = 1,2. \tag{3.30b}$$

In the above notation, we are introducing the flux across $\partial\Omega_i$ defined as $H := \mathbf{J}(u^{(i)})\cdot\mathbf{n}_i$ (that is, for example, $H = \varphi_N$ on Γ_N). The weak multidomain formulation of (3.29) can be obtained using suitable extension operators in order to describe interface conditions. Therefore we have: find $u^{(i)} \in U_i$ such that:

$$a_{\Omega_i}\left(u^{(i)}, v^{(i)}\right) = F_{\Omega_i}\left(v^{(i)}\right) \qquad \forall v^{(i)} \in V_i \tag{3.31a}$$

$$u^{(1)}\big|_\Gamma = u^{(2)}\big|_\Gamma \tag{3.31b}$$

$$\sum_{i=1}^{2} a_{\Omega_i}\left(u^{(i)}, R^{(i)}\eta\right) + F_{\Omega_i}\left(R^{(i)}\eta\right) = 0 \qquad \forall \eta \in \Lambda \tag{3.31c}$$

where the functional spaces are defined as:

$$\begin{aligned} V &:= H^1_{\Gamma_D}(\Omega) = \left\{ v \in H^1(\Omega) :\ v|_{\Gamma_D} = 0 \right\} \\ V_i &:= H^1_{\Gamma_D}(\Omega_i) \\ \Lambda &:= \left\{ \phi \in H^{1/2}(\Gamma) :\ \phi = v|_\Gamma \text{ for a suitable } v \in V \right\} \\ U_i &:= \left\{ v \in H^1(\Omega_i) :\ v|_{\Gamma_D \cap \partial\Omega_i} = \varphi_D \right\} \end{aligned}$$

and where $R^{(i)}\eta$ denotes an extension of $\eta \in \Lambda$ to U_i.

To introduce the discretization of equations (3.31a)-(3.31c) we consider the same finite element discretization introduced in Section 3.3. We define U_i^h and V_i^h as the following finite dimensional subspaces of U_i and V_i:

$$\begin{aligned} U_i^h &:= X_h^1(\Omega_i) \cap U_i = \left\{ v_h \in C^0\left(\overline{\Omega_i}\right) : v_h|_{K_i} \in \mathbb{P}_1(K_i)\ \forall K_i \in T_h \right\} \cap U_i \\ V_i^h &:= X_h^1(\Omega_i) \cap V_i, \end{aligned}$$

that are the spaces of continuous piecewise linear polynomial functions over each subdomain Ω_i. Now we are able to derive the discretized form of system (3.31a)-(3.31c), obtaining:

$$a_{\Omega_i}\left(u_h^{(i)}, v_h^{(i)}\right) = F_{\Omega_i}\left(v_h^{(i)}\right) \qquad \forall v_h^{(i)} \in V_i^h \tag{3.32a}$$

$$u_h^{(1)}\Big|_\Gamma = u_h^{(2)}\Big|_\Gamma \tag{3.32b}$$

$$\sum_{i=1}^{2} a_{\Omega_i}\left(u_h^{(i)}, R_h^{(i)}\eta\right) + F_{\Omega_i}\left(R_h^{(i)}\eta\right) = 0 \qquad \forall \eta \in \Lambda^h \tag{3.32c}$$

where $\Lambda^h := \left\{ \phi \in H^{1/2}(\Gamma) :\ \phi = v|_\Gamma \text{ for a suitable } v \in X_h^1 \right\}$.

It is now possible to write the algebraic counterparts of (3.32a)-(3.32c). For each subdomain the nodes of the computational grid can be divided into three disjoint subsets. Denoting with $\mathbf{u}_\Gamma^{(i)}$ the unknowns at the nodes belonging to Γ, with $\mathbf{u}_D^{(i)}$ the ones on $\Gamma_D \cap \partial\Omega_i$ and with $\mathbf{u}_I^{(i)}$ the internal nodes of each domain Ω_i, we have the vector

$$\mathbf{u}^{(i)} = \begin{bmatrix} \mathbf{u}_I^{(i)} \\ \mathbf{u}_D^{(i)} \\ \mathbf{u}_\Gamma^{(i)} \end{bmatrix}.$$

The algebraic version of (3.32) is then

$$A^{(i)} \begin{bmatrix} \mathbf{u}_I^{(i)} \\ \mathbf{u}_D^{(i)} \\ \mathbf{u}_\Gamma^{(i)} \end{bmatrix} = \begin{bmatrix} \mathbf{b}_I^{(i)} \\ \mathbf{b}_D^{(i)} \\ \mathbf{b}_\Gamma^{(i)} \end{bmatrix} + M^{(i)} \begin{bmatrix} 0 \\ \mathbf{H}_D^{(i)} \\ \mathbf{H}_\Gamma^{(i)} \end{bmatrix} \qquad i = 1, 2, \tag{3.33}$$

where $\mathbf{H}_D$ represents the flux across the Dirichlet sides as well as $\mathbf{H}_\Gamma$ represents the flux across Γ. The matrix

$$A^{(i)} = \begin{bmatrix} A_{II}^{(i)} & A_{ID}^{(i)} & A_{I\Gamma}^{(i)} \\ A_{DI}^{(i)} & A_{DD}^{(i)} & 0 \\ A_{\Gamma I}^{(i)} & 0 & A_{\Gamma\Gamma}^{(i)} \end{bmatrix}$$

is the discretized form of $a_{\Omega_i}(\cdot,\cdot)$, while

$$M^{(i)} = \begin{bmatrix} 0 & 0 & 0 \\ 0 & M_{DD}^{(i)} & 0 \\ 0 & 0 & M_{\Gamma\Gamma} \end{bmatrix}$$

is a sparse block matrix accounting for the quadrature rule adopted when computing the integrals on the right hand side of (3.32a)-(3.32c). $M_{\Gamma\Gamma}$ does not have any domain index, because we have assumed conformity of the two grids over Γ, so that we have $M_{\Gamma\Gamma}^{(1)} = M_{\Gamma\Gamma}^{(2)}$. Therefore the interface conditions are:

$$\mathbf{u}_\Gamma^{(1)} = \mathbf{u}_\Gamma^{(2)} \tag{3.34}$$

$$\mathbf{H}_\Gamma^{(1)} + \mathbf{H}_\Gamma^{(2)} = 0. \tag{3.35}$$

As $\mathbf{u}_D^{(i)}$ is a given datum, we can reduce (3.33) to the following system

$$\begin{bmatrix} A_{II}^{(i)} & A_{I\Gamma}^{(i)} \\ A_{\Gamma I}^{(i)} & A_{\Gamma\Gamma}^{(i)} \end{bmatrix} \begin{bmatrix} \mathbf{u}_I^{(i)} \\ \mathbf{u}_\Gamma^{(i)} \end{bmatrix} = \begin{bmatrix} \mathbf{b}_I^{(i)} \\ \mathbf{b}_\Gamma^{(i)} \end{bmatrix} - \begin{bmatrix} A_{ID}^{(i)} \mathbf{u}_D^{(i)} \\ 0 \end{bmatrix} + \begin{bmatrix} 0 \\ M_{\Gamma\Gamma} \mathbf{H}_\Gamma^{(i)} \end{bmatrix}. \tag{3.36}$$

System (3.36) is the starting point for the development of two different approaches to solve (3.29): the "Schur complement approach" and the one we call "global approach" [7], which we have actually used in our work. The method we have implemented does not impose the transmission conditions in explicit way, so that it does not require the computation of inverse matrices. By doing so, we end up with the following monolithic problem

$$\begin{bmatrix} A_{II}^{(1)} & 0 & A_{I\Gamma}^{(1)} \\ 0 & A_{II}^{(2)} & A_{I\Gamma}^{(2)} \\ A_{\Gamma I}^{(1)} & A_{\Gamma I}^{(2)} & \sum_{i=1}^{2} A_{\Gamma\Gamma}^{(i)} \end{bmatrix} \begin{bmatrix} \mathbf{u}_I^{(1)} \\ \mathbf{u}_I^{(2)} \\ \mathbf{u}_\Gamma \end{bmatrix} = \begin{bmatrix} \mathbf{b}_I^{(1)} - A_{ID}^{(1)} \mathbf{u}_D^{(1)} \\ \mathbf{b}_I^{(2)} - A_{ID}^{(2)} \mathbf{u}_D^{(2)} \\ \sum_{i=1}^{2} \mathbf{b}_\Gamma^{(i)} \end{bmatrix}.$$

The above linear system has clearly a large size but, unlike the Schur complement method, we do not have the need to deal with inverse matrix approximation.

Chapter 4

Numerical Simulation of Bio-Electronic Interfaces

In this chapter, we carry out an extensive validation of all the mathematical models discussed in Chapter 2, showing and critically describing the numerical results we were able to obtain with the application of the numerical methods introduced in Chapter 3.

We can divide the simulations conducted into two cathegories:

- a validation of the PNP model in two dimensional axisymmetric geometries. Using this geometrical model we also study complex configurations, to investigate problems similar to those depicted in Fig. 1.1.1;
- a validation of the model reduction performed in Section 2.3. We discuss the results obtained with the approximations introduced in Section 2.3.1 and then we compare the results of [5] with our area contact lumped models.

For the numerical implementation we use Octave, an open-source language. This choice is motivated by the availability of computer codes developed in previous works for the generation of meshes (octave package msh [10]) and for the construction of the matrices resulting from the spatial discretizations (package bim [9]). We point out that we have contributed to the development of this last package, implementing the EAFE method to solve problems in axial symmetry, using radial and cylindrical coordinates, described in Sections 3.3.1 and 3.3.2.

Stationary and time-dependent problems are linearized using the Gummel Map iterative scheme (see Section 3.2), applied to the different nonlinear problems. The Newton subcycle is dealt with the nonlinear solver fsolve. The tolerances introduced in (3.2), in most of the numerical experiments are chosen as $\epsilon_\varphi \simeq 10^{-4}$ and $\epsilon_c \simeq 10^{-5}$.

4.1 Axisymmetric geometry

The first set of simulations has the goal to provide an accurate validation of the methods implemented in the bim package to deal with axisymmetric configurations. The need to resort to radial and cylindrical coordinates is intrinsic to most of the geometries considered in the description of bio-hybrid devices.

4.1.1 Convergence analysis on a test case for the Octave library

For the validation of the part of bim library developed in the present work, we have conducted a broad range of test cases, for both radial and cylindrical coordinates.

Here we discuss the results of a convergence analysis carried out on a two dimensional advection-diffusion problem (we refer to the model continuity problem (3.6)), solved with cylindrical coordinates on a square domain $\Omega_{as} = [1,2] \times [0,1]$ in a r-z plane (the symmetry axis is then the left side, with coordinates $r = 1$ and z varying between 0 and 1). Given this domain, we apply homogeneous Neumann boundary conditions on the symmetry axis side and Dirichlet boundary conditions on the other three sides. These conditions are enforced in such a way that the exact solution is

$$u_{ex}(r,z) = z^2 \ln r$$

with $\mu = 1$, $\mathbf{b} = [1,1]$, $c = 0$ and f computed accordingly.

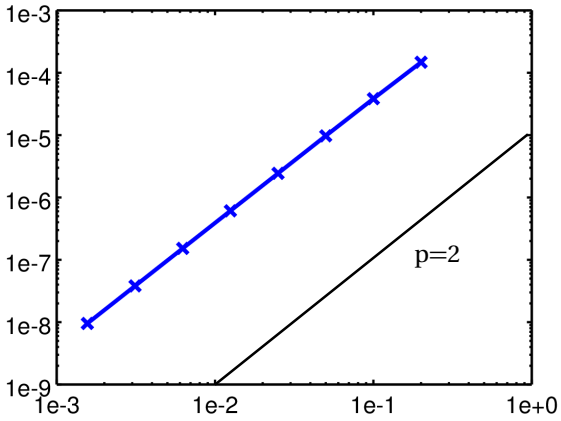

Figure 4.1.1 – Convergence analysis: $\|u_h - u_{ex}\|_{L^2(\Omega)}$ as a function of the mesh size h.

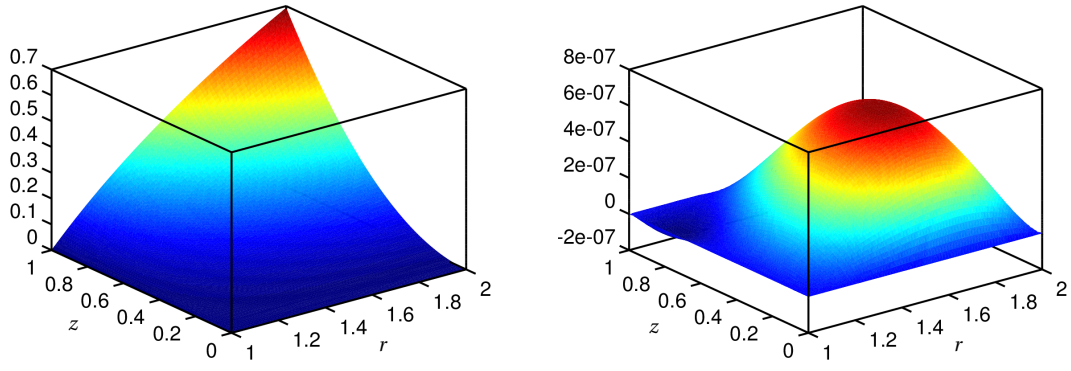

(a) u_h (b) $|u_h - u_{ex}|$

Figure 4.1.2 – Left: numerical solution computed with the Octave library for axysymmetric problems. Right: difference between exact and numerical solutions with $h = 1/80$.

Fig. 4.1.1 illustrates the convergence of the method as a function of the mesh size h. It is remarkable to notice that the numerical solution u_h enjoys the $O(h^2)$ superconvergence behavior to the exact solution u, as explained in Section 3.3 and as proved in [8, 28, 56] for the same EAFE method in cartesian coordinates. The spatial distribution of the absolute value of the error between this analytical solution and our numerical solution is shown in Fig. 4.1.2-(b) for a mesh size $h = 1/80$.

4.1.2 A biological test case solved with radial and cylindrical coordinates

One dimensional simulation

We tested our library also on a biological case, solving the model presented in [38], where the authors derive an analytical solution of a Poisson-Nernst-Planck system in radial coordinates under the assumption of axial symmetry. Their model refers to the middle plane of a cleft between a cell and a substrate as in the general setup described in Section 2.3 and with the following simplifications:

- ions are assumed to flow only in the radial direction, so that $j_{i,\phi} = j_{i,z} = 0$. Beside the pure radial current flow, no dependence on ϕ and z is assumed: the radial coordinate r is the only independent variable and in the interval $[0, R]$ (R being the cell radius);

- three types of ions are considered (potassium, sodium and chloride) and in this

model only K^+ ions can flow from the inside of the cell to the outside. The influx of K^+ ion charge per volume and per time is given by $\lambda_K = j_K^{tm}/\delta_j$, where δ_j is the cleft width and j_K^{tm} is the potassium current density through the membrane, here assumed to be constant;

- there is no influence on the flux of ions inside the cleft from the two boundaries (the cell-cleft and the chip-cleft interfaces), neglecting the capacitive couplings described in Section 2.2.4;

- only the stationary case is considered, meaning that all quantities are independent of time.

Imposing at $r = R$ Dirichlet boundary conditions at bath values for both the potential and the concentrations, the analytical solution for the potential φ for this particular one dimensional PNP system is the following [38]

$$\varphi(r) = kR^2 \left[\left(1 - \frac{r^2}{R^2}\right) + 4\frac{\lambda_{Debye}^2}{R^2} \left(\frac{I_0\left(r/\lambda_{Debye}\right)}{I_0\left(R/\lambda_{Debye}\right)} - 1 \right) \right] \tag{4.1}$$

where k is a suitable constant, λ_{Debye} is the Debye length[1] of the bath and I_0 is the modified Bessel function of the first kind (for the details see [38]). In this case, the second term in the bracket can be neglected, because $\lambda_{Debye} \ll R^2$ and the potential is then reduced to a parabolic term. From this expression the authors also calculate

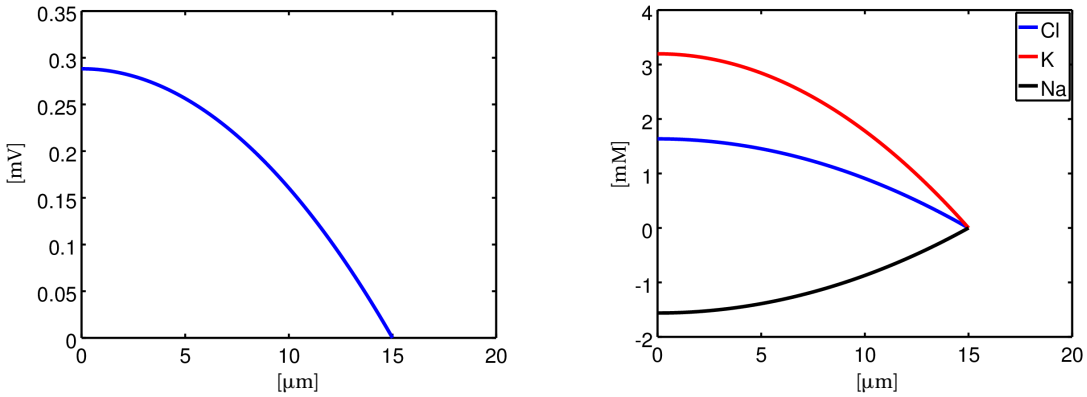

(a) Potential φ (b) Concentrations c_i

Figure 4.1.3 – On the left: radial profile of the potential $\varphi(r)$. On the right: radial profile of the changes of ion concentrations with respect to their bath values $c_i(r) - c_i^{bath}$. Results obtained with a source term $\lambda_K = 11\,\text{pA}\,\mu\text{m}^{-2}$ and a cell radius $R = 15\,\mu\text{m}$.

[1]The Debye length of the bath has the following expression: $\lambda_{Debye} = \sqrt{\epsilon_0 \epsilon_r k_B T / q^2 c_{tot}}$

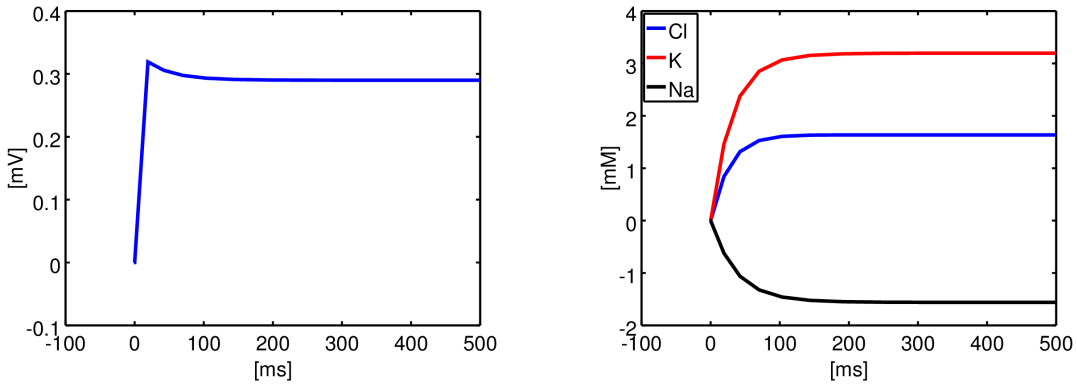

(a) Potential $\varphi(t, r=0)$ (b) Concentrations $c_i(t, r=0)$

Figure 4.1.4 – Time variation of the potential and of the concentrations with respect to their bath values, at the centre of the junction.

the ion charge densities inside the cleft: again the r-dependent terms are grouped into a leading parabolic term proportional to $R^2(1-r^2/R^2)$, and a smaller one that can be neglected.

As shown in Fig. 4.1.3, the results obtained with our numerical tool are in very good agreement with the analytical solutions. Under the hypotheses illustrated above, the potential variation at $r=0$ is really small (less than 1 mV) and the absolute changes of ion concentrations for Cl^- and Na^+ are quite small too. Only the change of the K^+ ion concentration is considerable: from 5 mM to 8 mM.

We also conduct a time dependent simulation of this experimental setup, redefining the transmembrane current as $\lambda_K(t)=\lambda_K H(t)$, where λ_K is the constant current used in the static formulation and $H(t)$ is the Heaviside function, defined in such a way that $H(t)=0$ for $t<0$ and $H(t)=1$ for $t\geq 0$. With this mathematical definition of the the potassium injection, we are considering an instantaneous opening of the K^+ channels at $t=0$, which leads to a time variation of the quantities φ and c_i (see Fig. 4.1.4, where we show the variation of these functions evaluated at $r=0$). According to the time dependent results presented in [55], the transients are exhausted in about 150 ms. Moreover, the stationary limits of φ and c_i are consistently the same as the static case shown in Fig. 4.1.3.

One dimensional simulation with a larger domain

In this section, we study the same model as in the previous paragraph [38], but besides the electrolyte under the cell, we also include in the problem a portion of elec-

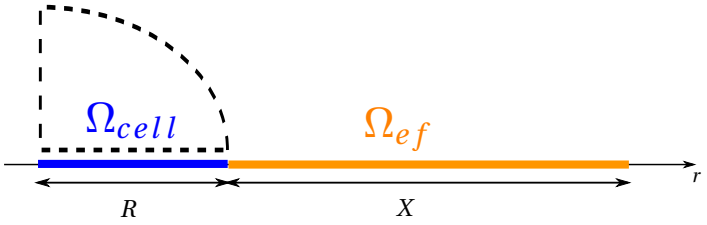

Figure 4.1.5 – One dimensional geometry for the axisymmetric problem. The domain is $\Omega = \Omega_{cell} \cup \Omega_{ef}$ (cell radius $R = 10\,\mu m$).

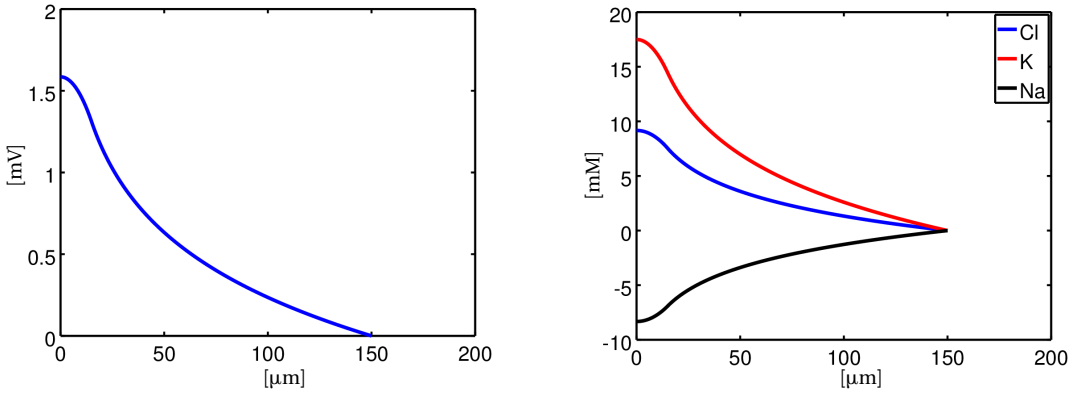

(a) Potential φ (b) Concentrations c_i

Figure 4.1.6 – On the left: radial profile of φ. On the right: radial profile of the changes of ion concentrations with respect to their bath values $c_i(r) - c_i^{bath}$. Results obtained with a cell radius $R = 15\,\mu m$ and free space $X = 10R$.

trolyte nearby it, as depicted in Fig. 4.1.5. The entire domain Ω is the union of two different parts: the attached area Ω_{cell} (R is the cell radius) and the free part Ω_{ef}, whose width is here called X. We can set the whole domain amplitude at $W = R + X$. At $r = W$ we impose Dirichlet boundary conditions at bath values and we carry out a parametric analysis changing the amplitude of Ω_{ef}, to study the decay of the potential and of the concentrations.

In Fig. 4.1.6 we can see the radial profiles of φ and of the concentrations, with a domain amplitude $W = R + X = R + 10R$ and we see that the trend has a decay similar to $\ln r$ in the free part, which is a solution of the diffusion problem in radial coordinates. The central value is higher than in Fig. 4.1.3, and the decay is slower than the physical one, because we are extending the author's hypothesis of neglecting the couplings also in Ω_{ef}, instead of using the electrolyte-electrolyte artificial coupling conditions introduced in Section 2.2.4. This approximation results in the radial distributions shown in Fig. 4.1.6, where φ and c_i do not approach their bath values with

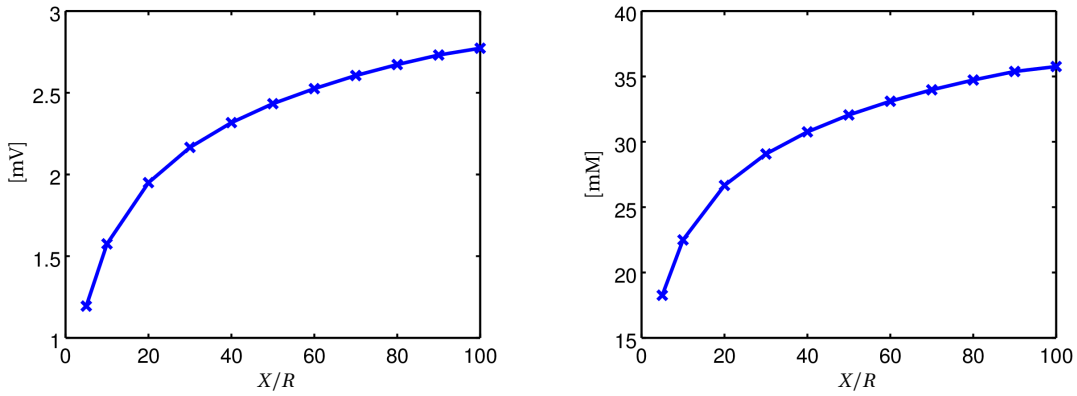

(a) Potential $\varphi(r=0)$ (b) Concentration $c_K(r=0)$

Figure 4.1.7 – Parametric analysis of the potential and of the potassium concentration at the centre of the junction as a function of the size of the domain.

the physically expected rapidity: this is due to the fact that the ions are not allowed to flow outside the domain.

The parametric analysis in Fig. 4.1.7 gives us an idea of the variation of $\varphi(r=0)$ and $c_K(r=0)$ with different domain configurations (from $X=5R$ to $X=100R$): the trend is logarithmically increasing, which means that it continues growing, unlike what one should expect. Again the reason of this behavior is that we are not accounting for the ion flow in the overlying electrolyte. This could be overcome in the same spirit of the treatise of Section 2.3.1 with the addition of a term in the continuity equations in the following way

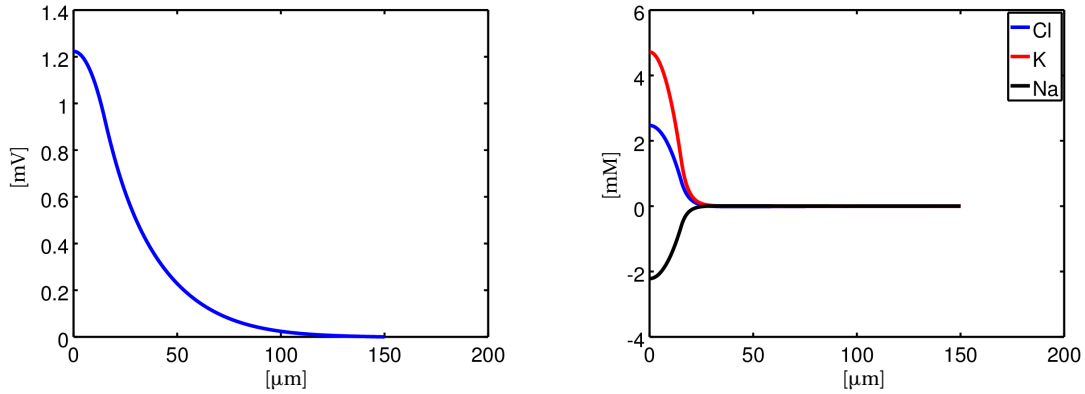

(a) Potential φ (b) Concentrations c_i

Figure 4.1.8 – Results accounting for the ion fluxes outside the cleft, solving (4.2). Profiles of φ and of $c_i(r)-c_i^{bath}$ in the case of a cell radius $R=15\,\mu$m and a free space $X=10R$.

$$\frac{\partial c_i}{\partial t} + \mathrm{div}\mathbf{f}_i = \lambda_K|_{\Omega_{cell}} - \frac{v_i^*}{\delta_j}\left(c_i - c_i^{bath}\right)\Big|_{\Omega_{ef}}. \tag{4.2}$$

Beside the current rate λ_K injected in Ω_{cell}, we give the ions the possibility to flow from Ω_{ef} into the surrounding extracellular fluid, in a way consistently similar to that introduced in (2.20), using for v^* a value around $1 \times 10^{-5}\,\mathrm{m\,s^{-1}}$. The results obtained solving (4.2) in the PNP system are shown in Fig. 4.1.8: as expected, we see a faster decay to the bath values in the Ω_{ef} part for the potential and the concentrations.

Two dimensional simulation

In order to check the accuracy of the one dimensional approximation, we solve the model studied in [38] in a two dimensional geometry with cylindrical coordinates. We consider a cross section in the *r-z* plane, so that we are actually dealing with a three dimensional description, thanks to the symmetry with respect to the ϕ- coordinate. We choose the geometry represented in Fig. 4.1.9, describing the entire electrolyte bath surrounding the cell, in order to have an accurate description of the involved phenomena to be compared with our radial solution.

The boundary conditions for this model are represented in Fig. 4.1.9. Referring to the framework of Section 2.2.5, they are specified as follows:

- on Γ_{sim} we impose homogeneous Neumann conditions on both potential and concentrations, as required by the axial symmetry;

- on Γ_{sub} we have the chip interface: we can consider a coupling condition for the potential with a substrate capacitance C_S, as described in Section 2.2.4, or we can neglect the device influence, setting $C_S = 0$ in (2.16), to reproduce results similar to [38];

- on Γ_{cell} we again can choose whether to have or not the capacitive coupling described in Section 2.2.4 for the potential, but we have to impose a transmembrane current injected from all over this part of boundary. This can be managed either with a fixed flux or with the models for the transmembrane currents introduced in (2.10) and (2.11);

- on Γ_b (the external ellipse) we impose Dirichlet boundary conditions at bath values for all the involved quantities.

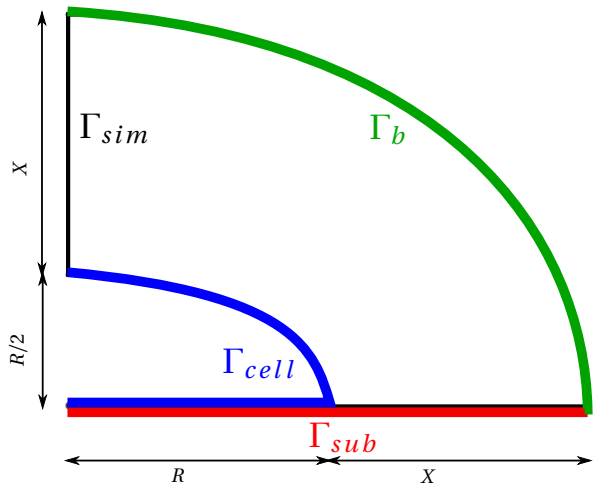

Figure 4.1.9 – Two dimensional geometry for the axisymmetric problem: cross section in the r-z plane including the electrolyte surrounding the cell. Dimensions: $R = 15\,\mu m$ and $X = R$. The cell is approximated as an ellipsoid with the major semiaxis equal to R and the other one equal to $R/2$. The cleft is the line between Γ_{cell} and Γ_{sub}: its height is $\delta_J = 100\,nm$.

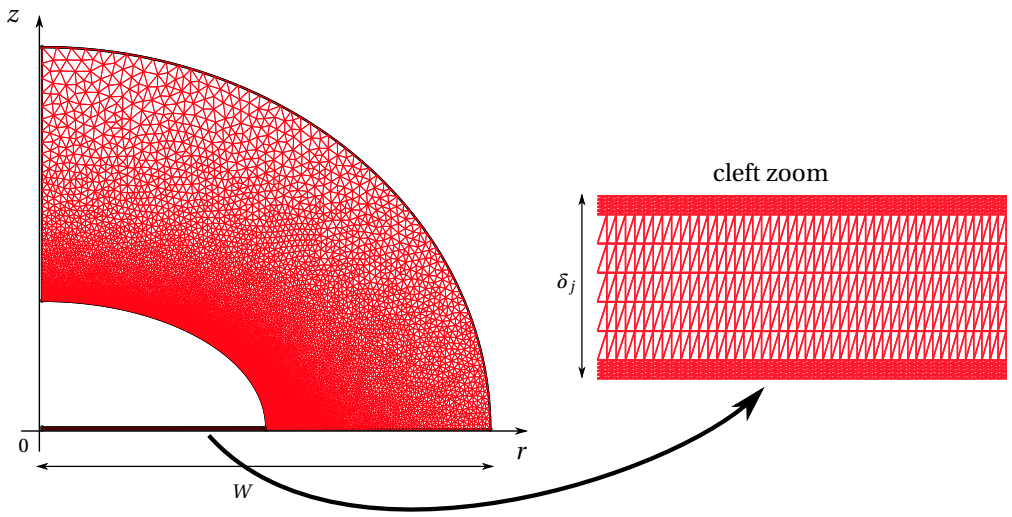

Figure 4.1.10 – Mesh for the axisymmetric geometry of Fig. 4.1.9: the mesh is refined all around the cell. On the right: zoom of a part of the cleft zone, where the mesh is structured and refined at the boundaries. The mesh is generated with the software Gmsh.

The mesh used in the numerical computations is shown in Fig. 4.1.10 and is unstructured because of the cell curvature. However, we use a structured mesh in the cleft between the cell and the chip (its height is $\delta_j = 100\,nm$) in order to independently control the refining in the r and in the z directions and to achieve a more detailed description of this area. This is required because we are considering a multiscale problem: the domain is quite big but the most interesting phenomena take place in a thin part, three orders smaller than the cell radius. The number of nodes is more

than 10000.

The first case we investigate is the same studied in radial coordinates above, neglecting the capacitive couplings and using a constant trasmembrane current. As one can observe in Fig. 4.1.11, the results are in good agreement with the ones presented in [38] and with the ones presented in Fig. 4.1.3-4.1.6. The area where most of the phenomena occur is the thin sheet of electrolyte between cell and chip, in the rest of the domain the decay to electroneutrality is very fast. Another parametric analysis is presented (see Fig. 4.1.12), with a variation of the size of the domain: the increasing trend found for φ and c_i is smaller here than in Fig. 4.1.7 and it stops varying long before than in the one dimensional model. This confirms that the one dimensional approximation is quite inaccurate when it does not account for the electrolyte all around, where the ions can actually flow.

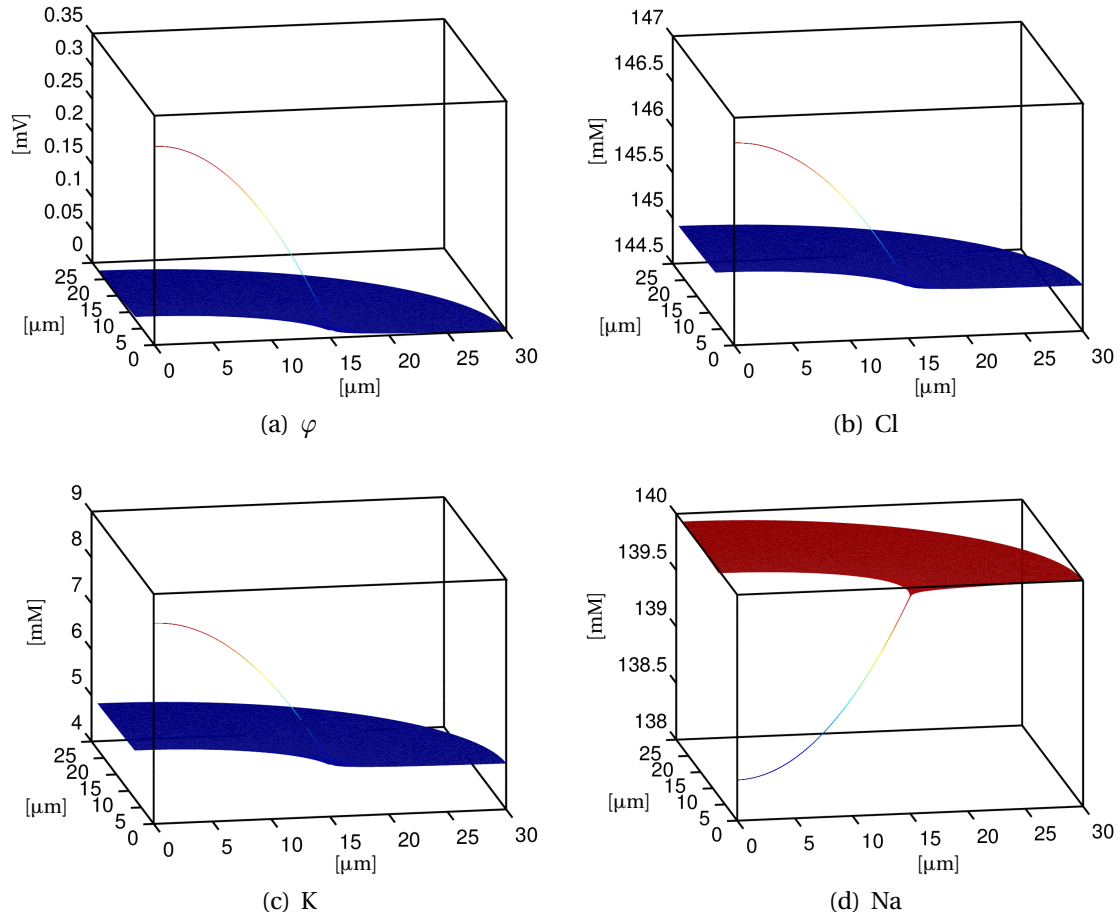

(a) φ (b) Cl

(c) K (d) Na

Figure 4.1.11 – Spatial distribution of φ and of c_i in a configuration with $X = R$: the only region of interest for the phenomena is the thin cleft between cell and substrate.

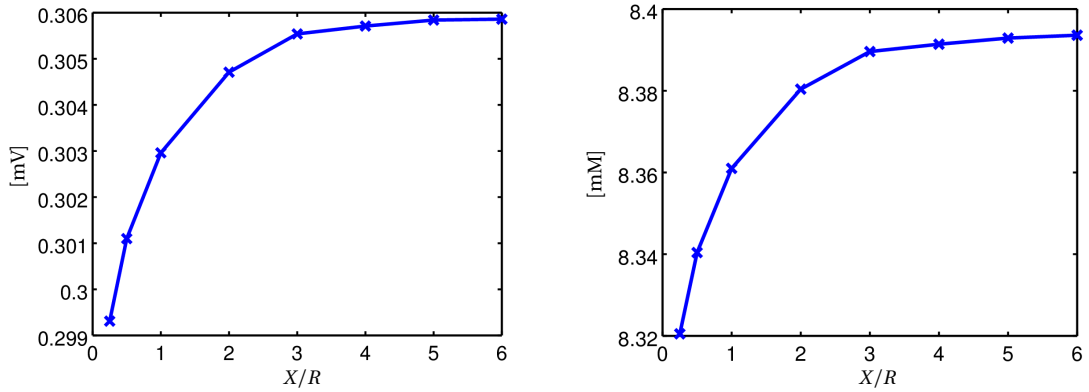

(a) Potential $\varphi(r=0, z=0)$ (b) Concentration $c_K(r=0, z=0)$

Figure 4.1.12 – Parametric analysis of the potential and of the potassium concentration at the centre of the junction as a function of the size of the domain.

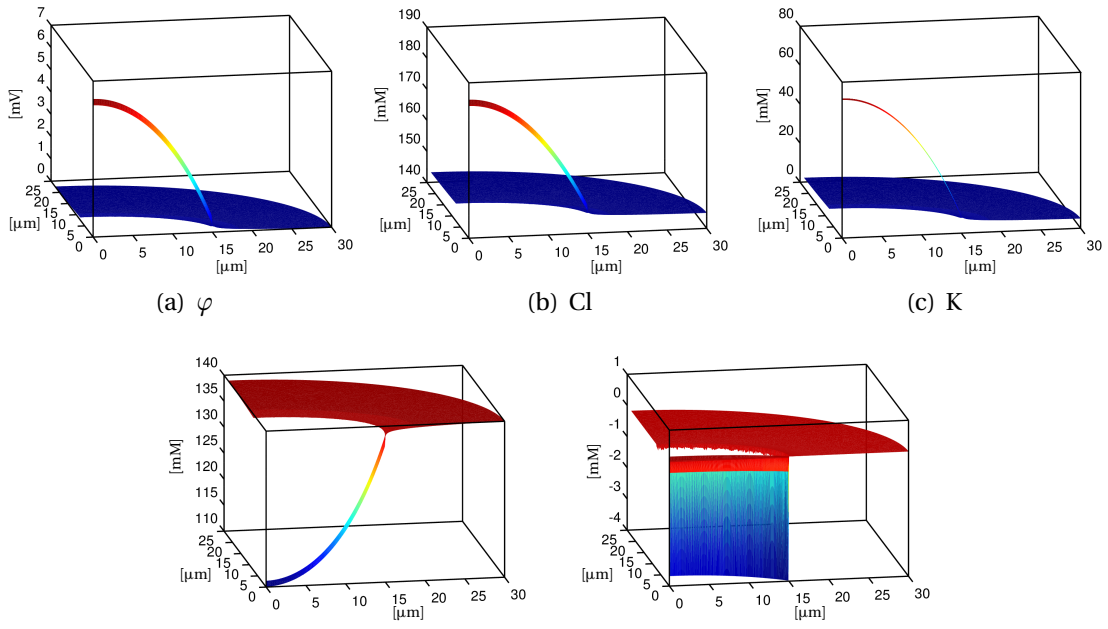

(a) φ (b) Cl (c) K

(d) Na (e) ρ

Figure 4.1.13 – Spatial diastribution of the potential φ, of the concentration c_i and of the total charge density ρ, in a configuration with $X = R$ with a capacitive coupling between cell and electrolyte ($C_M = 1 \times 10^{-2}\,\mathrm{F\,m^{-2}}$) ans substrate and electrolyte ($C_S = 0.3 \times 10^{-2}\,\mathrm{F\,m^{-2}}$). Results obtained with a depolarizing pulse keeping $V_{cell} = 50\,\mathrm{mV}$.

With the geometry presented in Fig. 4.1.9, we solve the same problem as before, but modeling the transmembrane currents with both the Goldman-Hodgkin-Katz model and the resistive model described in Section 2.2.4. We also increase the model complexity simulating a voltage-clamp stimulation from the cell (the same depolar-

ization of [5]): we account for the cell and for the electronic substrate with two capacitive couplings at the two boundaries Γ_{cell} and Γ_{sub} (see Section 2.2.4). Fig. 4.1.13 shows the results obtained with the GHK model. We notice a consistently higher variation of the quantities in the cleft than before (ion injection from the membrane is here better represented) and also steep layers due to the capacitive couplings and charge screening effects. Now the electrolyte away from the cleft is not everywhere electroneutral, but there is a little more evident decay nearby the cell.

4.2 Stimulation in complex configurations

In the present work we have started our analysis from a single cell on an electronic substrate and we have also studied in Section 4.1 a three dimensional geometry considering the electrolyte all around the cell. We now investigate configurations with more than just one cell and/or more than just one electrode, to understand the behavior of these type of couplings and the mutual influence between one bio-electronic device and another one in its neighborhood.

The results presented in this section are obtained solving the PNP system (2.4) in

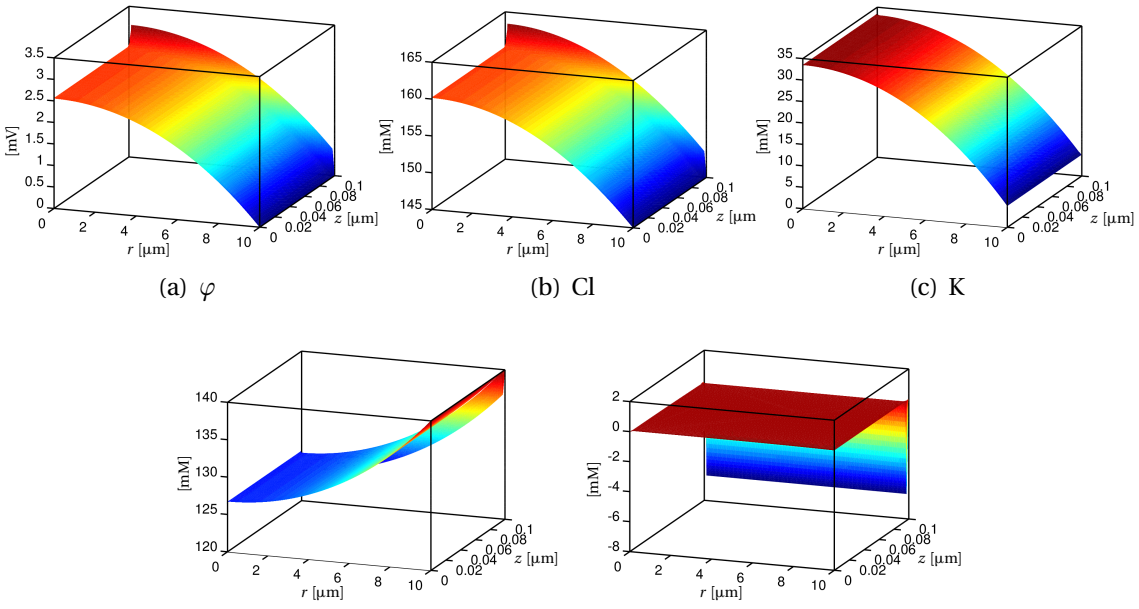

(a) φ (b) Cl (c) K

(d) Na (e) ρ

Figure 4.2.1 – Spatial diastribution of φ, of c_i and of the total charge density ρ in the portion of electrolyte between cell and substrate. Results at the end of a transient, after an impulse applied to the cell as in [5]. GHK model for the transmembrane currents. Cell radius: $R = 10\,\mu$m.

a two dimensional cross section of the three dimensional geometry, knowing that if we take into account the effect of the capacitive couplings we have to expect steep layers at these boundaries, as seen in Fig. 4.1.13 and as also described in [3]. In [3], the author shows some results in a x-z plane of the electrolyte cleft under the cell and in Fig. 4.2.1 we reproduce these results using cylindrical coordinates. This is actually a zoom of the cleft area of Fig. 4.1.13 and it is our starting point to proceed in approaching more complex configurations. We also see that the hypotheses on the distributions along the z-direction introduced in Section 2.3.1 are verified.

4.2.1 Cell to chip stimulation

The geometry of this first case is represented in Fig. 4.2.2: there are one cell and two electrodes, one placed under the centre of the cell and the other one at a distance W from the cell. The goal of the conducted simulations is to study the current measured by the second electrode after a voltage-clamp stimulation of the cell.

This geometrical model lends itself to the use of cylindrical coordinates, interpreting the left vertical side of the boundary as a symmetry axis. Approximating the cell as a half sphere or ellipsoid, one can rotate the domain in Fig. 4.2.2 around the chosen axis and be able to represent the whole three dimensional thin sheet of electrolyte we are interested in. This is of course an ideal representation of the actual structure because in this way the second electrode is all around the cell, but it can still be a sound model to gain accurate physical results.

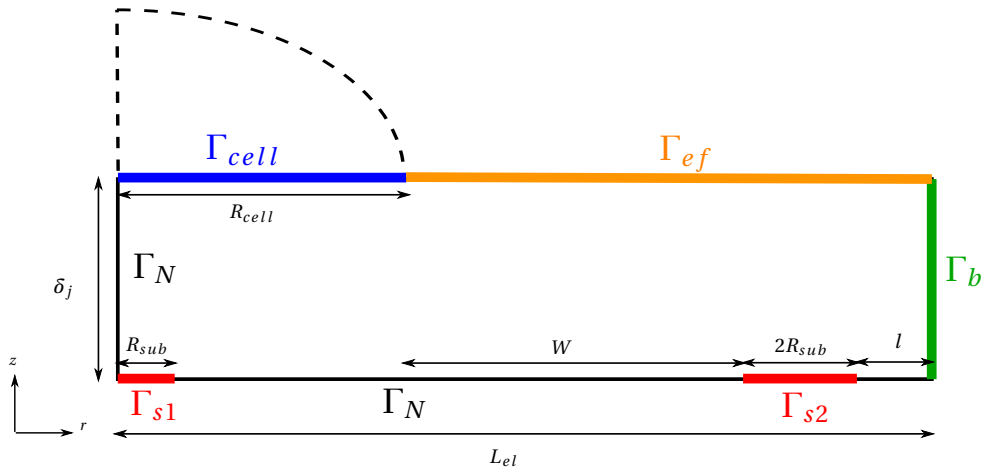

Figure 4.2.2 – Domain with two electrodes for a cell to chip stimulation. The figure is not in scale for ease of representation (in reality: $\delta_j = 100\,\text{nm}$, $R_{cell} = 10\,\mu\text{m}$, $R_{sub} = 1.5\,\mu\text{m}$). The width l of the part of electrolyte on the right is fixed at $20\,\mu\text{m}$: we need to set on Γ_b the usual "far field" conditions.

The applied boundary conditions refer to (2.22)-(2.23). Moreover, this configuration is the one we use to test and study the parameters introduced in Section 2.2.4 to model the boundary part Γ_{ef}. A parametric analysis conducted with the variation of C^*, v^* and of the width W leads us to obtain confidence intervals for these two artificial constants, in order to get physically acceptable solutions. After that, we use the procedure discussed at the end of Section 2.2.4, comparing this terms with the current injected from the membrane and with the cell capacitive coupling. This way, we are able to choose the fractions $1/\kappa$ of the membrane current fluxes and of the capacitance. The resulting best-fitting values used in all our simulations are $v_K^* = 1\times10^{-5}\,\mathrm{m\,s^{-1}}$ and $C^* = 1\times10^{-5}\,\mathrm{F\,m^{-2}}$.

As one can observe in Fig. 4.2.3, varying the distance W brings noticeable differences in the spatial distribution of the quantities of interest, especially φ. The

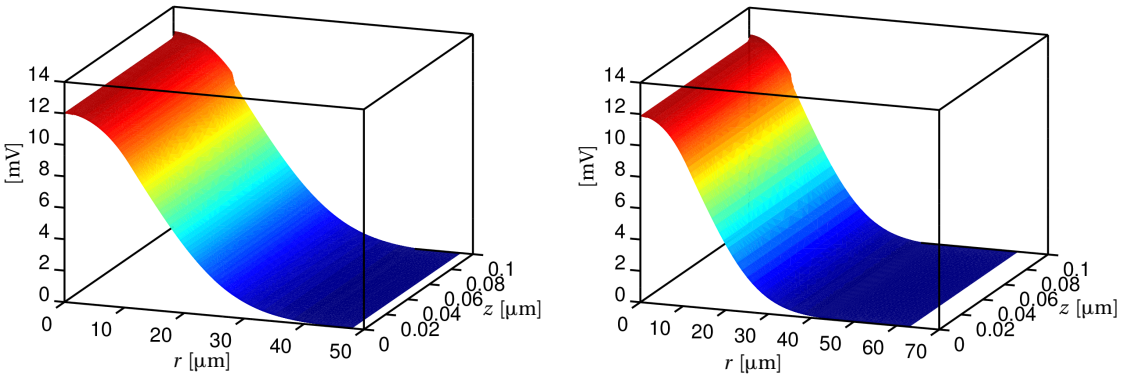

(a) $W = 15\,\mu\mathrm{m}$ (b) $W = 30\,\mu\mathrm{m}$

Figure 4.2.3 – Spatial distribution of the potential φ with different domains: the distance between the cell and the second gate is on the left $W = 15\,\mu\mathrm{m}$ and on the right $W = 30\,\mu\mathrm{m}$. In both cases: $\delta_j = 100\,\mathrm{nm}$.

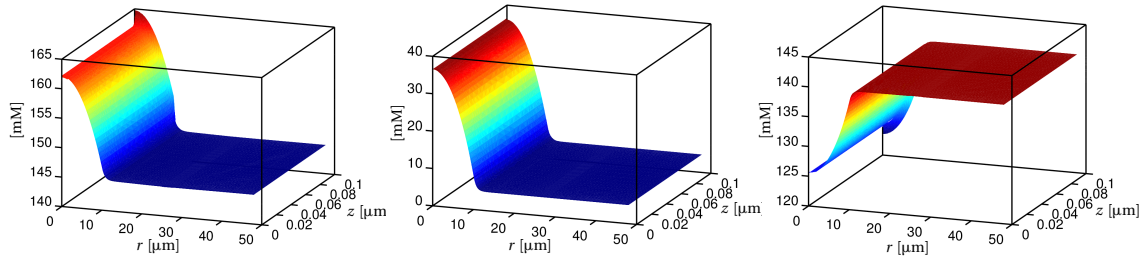

(a) Cl (b) K (c) Na

Figure 4.2.4 – Spatial distribution of the concentrations c_i with a distance between the cell and the second gate $W = 15\,\mu\mathrm{m}$ and $\delta_j = 100\,\mathrm{nm}$.

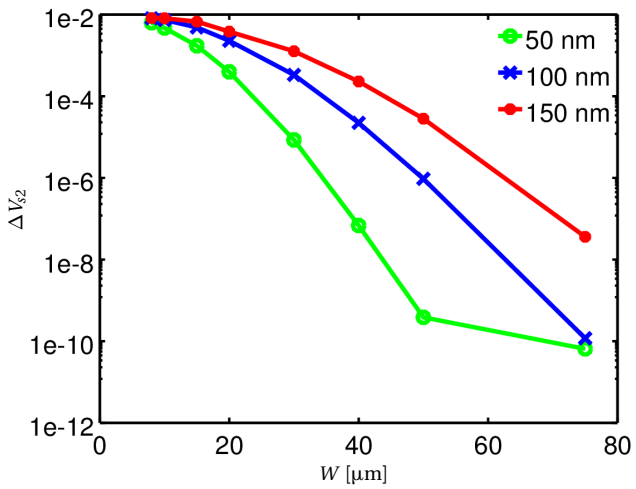

Figure 4.2.5 – Parametric semilogarithmic analysis for ΔV_{s2} as a function of the distance W. Results for three different values of the cleft thickness δ_j, obtained with a depolarizing pulse with $V_{cell} = 50\,\text{mV}$.

potential relaxes to a neutral state with a $1/r$ decay. At a distance W around $15\,\mu\text{m}$ the influence on the second electrode is still evident, because it is not already decayed at the bath value of reference, but it is completely different when this distance increases, as one can see in Fig. 4.2.3-(b). The concentrations c_i are shown in Fig. 4.2.4, and both their values and their distributions are very close to the case with only the cell (of Fig. 4.2.1), with steep layers near Γ_c because of the strong coupling, and with a decay to their bath value almost at the end of the attached area.

The parametric analysis we have carried out is reported in Fig. 4.2.5, where we show the variation of the following computed integal mean

$$\Delta V_{s2} = \frac{\int_{\Gamma_{s2}} \left(\varphi\big|_{\Gamma_{s2}} - V_{s2} \right) d\gamma}{|\Gamma_{s2}|},$$

which measures the difference of potential between substrate and electrolyte at the second gate. The current at the electrode can be obtained multiplying ΔV_{s2} by a specific conductance g_s (for a physical value of g_s see [5]). We conduct the same analysis for three different values of the cleft thickness δ_j (50, 100 and 150 nm) and for each fixed δ_j, we observe a fast and almost exponential decreasing when considering a farther electrode.

Moreover, as one can observe in Fig. 4.2.6, a smaller value of δ_j gives rise to an increase of the potassium concentration and consequently of the potential in the portion of electrolyte under the cell, but the phenomena tends to take place only in

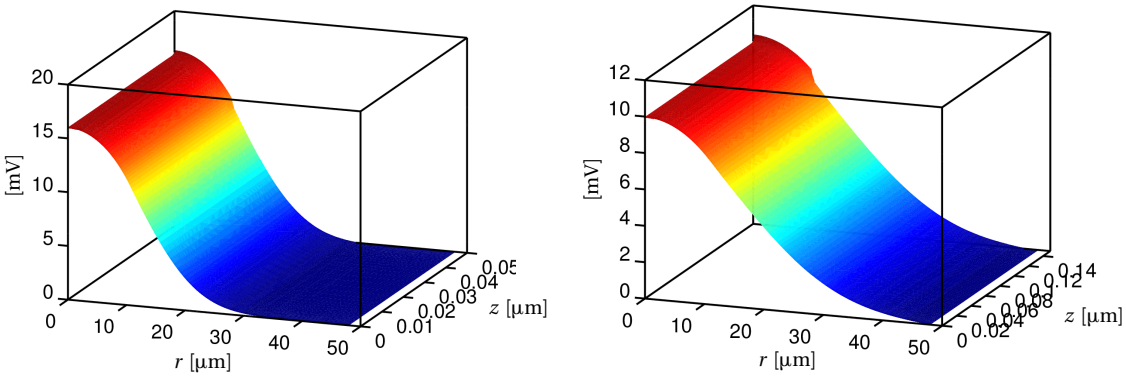

(a) $\delta_j = 50\,\text{nm}$ (b) $\delta_j = 150\,\text{nm}$

Figure 4.2.6 – Spatial distribution of the potential φ with different domains: the distance between the cell and the second gate is set at $W = 15\,\mu\text{m}$, but on the left we have a cleft thickness $\delta_j = 50\,\text{nm}$ and on the right $\delta_j = 150\,\text{nm}$.

this little part. The decay to the bath values of the quantities is faster in the configuration with $\delta_j = 50\,\text{nm}$, as shown by the spatial distribution of φ in Fig. 4.2.6-(a). The parametric analysis reflects this result: in Fig. 4.2.5 we see that the value of ΔV_{s2} decreases with the cleft thickness, at every chosen W. A physical explanation for this latter result can be found by applying the definition of electrical resistance to the considered portion of electrolyte. We are allowed to do that, because the electrolyte solution is an electrical conductor, therefore we have

$$R_{el} = \rho_{el} \frac{L_{el}}{S_{el}},$$

where ρ_{el} is the electrolyte resistivity, L_{el} is the amplitude of the domain (see Fig. 4.2.2) and S_{el} is a y-z cross section of the electrolyte, linearly proportional to the cleft thickness δ_j. A smaller value of δ_j brings then a bigger resistance R_{el}, resulting in the faster decay of the potential, as shown in Fig. 4.2.6.

4.2.2 Cell to cell stimulation

The second configuration studied in the cross section of a general three dimensional domain is depicted in Fig. 4.2.7. In this case, we want to characterize the influence that one cell can have on another one placed in its neighborhood. This configuration, in principle, cannot be studied using cylindrical coordinates, because the left part of the boundary is not the symmetry axis of a rotational solid. To overcome this problem and to use cylindrical coordinates in axial symmetry, we apply a substructuring

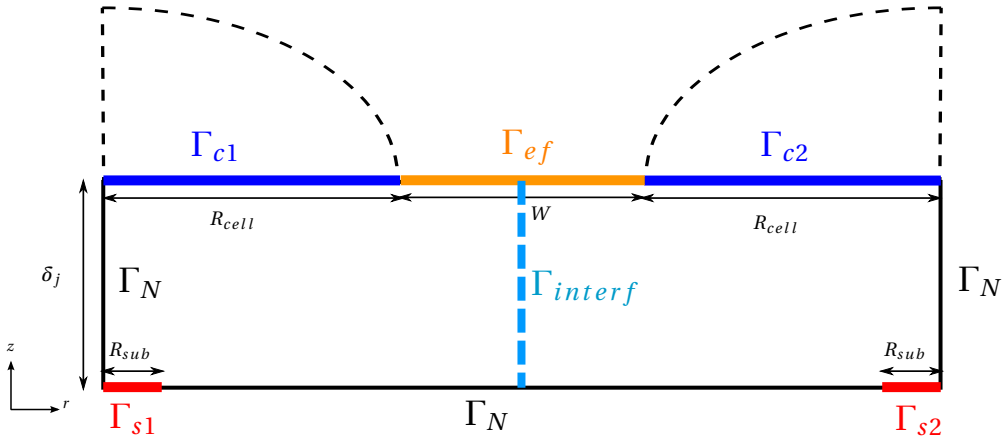

Figure 4.2.7 – Domain with two cells and two electrodes. The figure is not in scale for ease of representation (in reality: $\delta_j = 100\,\text{nm}$, $R_{cell} = 10\,\mu\text{m}$, $R_{sub} = 1.5\,\mu\text{m}$). Γ_{interf} is an artificial boundary introduced to divide the domain into two identical parts.

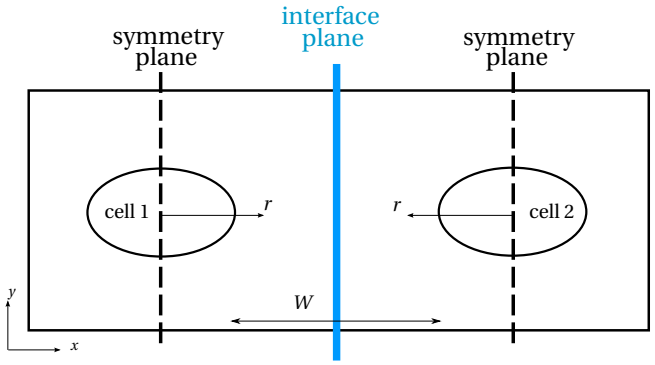

Figure 4.2.8 – Schematics for the geometry with two cells: cross section in the x-y plane of the three dimensional configuration, studied in the computational domain z-r depicted in Fig. 4.2.7. We divide it into two parts, each one with its symmetry axis and with its radial coordinate r.

method (see Section 3.4).

In order to do that (referring to Fig. 3.4.1), we artificially introduce a new side Γ_{interf}, dividing the domain into two parts that geometrically are identical, and we use the left and the right sides of the boundary as symmetry axis for each part. Fig. 4.2.8 shows a representation of a cross section in the x-y plane of the entire three dimensional problem. The two axis lie on the symmetry planes depicted in Fig. 4.2.8 and Γ_{interf} lies on the artificial interface plane. Then, we solve in a monolithic fashion the same model in each of these two parts (boundary conditions are applied as in Fig. 4.2.7, referring to (2.22)-(2.23)), using the interface conditions (3.34)-(3.35) on Γ_{interf} and thanks to this procedure we are able to describe the coupling between two cells considered to be geometrically identical. The accuracy of this approxima-

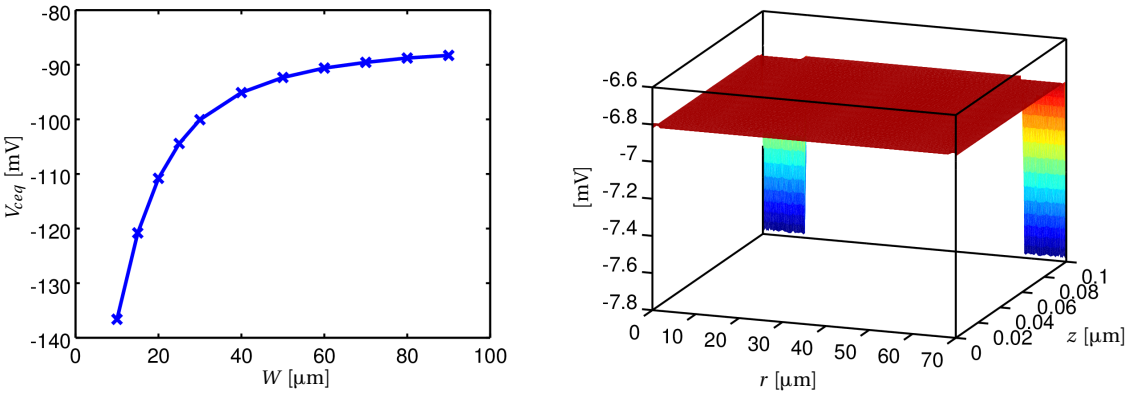

(a) V_{ceq} (b) φ at $W = 50\,\mu\text{m}$

Figure 4.2.9 – Left: intra-cellular potential of equilibrium (corresponding to a non-opening of the transmembrane channels) as a function of the distance W. Right: spatial distribution of φ in an equilibrium configuration (the cells are not polarized), obtained solving the PNP system with the addition of (4.3), with a chosen $W = 50\,\mu\text{m}$.

tion increases the larger the distance W is.

In all the models of the present work we are considering the intra-cellular potential as a function constant in space. This is of course an approximation, which has to be carefully dealt especially in this case: in a full description one should study the potential not only in the external electrolyte, but also inside the cell. In order to perform a cell to cell stimulation, we need to set the intra-cellular potential of the second cell at a non-polarized value (corresponding to a state of equilibrium, without the opening of the transmembrane channels, that gives the so called "resting membrane potential"). This value can be computed by setting to zero the integral mean on Γ_{c1} and Γ_{c2} of transmembrane currents, in the following way (when using a resistor model)

$$\frac{\int_{\Gamma_{c1}} \left(V_{c1} - \varphi\big|_{\Gamma_{c1}} + \frac{V_{th}}{z_K} \ln \frac{c_K^{c1}}{c_K|_{\Gamma_{c1}}} \right) d\gamma}{|\Gamma_{c1}|} = \frac{\int_{\Gamma_{c2}} \left(V_{c2} - \varphi\big|_{\Gamma_{c2}} + \frac{V_{th}}{z_K} \ln \frac{c_K^{c2}}{c_K|_{\Gamma_{c2}}} \right) d\gamma}{|\Gamma_{c2}|} = 0. \qquad (4.3)$$

Therefore, a new unknown variable $V_{ceq} = V_{c_1} = V_{c_2}$ is introduced. We need to compute this intra-cellular potential using the usual PNP model with the addition of (4.3), having then a closed system to solve. The V_{ceq} computed as a result of this problem is shown in Fig. 4.2.9-(a) for different distances W between the two cells. When the cells are close to each other, this potential is low because they have a big mutual influence, but when the distance becomes larger than two cells diameters, the intra-cellular potential stabilizes itself around a value of -90 mV, which is near to the physical values of equilibrium reported in [5, 13, 54]. Fig. 4.2.9-(b) shows the spatial distribution of

the potential φ in the electrolyte when we solve this particular "equilibrium problem": the profile is flat except for the steep layers near Γ_{c1} and Γ_{c2} resulting from the strong coupling with the cells, and the value of φ is around -6.8 mV. The negative sign is due to the fact that the cells are at a non-polarized state, which is obtained with a negative V_{ceq}.

Having determined the value of the intra-cellular potential for each configuration, we can now study the influence of the stimulated cell on the other one, which should be considered set at the corresponding V_{ceq} value with a voltage-clamp tecnique. We study a stimulation consisting of the usual depolarizing pulse keeping the first cell intracellular potential at 50 mV.

Fig. 4.2.10 shows the spatial distributions of the potential φ and of the potassium concentrations for two different distances W between the two cells. The channels of

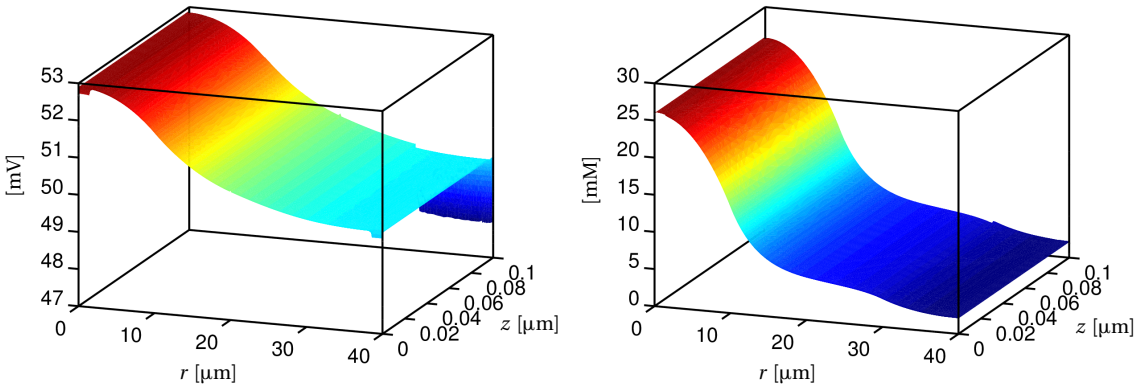

(a) φ with $W = 20\,\mu$m

(b) c_K with $W = 20\,\mu$m

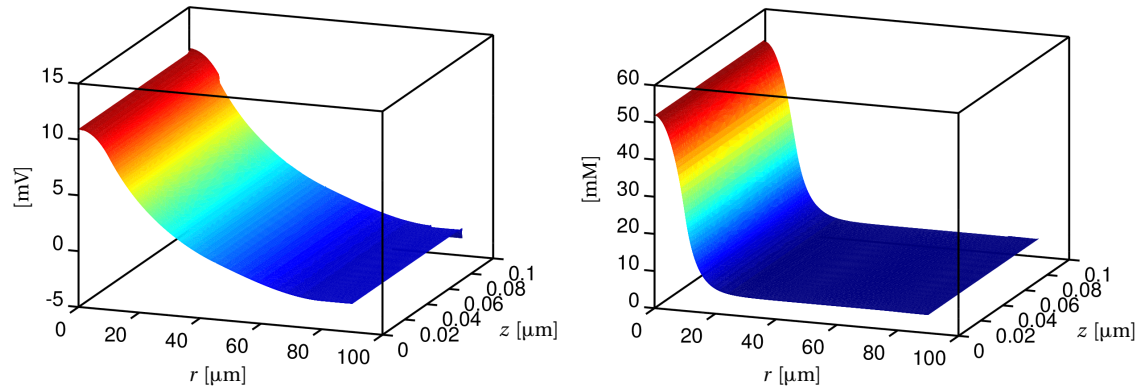

(c) φ with $W = 70\,\mu$m

(d) c_K with $W = 70\,\mu$m

Figure 4.2.10 – Spatial distributions of φ and of c_K after a stimulation of the first cell with a pulse of $V_{cell} = 50$ mV, keeping the second cell at V_{ceq} with a voltage clamp tecnique. Results for two different distances between the cells: $W = 20\,\mu$m and $W = 70\,\mu$m.

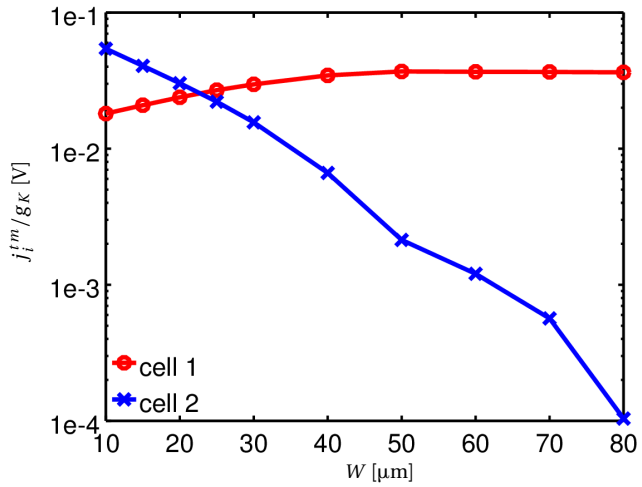

Figure 4.2.11 – Parametric semilogarithmic analysis for the transmembrane currents j_i^{tm}, $i = 1,2$ of the two cells as functions of W. j_1^{tm} is entering into the electrolyte, j_2^{tm} is entering into the second cell. Results obtained with a depolarizing pulse $V_{c1} = 50\,\text{mV}$ and with $V_{c2} = V_{ceq}$. The values reported are in V because we are considering j_i^{tm}/g_K, where g_K is the specific membrane conductance.

the first cell are always open and are injecting a K^+ current in the electrolyte, because of the depolarization. This causes an increase of the potassium concentration and of φ in the considered domain, which may lead, in turn, to the opening of the channels of the second cell. In Fig. 4.2.10-(b), where the cells are at a distance $W = 20\,\mu\text{m}$, we observe that there is an evident depletion in the spatial distribution c_K under Γ_{c2}. This is due to the fact that the potassium current here is entering into the second cell: as physically expected the potassium is injected by one cell and collected from the other one. In the case of a larger W (Fig. 4.2.10-(c)-(d)), the value of the potential in the electrolyte is lower and there is practically no current entering into the second cell, because here the ions are free to flow in a larger portion of electrolyte.

A parametric analysis is carried out in Fig. 4.2.11, where we study the decreasing of the integral mean of the transmembrane current entering into the second cell as a function of the distance W. The decay is very fast and exponential, while the integral mean of the transmembrane current injected by the stimulated cell stabilizes itself around $9\,\text{A}\,\text{m}^{-2}$ (which is computed multiplying the value reported in Fig. 4.2.11 by the potassium membrane specific conductance $g_K = 250\,\text{S}\,\text{m}^{-2}$). The two lines intersect at a distance $W \simeq 25\,\mu\text{m}$. This is of course unphysical, because it means that in the second cell is entering more potassium than the quantity coming out from the first one.

We can give an interpretation of this behavior by some considerations on the

modeling hypotheses. Firstly, the axial symmetry is an approximation and is definitely not valid when we consider a geometry with a small distance W between the two cells. Secondly, when we study two cells, we need to remember that the transmembrane channels are located all over the membrane (not only in the attached part) and the ions can be injected and collected not only in the cleft area. Therefore, in a configuration where the two cells are very close to each other, the considered domain does not properly account for the entire phenomena and the modeling of Γ_{ef} introduced in Section 2.2.4 is no longer a good approximation. In this specific case, one should solve the model in the whole surrounding electrolyte and, particularly, describe the ion flow in the portion of electrolyte placed between the two cells, because it is expected that almost the same amount of potassium injected by the first membrane sould be collected from the second one.

4.3 Reduced order models

In this section we illustrate the results obtained solving the reduced models introduced in Section 2.3 in order to decrease the computational effort of a three dimensional discretization. We have derived two dimensional equations in the middle plane of the electrolyte cleft and now we validate this averaging procedure.

4.3.1 Reduced model with approximation of the boundary layers

The reduced models of Section 2.3.1 are derived in the x-y middle plane of the electrolyte cleft. As in most of our simulations, the configuration we want to study is axisymmetric. Therefore, as schematically depicted in Fig. 4.3.1, we can reduce the computational domain Ω_{2D} to a one dimensional manifold Ω_{rad}, describing the variation along the radial direction of the quantities of interest. The two dimensional spatial distributions of these latter can be obtained with a rotation of Ω_{rad} around the centre of the cell.

The considered domain Ω_{rad} is the union of two different parts $\Omega_r^{cell} \cup \Omega_r^{ef}$: the first portion Ω_r^{cell} represents the area where the cell is attached, the second one Ω_r^{ef} is instead the free part of extracellular fluid. This latter division is essential, because the coupling with the cell results in a distribution along the z-direction that is different from the one in the free part, as explained in Section 2.3.1. In the description of the

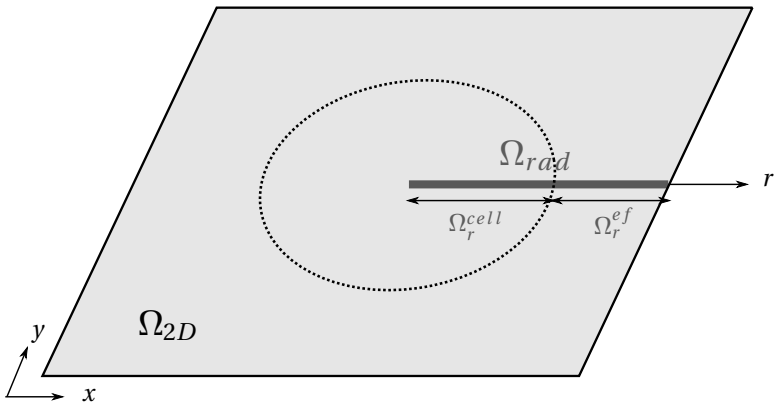

Figure 4.3.1 – The one dimensional radial domain is $\Omega_{rad} = \Omega_r^{cell} \cup \Omega_r^{ef}$, introduced for the intrinsic axial symmetry of the two dimensional domain Ω_{2D}. With a rotation of Ω_{rad} around the centre, the entire Ω_{2D} is obtained.

results of Section 4.2, we have pointed out how the strong coupling with the cell and the electronic substrate gives rise to steep boundary layers in the spatial distribution of the potential φ and of the concentrations c_i near the membrane and the oxide (see, for example, Fig. 4.2.1). When solving model (2.36) in Ω_{rad}, although the description is in the middle plane of the cleft with averaged variables, we are able to account for this behavior computing the top and the bottom values of the quantites of interest.

We start focusing our attention only on the attached part Ω_r^{cell}, in order to reproduce the two dimensional results of Fig 4.2.1 with this reduced model. In our numerical computations, we choose a boundary layer thickness $H \simeq 2\lambda_{Debye} \simeq 1.6\,\text{nm}$, which is physically correct and is also in good agreement with the results obtained in the simulations of the previous sections. Fig. 4.3.2 shows the radial distributions of the averaged values $\overline{\varphi}$ and $\overline{c}_i$, but also the radial distributions of φ_{top}, c_i^{top} and φ_{bot}, c_i^{bot}, which are the values respectively at the boundaries Γ_{cell} and Γ_{sub} at $z = \pm\delta_j/2$ of the three dimensional domain. We can also reconstruct the z-dependence of the potential and of the concentrations for a fixed point $\bar{r}$, only having the averaged and the top and bottom values, with the following post-processing formulas:

$$\varphi(\bar{r},z) = \overline{\varphi}(z,\bar{r}) + \left(\frac{\varphi_{top}(\bar{r},z)-\overline{\varphi}(\bar{r},z)}{H}\right)\Bigg|_{z\in\Omega_1} + \left(\frac{\overline{\varphi}(\bar{r},z)-\varphi_{bot}(\bar{r},z)}{H}\right)\Bigg|_{z\in\Omega_3} \quad (4.4a)$$

$$c_i(\bar{r},z) = \overline{c}_i \exp\left(-z_i \frac{\varphi(\bar{r},z)-\overline{\varphi}(\bar{r},z)}{V_{th}}\right), \quad (4.4b)$$

where $\Omega_1$and Ω_3 are the boundary layers subdomains (see Fig. 2.3.2). The reconstruction of $\varphi(r=0,z)$ and of $c_K(r=0,z)$ is illustrated in Fig. 4.3.3 and we see that the major term in the electrolyte system behavior is the capacitive coupling with the

cell membrane.

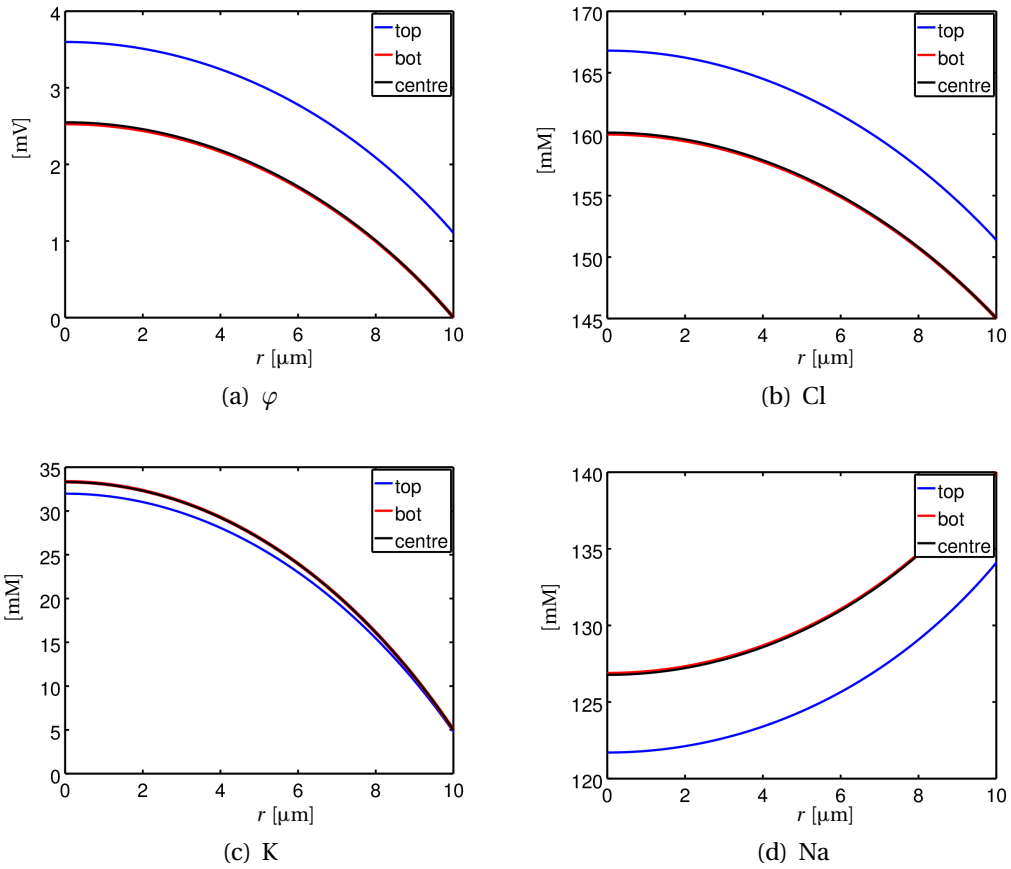

(a) φ (b) Cl

(c) K (d) Na

Figure 4.3.2 – Radial distribution of $\overline{\varphi}$ and of $\overline{c}_i$ in Ω_r^{cell} (here $\left|\Omega_r^{cell}\right| = R_{cell} = 10\,\mu\text{m}$). To account for the boundary layers: distributions of the top and the bottom values φ_{top}, φ_{bot}, c_i^{top} and c_i^{bot}.

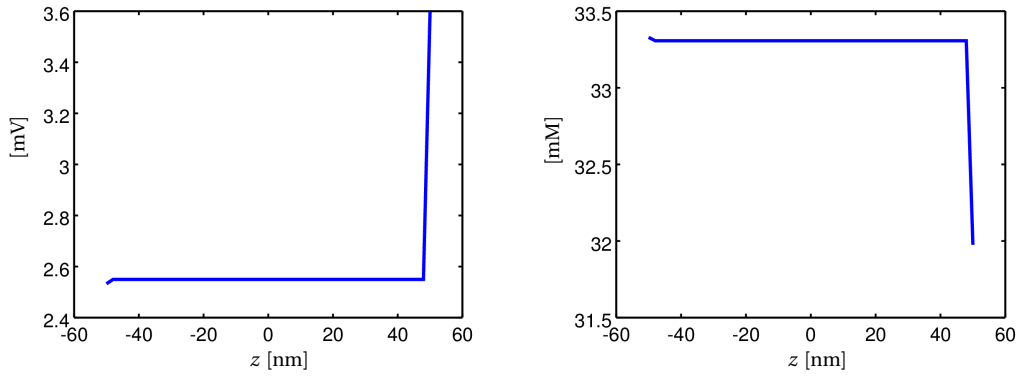

(a) $\varphi(r=0,z)$ (b) $c_K(r=0,z)$

Figure 4.3.3 – Distributions along the z-direction for the potential and the potassium concentration at $r=0$ using (4.4).

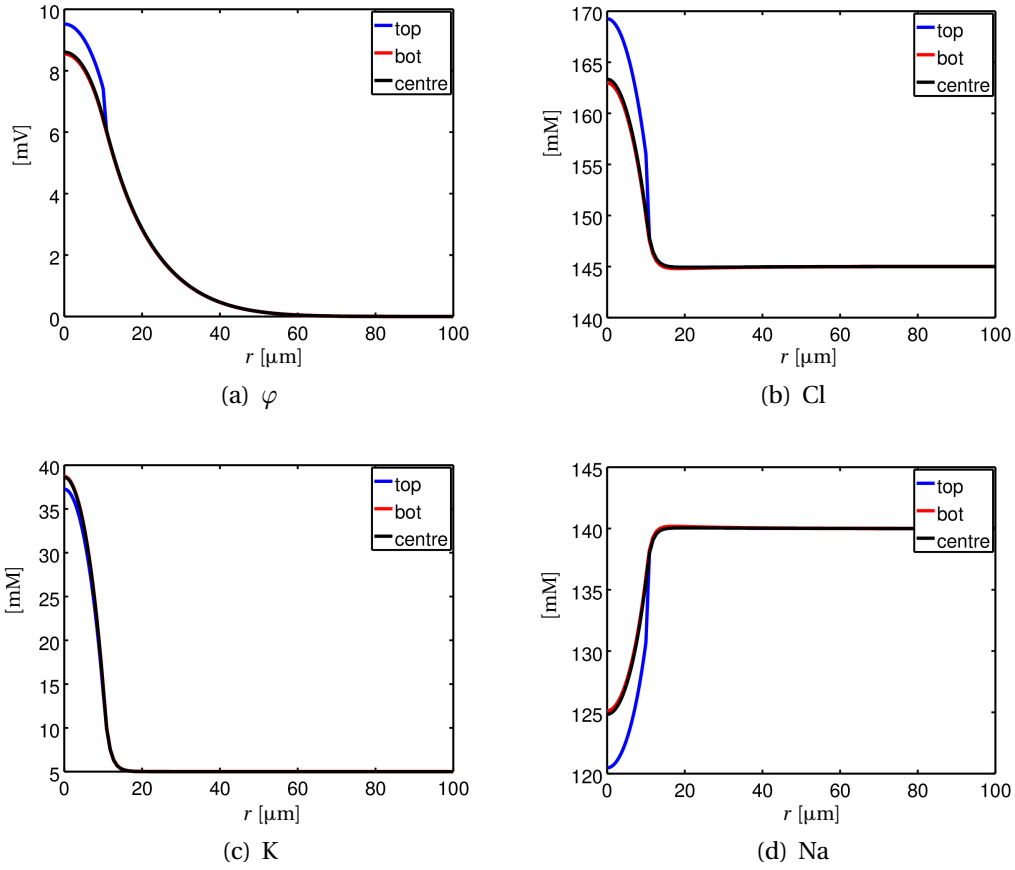

(a) φ (b) Cl

(c) K (d) Na

Figure 4.3.4 – Spatial distribution of $\overline{\varphi}$ and of $\overline{c}_i$ in the domain $\Omega_{rad} = \Omega_r^{cell} \cup \Omega_r^{ef}$ (results obtained with $\left|\Omega_r^{ef}\right| = 10 \cdot \left|\Omega_r^{cell}\right| = 10 \cdot R_{cell} = 50\,\mu\text{m}$). To account for the boundary layers: distributions of the top and the bottom values φ_{top}, φ_{bot}, c_i^{top} and c_i^{bot}.

These results are in good agreement with those obtained in the axisymmetric two dimensional computations of the previous sections, telling us that the proposed model reduction produces sensible results in the attached area.

Then, we solve the reduced model accounting also for the free part of electrolyte in the neighborhood of the cell, in such a way that the computational domain is the entire $\Omega_{rad} = \Omega_r^{cell} \cup \Omega_r^{ef}$. As explained in Section 2.3.1, in Ω_r^{ef} we assume that the quantities of interest do not vary along z, as shown for example by the spatial distributions of Section 4.2.1. This modeling assumption evidently results in the radial distributions of Fig. 4.3.4: the potential $\overline{\varphi}$ and the concentrations $\overline{c}_i$ are perfectly superimposed on the distributions of the top quantities in the free part. We observe a $1/r$ decay in Ω_r^{ef}, as expected, thanks to the introduction of the parameters C^* and ν^* describing the artificial electrolyte-electrolyte coupling, whose values are taken as in Section 4.2.1.

Therefore, we can say that the model mathematically derived in Section 2.3.1 is valid, because it gives results comparable with the ones obtained when solving a three dimensional model, but with a much smaller amount of degrees of freedom. One could then use this model to reproduce also the interactions between multiple cells and multiple electrodes, gaining a lot of computational time.

4.3.2 Area-contact lumped models

We discuss now the results of the solution of the model described in Section 2.3.2: we are able to successfully reproduce the results obtained by Brittinger and Frohmerz in [5], computing the spatial distribution of the potential $\varphi(x,y)$ and the time variation of the concentrations c_i.

The physical region chosen for the numerical simulations is a two dimensional domain, but, accordingly with [5] and with the model reduction operated in Section 2.3.2, we study only the part of the electrolyte covered by the cell. This is due to the fact that here the concentrations are not space dependent, but only evolve in time in the electrodiffusion model: therefore the ion flow in the surrounding electrolyte bath cannot be described at this point.

The model depends on several different physical parameters (reported in Table 4.1) which are the same used in [5]: we are considering a cleft with a thickness δ_j of 70 nm. The radius of the cell-chip adhesion area is around 15 µm, therefore the junction forms an extended planar electrical core-coat conductor. The cell we are studying is a HEK293 (Human Embryonic Kidney) with only K^+ channels and the simulated experiment is a depolarization with a patch pipette of the intracellular potential (a 50 ms pulse from $V_{cell} = -84$ mV to $V_{cell} = 50$ mV, shown in Figure 4.3.6-(a)). Besides K^+, the other ion species considered in these simulations are Cl^-, Na^+, Ca^{2+}, Mg^{2+} and $HEPES^-$.

Parameter	Value	Parameter	Value	Parameter	Value	Parameter	Value
δ_J	70 nm	c_K^{bath}	5 mM	c_K^{cell}	140 mM	g_M^K	250 S m^{-2}
A_J	200 µm	c_{Cl}^{bath}	145.6 mM	c_{Cl}^{cell}	144 mM	$g_M^i \; \forall i \neq K^+$	0 S m^{-2}
C_M	1 µF cm^{-2}	c_{Na}^{bath}	135 mM	c_{Na}^{cell}	5 mM	T	298.16 K
C_S	0.3 µF cm^{-2}	c_{Ca}^{bath}	1.8 mM	c_{Ca}^{cell}	5 mM	ϵ_r	80
V_{bath}	0 V	c_{Mg}^{bath}	1 mM	c_{Mg}^{cell}	2 mM		
V_G	0 V	c_{HEPES}^{bath}	5 mM	c_{HEPES}^{cell}	5 mM		

Table 4.1 – Physical parameters used in the electrical and in the electrodiffusion models.

Electrical model

The electrical model is the simplest one can think of. It reproduces the extracellular voltage caused by the electrical current charging the cell-chip capacitance at constant ion concentrations. In [5] the authors compute V_J as shown in (2.43); in the present work, we are solving equation (2.39) keeping the concentrations constant at their bulk values to find at each time step the spatial distribution of the cleft potential $\varphi(x,y)$ (represented in Figure 4.3.5 at two different time levels) and then computing its integral mean to compare the results with those of [5].

The cell-chip contact is described by the capacitances C_M and C_S of membrane and substrate, respectively. The global conductance in (2.40) is not varying in time and is computed in the following way

$$\sigma_{el} = \sum_{i=1}^{M} \sigma_i = q \sum_{i=1}^{M} |z_i| \mu_i c_i^{bath} \delta_J$$

using the constant concentration values of the considered ion species. We obtain a value around 2.38 µS, which is close the value used by Brittinger and Fromherz of $g_J = 2.1$ µS. The dynamics is then determined by an electrical time constant, which is for us $\tau = (C_M + C_S)/\sigma \simeq 1.0944$ µS: therefore the transient is really fast, as one can observe in Figure 4.3.6. When the cell is depolarized, almost instantaneously the potential goes to a value around 2 mV, which is a little less than the result $V_J \simeq 3$ mV obtained in [5]. The reason of this difference is due to the fact that we are comparing an integral mean of a spatial distribution over all the domain and a quantity V_J which

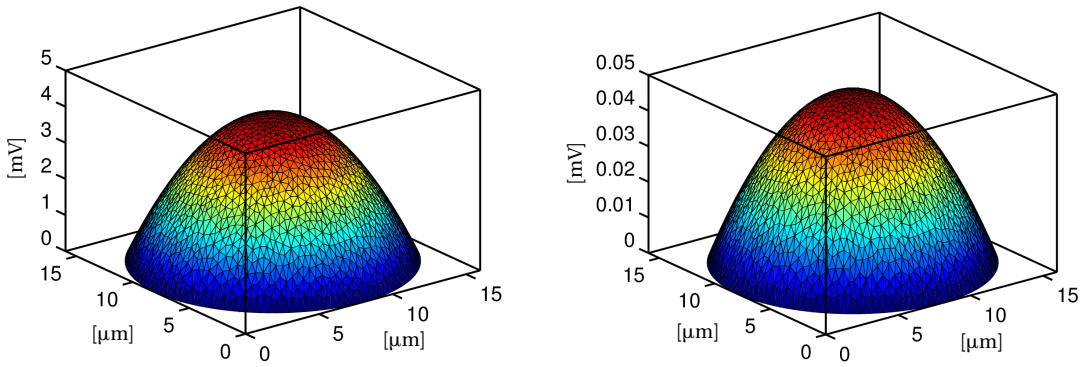

(a) φ at t=10 ms

(b) φ at t=100 ms

Figure 4.3.5 – Spatial distribution of the cleft potential φ in the circular domain: on the left after 10 ms (cell just depolarized: $V_{cell} = 50$ mV); on the right after 50 ms ($V_{cell} = -84$ mV).

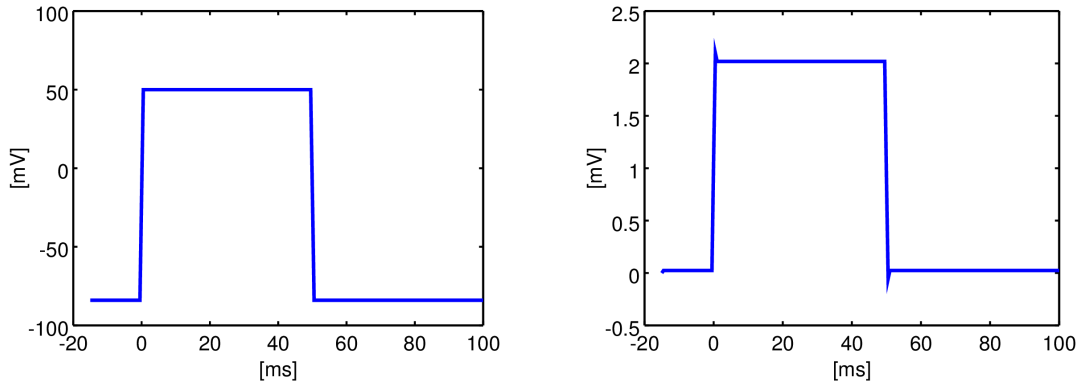

(a) Intracellular potential V_{cell}

(b) Cleft potential φ

Figure 4.3.6 – Left: depolarizing pulse of intracellular potential V_{cell}. Right: integral mean of φ obtained with the electrical model.

is not space dependent.

Electrodiffusion model

When the K^+ channels open, the ion concentrations in the junction change: the electrodiffusion model is a simplified description of the time variation of c_i, cosidering them as constant in space. The results of Brittinger and Fromherz are obtained solving (2.44a)-(2.44b), while we use the model presented in (2.46a)-(2.46d) to compute the spatial distribution of the potential φ but also the variation of the lumped concentrations c_i.

We solve this nonlinear model using the staggered algorithm introduced in Section 3.2.1. The algorithm converges in a reasonable number of iterations (less than 20 during the transients) when we use a fully nonlinear system for the concentrations equations, choosing a Newton method to solve them, as explained in Section 3.2.1. The other two linearization methods for the ODE system reported in Section 3.2.1 are able to reach the same result, but the time for a simulation tremendously increases, because at each time level the map needs many more iterations than before. Moreover, in order to have a correct solution, we have to use a relaxation parameter γ for both the potential and the concentrations according to the following strategy:

$$\begin{aligned} \varphi^{(k+1)} &= \gamma\varphi^{(k+1)} + (1-\gamma)\,\varphi^{(k)} \\ c_i^{(k+1)} &= \gamma c_i^{(k+1)} + (1-\gamma)\,c_i^{(k)}. \end{aligned}$$

γ must be set equal to a value around 0.01 to obtain the correct solution. The a-

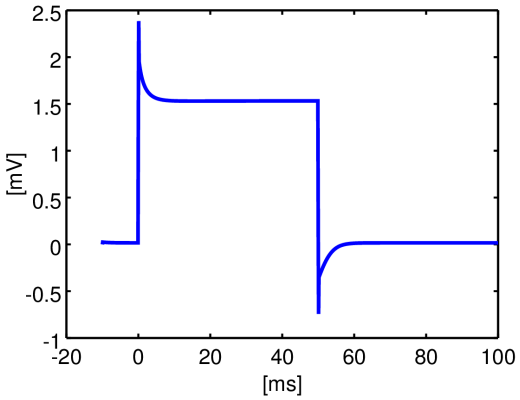

Figure 4.3.7 – Integral mean of φ obtained with the electrodiffusion model. The depolarization impulse V_{cell} applied is the same as the one shown in Figure 4.3.6.

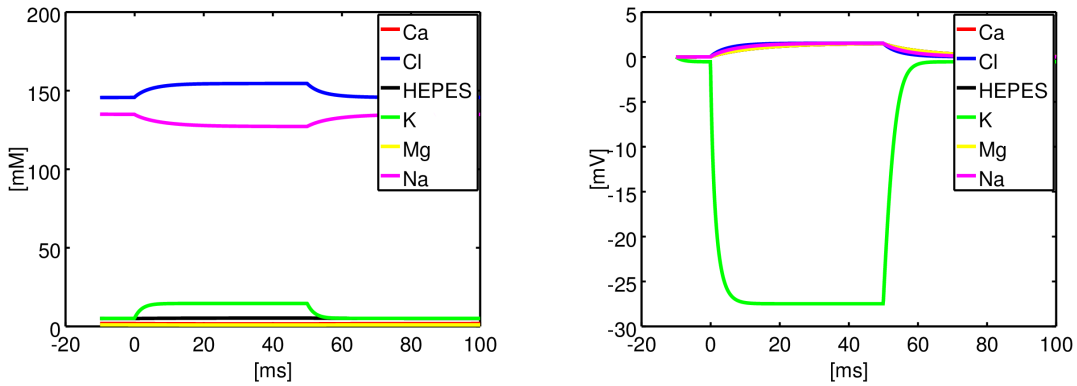

(a) Concentrations c_i

(b) Nernst potentials V_{J0}^i

Figure 4.3.8 – Changes of extracellular ion concentrations in the cell-chip junction and of the Nerst potentials V_{J0} between junction and bath.

priori refined temporal discretization described in Section 3.1 is mandatory for the convergence of the map and for an accurate tracking of the temporal evolution of the variables. For this particular problem we have also used a monolithic algorithm applied to the whole system (2.46a)-(2.46d): this works efficiently for this specific case and produces results in agreement with the ones obtained with the staggered map using the relaxation described above.

As one can observe in Figures 4.3.7 and 4.3.8, the slower dynamics is now taken into account and both the potential and the concentrations have transients with a time constant in the order of milliseconds, as expected (we have expressed the changes of extracellular ion concentrations in the junction also as Nernst potentials between junction and bath). The integral mean of the electrical potential φ increases

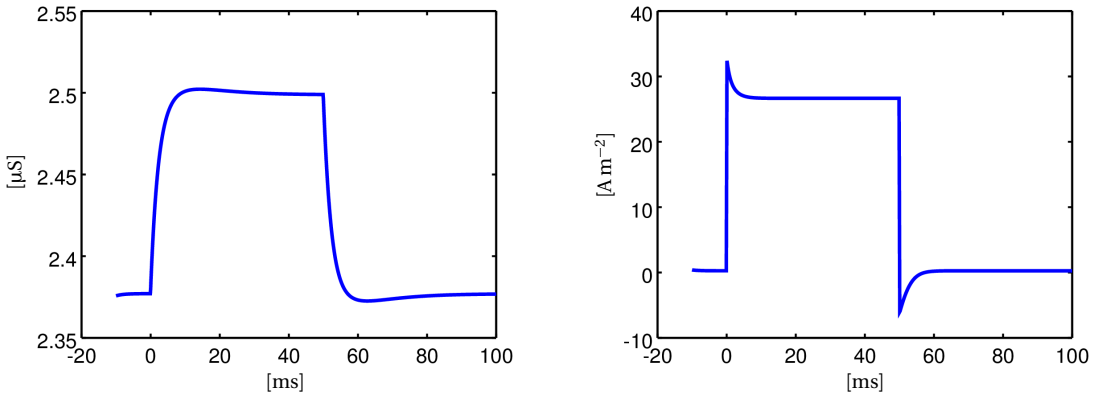

(a) Electrical conductance σ (b) K transmembrane current

Figure 4.3.9 – Left: electrical conductance σ of the junction, depending on ion concentrations. Right: lumped potassium transmembrane injected current $j_K^{tm} = g_{JM}^K \left(V_{cell} - V_J + V_{th}/z_K \ln(c_K^{cell}/c_K)\right)$ computed using as V_J the integral mean of φ.

fast to a value around 2.5 mV and subsequently decays to a stationary level around 1.5 mV. The same arguments valid for the electrical model should be applied here to the comparison of the value computed here with an integral mean over all the domain and of the lumped V_J in [5].

The potassium concentration increases from 5 mM to 17 mM, giving a Nernst potential $V_J^K \simeq -27$ mV in the junction. The redistribution of all other ions is smaller, with Nernst potentials determined by electrochemical equilibrium in the stationary state as $V_{J0}^i = V_J - V_{bath} \simeq 1$ mV. The decay of the electrical potential φ after the initial increase is due to the enhanced potassium concentration in the junction that lowers the driving force given by the difference $V_J - V_{bath} - V_{J0}^i$, the current across the membrane (depending on the logarithm of the reciprocal of c_K) and also the electrical resistance of the junction, which is the reciprocal of $\sigma(t) = q\sum_{i=1}^M |z_i|\mu_i c_i(t)\delta_J$. The time variation of these last two quantities is shown in Figure 4.3.9. The dynamics of relaxation is then determined by the ion diffusion coefficients D_i with a time constant which is $\tau_{diff}^i = A_J/5.78\pi D_i$ in the order of milliseconds: thus the electrodiffusion gives rise to a dynamics that is far slower than electrical charging, having $\tau_{diff} \gg \tau$ as one can see comparing Figure 4.3.6 with 4.3.7.

The spatial distribution of the potential φ is again parabolic, as for the electrical model. In Fig. 4.3.10 one can observe that when the cell has just been depolarized the maximum value is around 3.8 mV; after 35 ms, when the transient is already exhausted, the maximum value is around 3.15 mV.

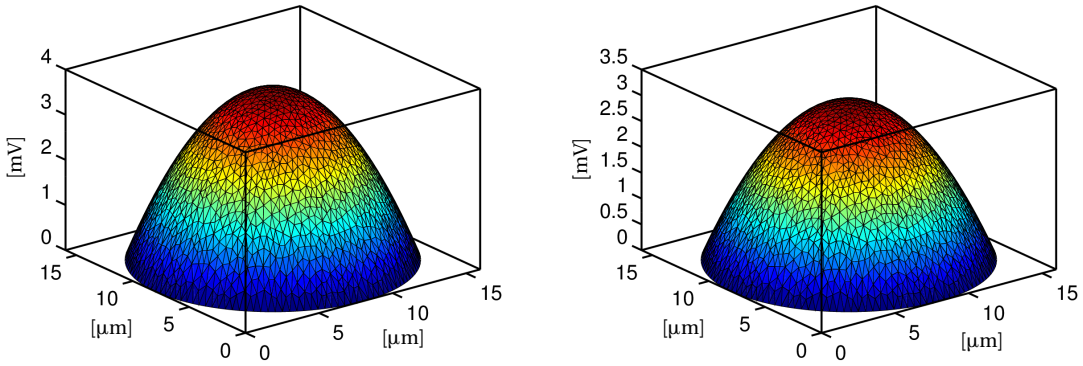

(a) φ at t=0.5 ms

(b) φ at t=35 ms

Figure 4.3.10 – Spatial distribution of the cleft potential φ in the circular domain: on the left after 0.5 ms (cell just depolarized: $V_{cell} = 50$ mV) when the transient is just started; on the right after 35 ms when the cell is still depolarized but the transient is exhausted.

Chapter 5

Conclusions and Future Work

In the present Master Thesis we have addressed the mathematical modeling and numerical approximation of bio-hybrid devices. This subject is of paramount importance in the wider scientific context of neuroelectronics, where the main aim is to actually realize devices consisting of the integration of biological tissues with solid-state integrated electronic circuits.

In this treatise we have illustrated a suitable mathematical characterization of bio-electronic interfaces, investigating different possible modeling hypotheses on the coupling between the two different enviroments (cell and electronic device) and on the derivation of model dimensional reductions, perfomed to decrease the computational simulation effort. A hierarchy of multiscale models has been therefore presented and extensively validated with a broad range of numerical computations, obtaining sensible results and comparing them with literature and experiments. This mathematical description has also been applied to complex configurations and has proved to be able to simulate the interactions between multiple cells and multiple devices. Even if the present work is far from a real world description, it can be considered a first step for the construction of mathematical models to be used in the design of actual devices.

Clearly, future research is needed to provide a better description of this very complex multiscale/multiphysics problem. Among possible developments, we mention a more accurate modeling of the electronic substrate, which can be useful in studying different types of stimulation, for example a different polarization of the chip influencing the cell. A model for the chemical binding mechanism of the ions to the electronic substrate is also required, in order to fully describe the EOSFET device. Another important improvement in the mathematical characterization can be a coup-

ling between electro-chemical and fluid-mechanical systems, in order to account for the forces due to pressure differences and flow in the aqueous medium.

Lastly, a more realistic description of the problem geometry, with full three dimensional computations including the intracellular fluid is mandatory to faithfully reproduce the entire phenomena. The above mentioned improvements should give the realistic chance to go further in the study of the interactions between multiple cells, maybe introducing a neural network and simulating a whole brain slice, as in the experimental results of [23, 57].

Appendix A

Scaling of the PNP system

In this appendix, we describe the scaling procedure applied to the PNP system and we provide a complete list of the values of the scaling parameters used in the procedure. The procedure can be applied on the several other models discussed in the thesis in a way similar to that illustrated here.

In general, a closed form solution for system (2.4a)-(2.4e) is impossible to determine and an approximate solution is therefore required. The first step towards a numerically stable approximation consists in a reformulation of the system to obtain a scaled set of equations, where variables are adimensional and normalized. This operation is useful in numerical computations, since each problem variable has a different unit and cannot be compared to the others (electric potential vs. ion concentrations) and may also have a range of variation of several orders of magnitudes, as in the case of ion concentrations. The scaling procedure leads to a set of PDEs where variables are dimensionless and have comparable orders of magnitude.

For each generic variable w of the system is rewritten as

$$w = \widehat{w} \cdot \overline{w}, \tag{A.1}$$

where $\bar{w}$ is the scaling constant and $\widehat{w}$ is the new scaled and adimensional variable (for a general treatise of this procedure see [45], appendix A).

We introduce the scaling factors $\overline{x}$, $\overline{c}$, $\overline{\varphi}$ and $\overline{D}$ for the main quantities in the PNP system. Then, using (A.1) in the continuity equations (2.4a) we get

$$\frac{\partial(\overline{c}\,\widehat{c}_i)}{\partial(\widehat{t}\,\overline{t})} + \frac{1}{\overline{x}}\,\widehat{\mathrm{div}}\,\widehat{\mathbf{f}}_i\,\bar{\mathrm{f}} = 0 \qquad i = 1,\ldots M$$

from which we are able to obtain a scaled continuity equation by defining $\overline{t}$ and $\bar{\mathrm{f}}$ in

such a way that

$$\frac{\overline{c}}{\overline{t}} = \frac{\bar{\mathrm{f}}}{\overline{x}}.$$

In order to compute $\bar{\mathrm{f}}$, we need to adimensinalize the Nernst-Planck expression for the fluxes (2.4b), getting

$$\mathbf{f}_i = -\overline{c}\,\frac{\overline{D}}{\overline{x}}\left[\widehat{\nabla}\,\widehat{c}_i + z_i\,\widehat{\nabla}\,\widehat{\varphi}\,\widehat{c}_i\right] = \widehat{\mathbf{f}}_i\,\bar{\mathrm{f}} \qquad i = 1,...M.$$

Here we set

$$\bar{\mathrm{f}} = \frac{\overline{x}\,\overline{c}\,\overline{D}}{\overline{x}},$$

and then we obtain the time scaling factor as follows

$$\overline{t} = \frac{\overline{x}^2}{\overline{D}}.$$

The scaling procedure applied on the Poisson equation (2.4c) gives

$$-\frac{\epsilon}{\overline{x}^2}\,\widehat{\mathrm{div}}\left(\widehat{\nabla}\left(\widehat{\varphi}\,\overline{\varphi}\right)\right) = q\sum_i z_i\,\widehat{c}_i\,\overline{c},$$

from which we obtain a scaled Poisson equation, upon introducing the singular perturbation parameter

$$\lambda^2 = \frac{\epsilon_0\epsilon_r\,\overline{\varphi}}{q\overline{c}\,\overline{x}^2}.$$

Therefore, denoting the new scaled variables with the same symbols as in the dimensional case, the scaled PNP system reads as follows

$$\begin{aligned}
\frac{\partial c_i}{\partial t} + \mathrm{div}\mathbf{f}_i\left(c_i,\varphi\right) &= 0 && i = 1,...,M\\
\mathbf{f}_i\left(c_i,\varphi\right) &= D_i\left(z_i c_i \mathbf{E} - \nabla c_i\right) && i = 1,...,M\\
\lambda^2 \mathrm{div}\mathbf{E} &= \sum_i z_i c_i &&\\
\mathbf{E} &= -\nabla\varphi. &&
\end{aligned}$$

The parameter λ is the scaled Debye length and can be rewritten as

$$\lambda = \left(\frac{\epsilon_0\epsilon_r\overline{\varphi}}{q\overline{c}}\right)^{1/2}\frac{1}{\overline{x}}.$$

It is relevant to observe that if $\lambda^2 \ll 1$ the PNP system exhibits a singularly perturbed

character (for a details see [43]), and the corresponding solutions may exhibit internal and/or boundary layers. The PNP system applied to our problems is singularly perturbed, because a typical value is $\lambda^2 \simeq 10^{-8}$, therefore stable discretization schemes must be used in the numerical approximation

We conclude the description of the scaling procedure with the following list of the values of all the scale factors and parameters.

Scaling factor	Value
$\overline{x} = R_{cell}$	10 nm
$\overline{c} = N_A$	6.023×10^{23} m^{-3}
$\overline{D}$	2×10^{-9} m^2 s^{-1}
$\overline{\varphi} = V_{th}$	25.7 mV
$\bar{\mathrm{f}}$	1.7726×10^{22} m^{-2} s^{-1}
$\overline{t}$	4.9261×10^{-2} s
$\lambda^2 := \dfrac{\epsilon \overline{\varphi}}{q \overline{x}^2 \overline{c}}$	1.3×10^{-8}
$\bar{\mathrm{j}} = q\bar{\mathbf{f}}$	2.84×10^3 A m^{-2}
$\overline{\mathrm{E}} = \overline{\varphi} / \overline{x}$	2.5693×10^3 V m^{-1}

Table A.1 – Scaling factors and relevant parameters.

Bibliography

[1] BANK, R. E., COUGHRAN JR, W., AND COWSAR, L. C. The finite volume scharfetter-gummel method for steady convection diffusion equations. *Computing and Visualization in Science 1*, 3 (1998), 123–136.

[2] BOSISIO, F., MICHELETTI, S., AND SACCO, R. A discretization scheme for an extended drift-diffusion model including trap-assisted phenomena. *Journal of Computational Physics 159*, 2 (2000), 197–212.

[3] BRERA, M. Multiphysics/multiscale computational modeling in neuroelectronics. Master's thesis, Politecnico di Milano, 2009.

[4] BRERA, M., JEROME, J. W., MORI, Y., AND SACCO, R. A conservative and monotone mixed-hybridized finite element approximation of transport problems in heterogeneous domains. *Computer Methods in Applied Mechanics and Engineering 199*, 41 (2010), 2709–2720.

[5] BRITTINGER, M., AND FROMHERZ, P. Field-effect transistor with recombinant potassium channels: fast and slow response by electrical and chemical interactions. *Applied Physics A 81*, 3 (2005), 439–447.

[6] COGLIATI, M., AND PORRO, M. Third generation solar cells: modeling and simulations. Master's thesis, Politecnico di Milano, 2009.

[7] CULPO, M., AND DE FALCO, C. Substructuring Methods for Coupled PDE/DAE Systems. CoMSON EU-FP6 Documentation, 2008.

[8] DE FALCO, C. *Quantum–corrected drift–diffusion models and numerical simulation of nanoscale semiconductor devices*. PhD thesis, Ph. D. thesis, Universita degli Studi di Milano, 2006.

[9] DE FALCO, C., AND CULPO, M. bim octave-forge package. `http://octave.sourceforge.net/bim/index.html`. [Last retreived 10/12/2010, version 1.0.0].

[10] DE FALCO, C., AND CULPO, M. msh octave-forge package. `http://octave.sourceforge.net/msh/index.html`. [Last retreived 10/12/2010, version 1.0.1].

[11] DE FALCO, C., PORRO, M., SACCO, R., AND VERRI, M. Multiscale modeling and simulation of organic solar cells. *Computer Methods in Applied Mechanics and Engineering 245* (2012), 102–116.

[12] FARREL, P., AND GARTLAND, E. On the scharfetter-gummel discretization for drift-diffusion continuity equations. *Computational Methods for Boundary and Interior Layers in Several Dimensions* (1991), 51–79.

[13] FROMHERZ, P. Joining microelectronics and microionics: Nerve cells and brain tissue on semiconductor chips. *Solid-State Electronics 52*, 9 (2008), 1364–1373.

[14] GARDNER, C. L., JONES, J. R., BAER, S. M., AND CHANG, S. Simulation of the ephaptic effect in the cone–horizontal cell synapse of the retina. *SIAM Journal on Applied Mathematics 73*, 2 (2013), 636–648.

[15] GATTI, E., MICHELETTI, S., AND SACCO, R. A new galerkin framework for the drift-diffusion equation in semiconductors. *East West Journal of Numerical Mathematics 6* (1998), 101–136.

[16] GRAHAME, D. C. The electrical double layer and the theory of electrocapillarity. *Chemical Reviews 41*, 3 (1947), 441–501.

[17] GUMMEL, H. A self-consistent iterative scheme for one-dimensional steady state transistor calculations. *Electron Devices, IEEE Transactions on 11*, 10 (1964), 455–465.

[18] HALL, J. E., AND GUYTON, A. C. *Textbook of medical physiology*. Saunders, 2011.

[19] HILLE, B. *Ion channels of excitable membranes*, vol. 507. Sinauer Sunderland, MA, 2001.

[20] HODGKIN, A. L., AND HUXLEY, A. F. Currents carried by sodium and potassium ions through the membrane of the giant axon of loligo. *The Journal of physiology 116*, 4 (1952), 449.

[21] HODGKIN, A. L., AND HUXLEY, A. F. A quantitative description of membrane current and its application to conduction and excitation in nerve. *The Journal of physiology 117*, 4 (1952), 500.

[22] HOPF, E. The partial differential equation ut+ uux= μxx. *Communications on Pure and Applied mathematics 3*, 3 (1950), 201–230.

[23] HUTZLER, M., LAMBACHER, A., EVERSMANN, B., JENKNER, M., THEWES, R., AND FROMHERZ, P. High-resolution multitransistor array recording of electrical field potentials in cultured brain slices. *Journal of neurophysiology 96*, 3 (2006), 1638–1645.

[24] HUXLEY, A. From overshoot to voltage clamp. *Trends in neurosciences 25*, 11 (2002), 553–558.

[25] JEROME, J. W. *Analysis of charge transport*. Springer Berlin, 1996.

[26] KEENER, J., AND SNEYD, J. *Mathematical Physiology*. Springer-Verlag, 2009.

[27] KERKHOVEN, T. A spectral analysis of the decoupling algorithm for semiconductor simulation. *SIAM Journal on Numerical Analysis 25*, 6 (1988), 1299–1312.

[28] LAZAROV, R. D., AND ZIKATANOV, L. T. An exponential fitting scheme for general convection-diffusion equations on tetrahedral meshes. *arXiv preprint arXiv:1211.0869* (2012).

[29] LONGARETTI, M., CHINI, B., JEROME, J. W., AND SACCO, R. Electrochemical modeling and characterization of voltage operated channels in nano-bio-electronics. *Sensor Letters 6*, 1 (2008), 49–56.

[30] MARKOWICH, P. A. *The stationary semiconductor device equations*, vol. 1. Springer, 1986.

[31] MARTINOIA, S., AND MASSOBRIO, P. Isfet–neuron junction: circuit models and extracellular signal simulations. *Biosensors and Bioelectronics 19*, 11 (2004), 1487–1496.

[32] MASSOBRIO, G., MASSOBRIO, P., AND MARTINOIA, S. Modeling and simulation of silicon neuron-to-isfet junction. *Journal of Computational Electronics 6*, 4 (2007), 431–437.

[33] MORI, Y. *A three-dimensional model of cellular electrical activity*. PhD thesis, New York University, 2006.

[34] MORI, Y., AND PESKIN, C. S. A numerical method for cellular electrophysiology based on the electrodiffusion equations with internal boundary conditions at the membrane. *Communications in Applied Mathematics and Computational Sciences 4* (2009), 85–134.

[35] NEHER, E. Molecular biology meets microelectronics. *Nature Biotechnology 19*, 2 (2001), 114–114.

[36] NEHER, E., AND SAKMANN, B. The patch clamp technique. *Scientific American 266*, 3 (1992), 44–51.

[37] NEUEN, C. *Ein Multiskalenansatz zur Poisson-Nernst-Planck Gleichung (A Multiscale Approach to the Poisson-Nernst-Planck Equation)*. PhD thesis, Diplomarbeit Universität Bonn, 2010.

[38] PABST, M., WROBEL, G., INGEBRANDT, S., SOMMERHAGE, F., AND OFFENHÄUSSER, A. Solution of the Poisson-Nernst-Planck equations in the cell-substrate interface. *The European Physical Journal E 24*, 1 (2007), 1–8.

[39] PARK, J., AND JEROME, J. Qualitative properties of steady-state poisson–nernst–planck systems: Mathematical study. *SIAM Journal on Applied Mathematics 57*, 3 (1997), 609–630.

[40] PATA, V. Appunti del corso di analisi reale e funzionale, 2010.

[41] PODS, J., SCHÖNKE, J., AND BASTIAN, P. Electrodiffusion models of neurons and extracellular space using the Poisson-Nernst-Planck equations. Numerical simulation of the intra-and extracellular potential for an axon model. *Biophysical journal 105*, 1 (2013), 242–254.

[42] QUARTERONI, A., AND VALLI, A. *Numerical approximation of partial differential equations*, vol. 23. Springer, 2008.

[43] ROOS, H.-G., STYNES, M., AND TOBISKA, L. Robust numerical methods for singularly perturbed differential equations. *Springer Ser. Comput. Math 24* (2008).

[44] RUBINSTEIN, I. *Electro-diffusion of ions*, vol. 11. SIAM, 1990.

[45] SALSA, S. *Equazioni a derivate parziali: Metodi, modelli e applicazioni*. Milano: Springer-Verlag Milan, 2010.

[46] SAMSON, E., AND MARCHAND, J. Numerical solution of the extended Nernst-Planck model. *Journal of colloid and interface science 215*, 1 (1999), 1–8.

[47] SCHARFETTER, D., AND GUMMEL, H. Large-signal analysis of a silicon read diode oscillator. *Electron Devices, IEEE Transactions on 16*, 1 (1969), 64–77.

[48] SCHOEN, I., AND FROMHERZ, P. The mechanism of extracellular stimulation of nerve cells on an electrolyte-oxide-semiconductor capacitor. *Biophysical Journal 92*, 3 (2007), 1096 – 1111.

[49] SCHOEN, I., AND FROMHERZ, P. Extracellular stimulation of mammalian neurons through repetitive activation of Na+ channels by weak capacitive currents on a silicon chip. *Journal of Neurophysiology 100*, 1 (2008), 346–357.

[50] SELBERHERR, S. *Analysis and simulation of semiconductor devices*. Springer Wien; New York, 1984.

[51] TAUR, Y., NING, T. H., ET AL. *Fundamentals of modern VLSI devices*, vol. 2. Cambridge University Press Cambridge, 1998.

[52] VAN DER SCHOOT, B. H., AND BERGVELD, P. Isfet based enzyme sensors. *Biosensors 3*, 3 (1988), 161–186.

[53] WASER, R. *Nanoelectronics and information technology*. John Wiley & Sons, 2012.

[54] WILLNER, I., AND KATZ, E. *Bioelectronics: from theory to applications*. John Wiley & Sons, 2006.

[55] WROBEL, G., SEIFERT, R., INGEBRANDT, S., ENDERLEIN, J., ECKEN, H., BAUMANN, A., KAUPP, U. B., AND OFFENHÄUSSER, A. Cell-transistor coupling: investigation of potassium currents recorded with p-and n-channel fets. *Biophysical journal 89*, 5 (2005), 3628–3638.

[56] XU, J., AND ZIKATANOV, L. A monotone finite element scheme for convection-diffusion equations. *Mathematics of Computation of the American Mathematical Society 68*, 228 (1999), 1429–1446.

[57] ZECK, G., AND FROMHERZ, P. Noninvasive neuroelectronic interfacing with synaptically connected snail neurons immobilized on a semiconductor chip. *Proceedings of the National Academy of Sciences 98*, 18 (2001), 10457–10462.

Ringraziamenti

Alla fine di questo lavoro, desidero innanzi tutto ringraziare il professor Riccardo Sacco, che mi ha dato la possibilità di lavorare su argomenti molto stimolanti. Lo ringrazio per avermi insegnato moltissimo, per la continua disponibilità nonostante i numerosi impegni e per la sua curiosità scientifica e voglia di trovare sempre nuovi spunti, coinvolgendo chi lavora con lui.

Un enorme ringraziamento va poi a Matteo Porro, per la sua presenza costante ad ogni mio problema e domanda, per il grande aiuto e supporto e per tutti i consigli che mi ha dato.

Il ringraziamento più grande è, ovviamente, per i miei genitori, per avermi cresciuta, educata e amata e perché so di poter contare su di loro sempre e comunque. Li ringrazio anche per avermi trasmesso con forza la loro passione per la scienza e la conoscenza. Grazie a loro ho cominciato questo percorso e sono riuscita a portarlo fino alla fine, perchè mi hanno sostenuta e incoraggiata in ogni momento e senza mai smettere di credere in me.

Un abbraccio fortissimo va poi a mio fratello Stefano, per tutte le risate e anche per le litigate, e perché per me resta sempre il bambino che prendevo per mano, anche se mi ha superata in altezza ormai da tempo.

Voglio poi ringraziare i miei compagni di avventura, per aver reso bellissimi questi anni così impegnativi, per le giornate di studio, le vacanze, le cene a casa mia e tutti i momenti passati insieme.

Il primo grazie è per Jacopo, per esserci sempre stato, per aver sopportato con pazienza le mie manie e il mio caratteraccio e per avermi consolata e spronata ogni volta che ne ho avuto bisogno. Ringrazio Francesco, per avermi fatto fare un sorriso o una risata ogni giorno, anche nei momenti peggiori, e ringrazio Giorgio, che anche se

è scappato quando era ancora in tempo, è presente col suo modo incostantemente costante. Grazie ad Andrea per averci resi tutti più nerd e per le nostre discussioni su chi ha più pasta nel piatto e a Nicolò per avermi fatto compagnia nelle mie ansie pre-esame.

Ringrazio Eleonora per le interminabili telefonate, il sostegno e la sua voglia di starmi e avermi vicina, Valeria (o meglio: Miranda) per i pettegolezzi, le chiacchierate e le sue domande sempre geniali, e Silvia, perchè nonostante l'incredibile metamorfosi, è sempre disponibile come quando l'ho conosciuta.